Radiometric calibration and validation of GOSAT/TANSO-FTS thermal infrared spectra

February 2020

Fumie Kataoka

Graduate School of

Science and Engineering

CHIBA UNIVERSITY

（千葉大学審査学位論文）

Radiometric calibration and validation of GOSAT/TANSO-FTS thermal infrared spectra

February 2020

Fumie Kataoka

Graduate School of

Science and Engineering

CHIBA UNIVERSITY

Contents

1. Introduction

1.1. Background

Atmospheric carbon dioxide (CO_2) and methane (CH_4) are important greenhouse gases (GHGs) that cause global warming. The global temperature of the land and ocean combined increased by 0.85°C between 1880 and 2012 (Pachauri et al., 2014). A total of 195 countries signed the 21st Conference of Parties (COP21, 2015) Agreement in Paris, setting out a global action plan to avoid rapid climate change by limiting global warming to less than 2°C and, ideally, to 1.5°C. From 2023, all parties will periodically participate in a "global stock take" as part of the Paris Agreement, imposing emissions reductions and adaptation in line with its long-term goals. The Guidelines for National Greenhouse Gas Inventories (IPCC, 2006) provide methodologies for estimating national inventories of anthropogenic emissions (by source) and removals (by sink) of GHGs. In 2019, the refined version Guidelines, titled "2019 Refinement to the 2006 IPCC Guidelines for National Greenhouse Gas Inventories (2019 Refinement)" (Calvo et al., 2019) was published. It provided an updated and sound scientific basis to support the preparation and continuous improvement of national GHG inventories. The guidelines and refinement are composed of five volumes, the first of which is summarized as follows:

"Volume 1: General Guidance and Reporting updates on: national greenhouse gas inventory arrangements and management tools, data collection strategy, use of facility-level data in inventories, uncertainty analysis, key category analysis, comparison of greenhouse gas emission estimates with atmospheric measurements, use and reporting of models and several other issues."

Satellite and in-situ atmospheric measurements are important for estimating inventory emissions as part of inventory quality assurance and quality control procedures. This initiative also contributes to the global Sustainable Development Goals (SDGs).

1.2. Satellite observation of greenhouse gases

The satellite mission of the GHGs observation from space has started since the late 1990s. Recently, private and non-governmental organizations have used satellites for this purpose, in addition to the national space agency. Most sensors that measure GHGs are passive, but active sensors have recently been developed. Figure 1.2-1 summarizes the past, current, and future missions of the GHG-observing satellites. The Greenhouse gases Observing SATellite (GOSAT) was the world's first satellite designed specifically to monitor GHGs, being uniquely equipped with both shortwave infrared (SWIR) and thermal infrared (TIR) sensors. GHG sensors have been deployed in various orbits: low Earth orbit (LEO), geostationary Earth orbit (GEO), highly-elliptical orbits (HEO), and on the international space station (ISS). This allows a large time range of observations, and will hopefully expand our understanding of GHG variability.

In this section, we focus on the satellite measurements of CO_2 and CH_4 by near infrared (NIR) and TIR remote sensors. Column averages of CO_2 and CH_4 can be obtained from spectroscopic measurements in NIR, and vertical concentration profiles (from 0–20 km height) can be retrieved from the TIR measurements.

→ SWIR band   → TIR band

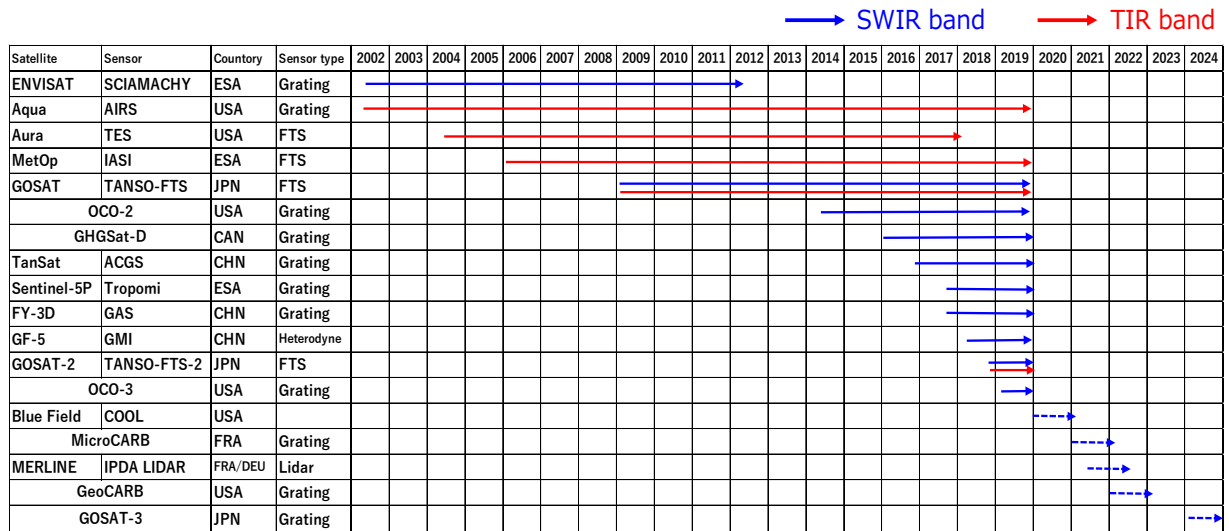| Satellite	Sensor	Country	Sensor type	Timeline
ENVISAT	SCIAMACHY	ESA	Grating	SWIR: 2002–2011
Aqua	AIRS	USA	Grating	TIR: 2002–2019
Aura	TES	USA	FTS	TIR: 2004–2018
MetOp	IASI	ESA	FTS	TIR: 2006–2019
GOSAT	TANSO-FTS	JPN	FTS	SWIR/TIR: 2009–2019
OCO-2		USA	Grating	SWIR: 2014–2019
GHGSat-D		CAN	Grating	SWIR: 2016–2019
TanSat	ACGS	CHN	Grating	SWIR: 2016–2019
Sentinel-5P	Tropomi	ESA	Grating	SWIR: 2017–2019
FY-3D	GAS	CHN	Grating	SWIR: 2017–2019
GF-5	GMI	CHN	Heterodyne	SWIR: 2018–2019
GOSAT-2	TANSO-FTS-2	JPN	FTS	SWIR/TIR: 2018–2019
OCO-3		USA	Grating	SWIR: 2019
Blue Field	COOL	USA		2020 (planned)
MicroCARB		FRA	Grating	2021–2022 (planned)
MERLINE	IPDA LIDAR	FRA/DEU	Lidar	2021–2022 (planned)
GeoCARB		USA	Grating	2022–2023 (planned)
GOSAT-3		JPN	Grating	2024 (planned)

Figure 1.2-1. Summary of the past, current, and future missions of the GHG-observing satellites.

1.2.1. NIR sensor

The SCanning Imaging Absorption spectroMeter for Atmospheric CHartographY (SCIAMACHY) is an ultraviolet (UV), visible (VIS), and NIR grating spectrometer onboard the European environmental satellite (ENVISAT), which observes the atmosphere in nadir, limb, and solar and lunar occultation viewing geometries. The spectral range is 240–2385 nm with a moderate spectral resolution of 0.2-1.5 nm. SCIAMACHY provided the first estimate of the column density for CO_2, CH_4, and CO using NIR spectra. It has a swath width of 960 km (in the scan direction) in width, and a typical footprint of 30 km (along-track) by 60 km (across-track) at the nadir observation. SCIAMACHY instrument was continuously in operation continuously between March 2002 and April 2012 (Buchwitz et al., 2015).

The Greenhouse gases Observing SATellite (GOSAT) launched on 23 January 2009, working regularly throughout orbit. It has two main sensors: a Thermal And Near infrared Sensor for carbon Observation Fourier Transform Spectrometer (TANSO-FTS), and a Cloud and Aerosol Imager (TANSO-CAI). The TANSO-FTS is the Michelson Fourie Transform Spectrometer (FTS) that has three SWIR bands, centered at 0.76 μm, 1.61 μm, and 2.0 μm, and a broad spectral range of 5.5–14.3 μm in the TIR band with a high spectral resolution of 0.2 cm^{-1}. The GOSAT footprint (at the nadir) is 10.5 km in diameter with nominal grid, target, and glint observation modes. Archived from GOSAT include long-term column-averaged and vertical profiles of CO_2 and CH_4 data (Kuze et al., 2009).

The Orbiting Carbon Observatory 2 (OCO-2) was launched in 2 July 2014, into the 705-km altitude Afternoon Constellation (A-train). The orbit is near-polar, sun-synchronous, and take 16-days to complete the ground-track cycle. OCO-2 uses a standard telescope with three long-slit imaging spectrometers that each have diffraction gratings to disperse the incoming light. The three spectrometers cover the O_2-A band at a wavelength of 0.765 μm, a weak CO_2 band at 1.60 μm, and a strong CO_2 band at 2.06 μm. These three channels are called ABO_2, WCO_2, and SCO_2, respectively. The footprint dimensions are determined by the cross-track instantaneous field of view (FOV) of 0.1°, along with an integration time of 0.333 s. For nadir observations, this yields eight cross-track footprints along the spectrometer slit with dimensions 1.29 km × 2.25 km. OCO-2 has been provided the carbon dioxide column-column-averaged dry air mole fraction (XCO_2) data since September 2014 (Crisp et al., 2017).

The GHGSat-D was developed by the Institute for Aerospace Studies/Space Flight

Laboratory (UTIAS/SFL) at the University of Toronto under contract to GHGSat Inc. of Montreal, Canada, and was launched on June 2016. It is the first microsatellite (>15 kg in weight) designed to measure GHGs emissions directly from the point source. GHGSat-D has two sensors: a two-dimensional Wide-Angle Fabry-Perot (WAF-P) imaging spectrometer, and a Clouds & Aerosols (also known as a "C&A") sensor. GHGSat-D orbit is sun-synchronous with an altitude of approximately 500 km, and a cycle of approximately 14 days. The WAF-P sensor has a multispectral SWIR band at 1600-1700 nm, and retrieves column densities of CO_2 and CH_4 with a FOV of approximately 12 km × 12 km and a spatial resolution of less than 50 m (Bradbury et al., 2018).

The TanSat is funded by the Ministry of Science and Technology of the China Earth Observation Program and was launched in December 2016. TanSat has two sensors: an Atmospheric Carbon dioxide Grating Spectrometer (known as ACGS) and a Cloud and Aerosol Polarimetry Imager (known as CAPI). AGGS measures in approximately the same spectral range as OCO-2, with a 2 × 3 km footprint. Its orbit is a sun-synchronous with a local time on ascending node of 13:30, an altitude of ~700 km, and an angle of inclination of 98.2°, which is very close to the NASA A-train. The nominal design life is three years (Yang et al., 2018a). The first global maps of XCO_2 Maps from TanSat were published (Yang et al., 2018b), but the XCO_2 product had not been released at that time.

The TROPOspheric Monitoring Instrument (TROPOMI) was launched in 13 October 2017, aboard the Sentinel-5 Precursor (Sentinel-5P) satellite, with a 7-year design lifetime. TROPOMI is a push-broom grating spectrometer, and measure sunlight in the UV-VIS (270–500 nm), NIR (675–775 nm) and SWIR (2305–2385 nm) bands, with a wide swath of 2,600 km and a ground pixel size of 7 (3.5) × 7 km. The Sentinel-5P orbit is a sun-synchronous orbit at approximately 824 km altitude, with an ascending node equatorial crossing at 13:30. This orbit is behind the Suomi-NPP (National Polar-orbiting Partnership) by 3.5 minutes. The orbit was selected to use the Visible/Infra-red Imager and Radiometer Suite (VIIRS) data for cloud screening. TROPOMI retrieves concentrations of several atmospheric constituents, including CH_4, NO_2, CO, O_3, SO_2, and aerosol properties, with daily global coverage (Haili et al., 2018).

The GOSAT-2 is the successor mission to GOSAT and was launched on 29 October 2018. The main sensors are TANSO-FTS-2 and TANSO-CAI-2. The upgrade points of TANSO-FTS-2 are extending the spectral range to monitor CO concentrations at 2.3 μm, and an intelligent pointing function, to avoid the clouds before the FTS interferogram data are

collected. The target-point observation capabilities have also been enhanced (Matsunaga et al., 2018). GOSAT-2 provides the column-averaged and vertical profiles of CO_2 and CH_4 more precisely than GOSAT and expands the long-term record in this series' mission.

The OCO-3 was launched on 4 May 2019, and docked on the ISS on 6 May 2019. The instrument is mounted on the ISS Japanese Experiment Module-Exposed Facility (JEM-EF). The sensor specification is almost same as OCO-2 and measures XCO_2 with the high precision and spatial resolution, having areal coverage from 51ºS to 51ºN. A two-axis pointing mirror was added, which allows snapshots on the order of 100×100 km for area mapping (Eldering et al., 2019). Deployment on ISS allows sampling during daytime hours, contributing to studies of diurnal variations in megacities, and in tropics and sub-tropical forest, and ocean.

The GHGSat-C1/C2 are a commercial constellations of GHG monitoring satellites and are scheduled to be launch after 2020. The sensors are similar in designs to the GHGSat-D, with improvements applied from critical lessons learned. These include upgrades to mitigate stray light further, ghosting, spectral bandpass inefficiencies, and radiation effects. GHGSat-C1/C2 has equipped the high resolution visible auxiliary camera to check the alignment as a replacement for a cloud and aerosol camera installed in the GHGSat-D (Ligori et al., 2019).

Bluefield Technologies have developed a commercial microsatellite to constellation monitor the CH_4 point emission sources. The orbit is synchronous with a nodal crossing time of local noon ± 90 minute, having a pointing capacity of $\pm 25º$. The sensor is capable of detecting ground leaks at a spatial resolution of 20×20 m. Specifically, the CH_4 Observation Of Lower troposphere (COOL) sensor is a gas filter correlation radiometer (GFCR), which is an instrument also used by the NASA Halogen Occultation Experiment (HALOE) on the Upper Atmosphere Research Satellite (UARS) and the Canadian Space Agency (CSA)/NASA MOPITT instrument on the TERRA spacecraft. The CH_4 absorption band at 2.3 µm, was chosen for its strong absorption compared with that at 1.6 µm. Bluefield Technologies plan to launch its first two microsatellites in 2020 (https://bluefield.co/).

The Methane Remote Sensing Lidar Mission (MERLIN) is a joint mission by the German Space Administration (DLR) and French Space Agency (CNES). DLR is developing and building a methane LiDAR instrument, while CNES is providing the satellite platform and managing the launch and mission control. MERLIN is scheduled for launch in the mid-2024 timeframe. It will be deployed at an altitude of 500 km, having a sun-synchronous orbit with a local time of 06:00/18:00, a 97.4º inclination, and a 28-day revisit cycle. More specifically,

the sensor is an integrated-path differential absorption (IPDA) LiDAR for measuring XCH_4 using the difference in atmospheric transmission between the CH_4 absorption line at 1645.6 nm and a reference wavelength of 1645.8 nm (Ehret et al.,2017).

The NASA Geostationary Carbon Cycle Observatory (GeoCARB) is the first satellite designed to measure the column-averaged of CO_2, CH_4, CO, and solar-induced fluorescence (SIF) from GEO orbit . The instrument will be launched in mid-2022 and hosted on the SES Government Solutions satellite in GEO orbit at 85º±15º W longitude. The sensor is a 4-channels slit imaging spectrometer that measures reflected near-IR sunlight at wavelengths 0.76, 1.61, 2.06, and 2.32 μm. The FOV is 0.15×77 mrad (0.0086º×4.4º) producing a long slit. From an altitude of ~36,000 km, this scanning range covers most of South America, Central America, and North America at latitudes between 50º S and 50 º N at least twice each day (Moore et al., 2018).

1.2.2. TIR sensor

The Interferometric Monitor for GHGs (IMG) was designed to monitor greenhouse gases from space. IMG was part of the Onboard Advanced Earth Observing Satellite (ADEOS) that was launched in 17 August 1996 and operated from June 1997 for a 10-month period. The ADEOS orbit is sun-synchronous with a local time on descending node of ~10:30 AM, an altitude of 789 km, an inclination angle of 98.6º, and revisit cycle of 41 days. The IMG is a nadir-looking Fourier transform infrared spectrometer (FTIR) that measure in the continuous IR spectrum in the range from 3.3–14.0 μm. It has an apodized spectral resolution of 0.1 cm^{-1} with a footprint of 8×8 km in the nadir direction. The 15-μm spectral region is sensitive to CO_2 variations, mainly in the upper troposphere (Ota et al., 2016).

The NASA Aqua Earth Observing System satellite was launched in 4 May 2002. The satellite hosts a hyperspectral instrument suite consisting of an Atmospheric Infrared Sounder (AIRS) measuring in 2378 infrared and 4 VIS/NIR channels, the Advanced Microwave Sounding Unit-A (AMSU-A) instrument measuring in 15 microwave channels, and the Humidity Sounder for Brazil (HSB) instrument measuring in 4 microwave channels. Aqua is part of the NASA A-train constellation, which has a nominal altitude of 705 km and an orbital period of 98.8 min, and approximately 14.5 orbits per day with a local times 13:30 in the ascending orbit. The AIRS measures in the IR spectrum (3.7–15.4 μm) with 2378 channels having a footprint of approximately 13.5 km in diameter at the nadir. The CO_2 algorithm utilizes the 15 μm band in TIR spectrum, which is sensitive in the mid- to upper-stratosphere, and the 4.2 μm band, which is sensitive to mid- to lower-troposphere (Chahine et al.,2008). The AIRS CO_2 data are provided as a research product (Crevoisier et al., 2004).

The Tropospheric Emission Spectrometer (TES) is the NASA A-train orbit with a local time of approximately 13:45, and was launched in 15 July 2004. The TES is designed to monitor the composition in the lowest layers of the atmosphere, directly from space, with a footprint size is 5 km $\times$ 8 km at nadir. TES instrument has a spectral range of 650–2260 cm^{-1}, with a standard resolution of 0.10 cm^{-1}. A finer resolution of 0.025 cm^{-1} is available for special observations. The TES CO_2 retrieval has less than 0.65 degrees of freedom for signal (DOFS) on average. The largest DOFS for daytime land cases is of the order of 1, the least for nighttime or winter land cases is of the order of 0.3, and for ocean targets (day or night), the DOFS is about 0.8. The TES senses between the surface to above 100 hPa, with the most sensitivity between about 700 and 300 hPa, peaking around 600 hPa (Kulawik et al.,2013).

The Infrared Atmospheric Sounding Interferometer (IASI) is onboard the Meteorological Operational Satellite Program (MetOp) of Europe series spacecraft: MeOop-A launched in October 2006, MetOp-B in September 2012, and MetOp-C in November 2018. The MetOp orbit is a sun-synchronous with a descending-node equatorial crossing at 09:30, and an altitude of approximately 817 km. IASI is a FTS with a spectral range of 645–2760 cm^{-1}, an apodized spectral resolution of 0.5 cm^{-1}, and sampling at 0.25 cm^{-1}. The footprint size at the nadir is 50 km $\times$ 50 km, composed of 2×2 circular pixels, each corresponding to a 12-km diameter. IASI channels are mostly sensitive to mid-to-upper tropospheric variations of CO_2 and CH_4 (Crevoisier et al., 2009).

1.3. Purpose and structure of this thesis

The global averaged CO_2 mole fraction exceeded 400 parts per million (ppm, by volume) in 2015 (WMO, 2016). With respect to the atmospheric concentration of 400 ppm, the annual variation of the CO_2 concentration is approximately 2 ppm. To capture small fluctuations in greenhouse gases (GHGs) concentrations on a global scale, spectroscopic observations with radiometric accuracies of 1% or better are required. GOSAT is the world's first satellite to be designed specifically to monitor global GHGs from space. TANSO-FTS on board the GOSAT adopted FTS technology to achieve such high accurate and precise observations, as it has the multiplex advantage (Fellgett advantage) and high optical throughput relative to dispersive instruments. TANSO-FTS is unique in that it includes both solar short-wave infrared (SWIR) and thermal infrared (TIR) band sensors, while previous satellite-borne sensors carried Fourier interferometers covering either SWIR or TIR spectral region. TANSO-FTS detects the scene radiance of SWIR spectra reflected from the Earth's surface and TIR spectra radiated from the ground and the atmosphere for monitoring both column densities and vertical profiles of GHGs. The combined usage of SWIR and TIR bands has an advantage of retrieving partial column densities of the lower and upper troposphere. These data will improve flux estimation by enhancing local emissions and reducing transportation effects. This is a distinguishing feature in the GHGs satellite communities, such as the United States, Europe, and China.

To achieve a precise GHGs observations with both the SWIR and TIR band sensors, the field of view (FOV) of TANSO-FTS is set to be as large as 15.8 mrad. A large FOV can obtain a large number of incident photons, thus high signal-to-noise ratio (SNR) with high spectral resolution. As photo-voltaic detector with the large area was not available for TIR band, TANSO-FTS uses Photo-Conductive HgCdTe (PC-MCT) detector. It covers a wide spectral and dynamic range with a multiplexing system. The data acquired with a PC-MCT detector needs non-linear correction. The correction parameters are dependent on detector temperature and background radiation, which could not be determined only by the pre-launch measurement but also by on-orbit data. This detector is sensitive to thermal condition, and its non-linearity is difficult to characterize only using the onboard blackbody and deep space data. For accurate non-linear correction, it is necessary to know the zero level without input photons and the detector temperature. However, the detector temperature resolution of TANSO-FTS Band 4 is only 0.7 K, and it makes difficult to estimate the background radiation accurately. Since TANSO-FTS performs differential absorption observations, the contamination of the optical instruments can cause signal degradation. Prior to launch, the

spectral transmittance and reflectance, as well as outgassing properties of all materials, were evaluated; then, if necessary, they were changed to materials of low outgassing with little absorption as possible (Kuze et al., 2009). However, several anomalies have affected the thermal conditions of the TANSO-FTS over the long-term operation of GOSAT. This may lead to contamination and, in turn, affect the change of the background radiation from the FTS optics and its environment and, subsequently, produced radiometric errors in the TANSO-FTS TIR spectra.

In this thesis, we describe the TANSO-FTS TIR band calibration and its radiometric validation of radiance spectra. We evaluated the TANO-FTS Band 4 TIR spectra using an aircraft-based FTS and a well-calibrated satellite-borne grating spectrometer and examined the radiometric correction method.

This thesis consists of seven main parts. First, the role of satellite observations in the study of global warming is proposed in chapter 1. The history and current status of GHG satellite measurements are also introduced in this chapter. Chapter 2 describes GOSAT TANSO-FTS in detail, particularly the characteristics of the TANSO-FTS Band 4 PC-MCT detector. A PC-MCT detector is effective to achieve high accurate and precise GHGs observations with the TIR band. However, it is known to have a non-linear response causing critical radiometric errors in quantitative spectroscopic measurements. Chapter 3 outlines the basic theory of TIR remote sensing of the atmosphere and calibration methods. Chapter 4 describes the history of long-term GOSAT operation and the update of the TANSO-FTS Level 1B product. The TANSO-FTS TIR band calibration, including the correction for non-linearity and the complex radiometric calibration method, is also discussed in this chapter. Chapter 5 introduces the TANSO-FTS TIR spectral validation with an aircraft-based FTS sensor from a field campaign. The spectral comparison utilizes the double difference method, which cancels the difference of observation geometries and evaluates the entire spectral range of TANSO-FTS Band 4. Chapter 6 describes the long-term stability of the TANSO-FTS spectral quality using both spectral and sea-surface temperature analysis. In this chapter, we also introduce the revision of the TANO-FTS non-linearity correction. Finally, Chapter 7 summarizes the TANSO-FTS TIR band calibration and covers other remaining issues.

2. Greenhouse Gases Observing Satellite (GOSAT)

The Greenhouse gases Observing SATellite (GOSAT) is a joint project of the Japan Aerospace Exploration Agency (JAXA), Ministry of the Environment (MOE), and the National Institute for Environmental Studies (NIES). GOSAT was the first instrument designed for measuring greenhouse gases, carbon dioxide (CO_2), and methane (CH_4), from space. GOSAT was launched into a sun-synchronous orbit on 23 January 2009. The orbit height is about 666 km with a ground track repeat cycle of 3 days.

GOSAT carries two main sensors: the Thermal And Near infrared Sensor for carbon Observation Fourier-Transform Spectrometer (TANSO-FTS) and the Cloud and Aerosol Imager (TANSO-CAI). TANSO-FTS detects gas absorption spectra reflected solar radiation from the Earth's surface with the shortwave infrared (SWIR) band and thermal emission from the Earth's surface and atmosphere with the thermal infrared (TIR) band. TANSO-CAI uses an ultraviolet (UV), visible, near-infrared, and SWIR bands to obtain cloud and aerosol optical properties.
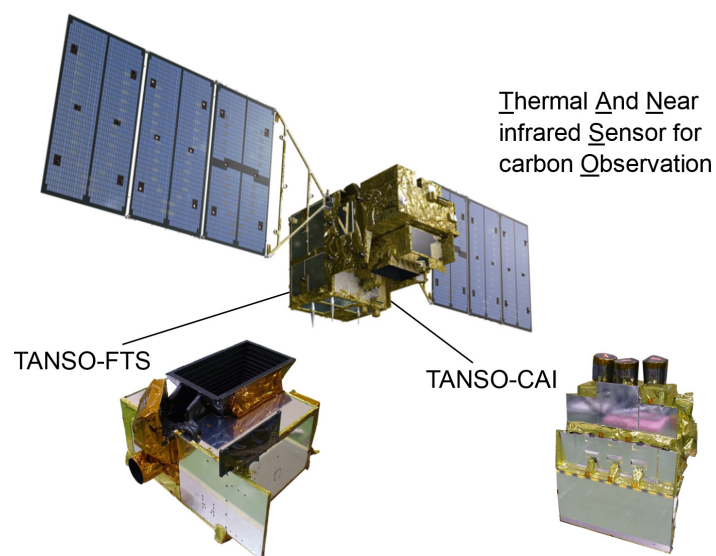

Figure 2-1. Overview photos of the Greenhouse gases Observing SATellite (GOSAT), Thermal And Near infrared Sensor for carbon Observation Fourier-Transform Spectrometer (TANSO-FTS) and the Cloud and Aerosol Imager (TANSO-CAI) (Source: JAXA/EORC GOSAT website).

2.1. TANSO-FTS onboard GOSAT

TANSO-FTS is the Michelson interferometer built by ABB, Inc. in Quebec, Canada. Figure 2.1-1 shows the approximate size of the TANSO-FTS unit. Incident light is modulated by a pendulum-type interferometer with two cube-corner reflectors made from three gold-plated Zerodur plates on an invar structure (Figure 2.1-2). The two cube-corner reflectors are mounted at the edges of a V-shaped swing arm and carefully aligned with each other to permanently maximize modulation efficiency. The rear sides of the cube-corner reflectors are gold coated to minimize thermal radiation coupling with the environment. The swing arm is mounted on the beam splitter holder with a flexible blade and actuated with a rotary motor. The thickness of the beam splitter is selected to be larger than the maximum optical path difference (MOPD) to avoid channeling; its surface has high quality and no anti-reflection (AR) coating to maintain high optical efficiency over a wide spectral range. Bare zinc (Zn)–selenium (Se) material has a spectrally flat index of refraction and transmittance higher than 65% over the wide spectral region from 0.76 to 15 μm (Nakajima et al., 2014). Speed stability of the rotary arm mechanism of the swing arm and interferogram acquisition time are essential factor for obtaining a high signal-to-noise ratio (SNR) and uniform frequency of the modulated output signal. Dichroic filters are used to divide the modulated scene flux into three SWIR bands: two linear polarizations (P/S) and the TIR band. These filters are carefully designed to minimize the polarization sensitivity of the SWIR bands and minimize the TIR background radiation. A silicon (Si) detector is applied for Band 1 and indium-gallium-arsenide (InGaAs) detectors are applied for Bands 2 and 3. The SWIR detectors are cooled to -40° C using three-stage thermoelectric coolers to minimize the dark current. TIR radiation is introduced to a photoconductive (PC) mercury cadmium telluride (HgCdTe or MCT) detector, mounted on the Dewar, and cooled to 72.7 K using a pulse tube high-efficiency cooler (HEC). The spectral sampling interval is about 0.2 cm^{-1}, which is determined at a MOPD of $\pm$2.5 cm. The fully redundant metrology sampling system of TANSO-FTS uses a semiconductor laser of known frequency (1.31 μm), distributed-feedback (DFB) lasers, and two InGaAs detectors. TANSO-FTS is designed to observe the same field location, to compensate for the satellite motion during one-way interferogram acquisition between turnarounds, i.e., image motion compensation (IMC), which is typically takes 4 s.
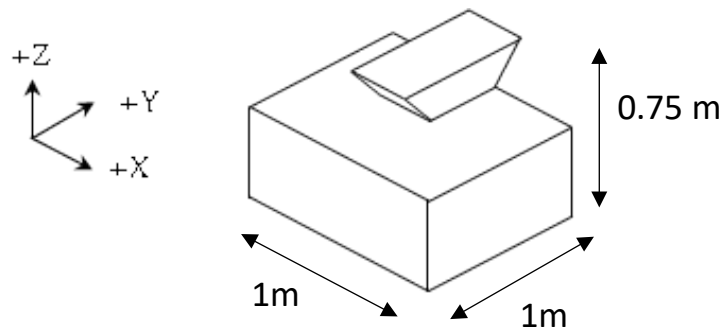
Figure 2.1-1. Schematic of Thermal And Near infrared Sensor for carbon Observation
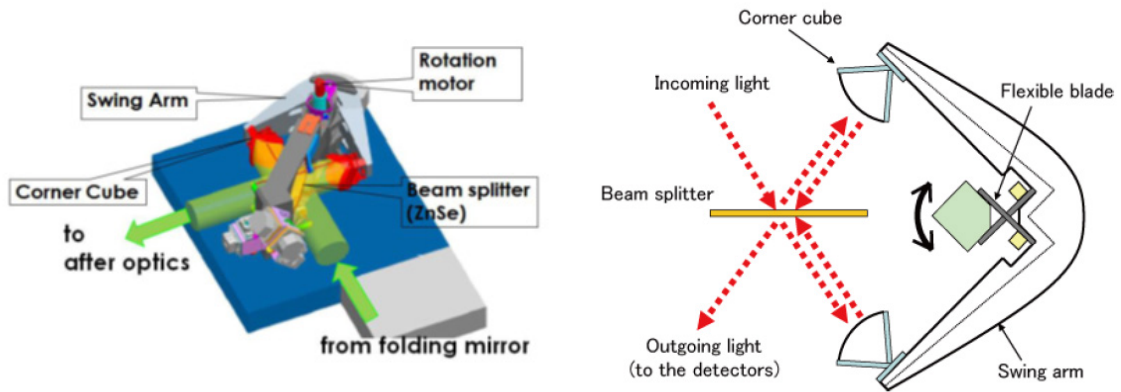Fourier-Transform Spectrometer (TANSO-FTS), indicating its approximate size.

Figure 2.1-2. Michelson of the TANSO-FTS Michelson interferometer
(Source: Nakajima et al., 2014).

The FTS method has several advantages over grating spectrometry. FTS can collect all wavelength spectra simultaneously with a high spectral resolution and better SNR. The spectral range is constrained only by bandpass filters. These sensor characteristics allow for detection of target molecules simply adding the detector. The spectral resolution is determined by the MOPD, and the spectral accuracy and reproducibility are determined by a standard laser.

In grating spectrometry, resolving power of a grating spectrometry, resolving power is the theoretical concept of separating adjacent spectral lines of equal intensity according to the Rayleigh criterion. The resolving power depends on the grating width, the number of grooves per grating, and spectral wavelength. However, the actual resolvable spectral wavelength difference is also affected by the light source, slit width, and other optical parameters. Diffraction grating of a spectrometer is usually applied near the blaze wavelength, to maximize

the diffraction efficiency; however, multiple diffraction grating may be performed to increase the efficiency of light utilization efficiency over a wide wavelength range. The instrumental line shape (ILS) function of FTS is relatively simple compared to the grating spectrometry, in which the diffraction peaks are sensitive to wavelength.

Table 2.1-1 shows the specifications of TANSO-FTS. The TANSO-FTS sensor has three SWIR bands, including an oxygen A-band (O$_2$A) near 0.76 μm, and the weak and strong CO$_2$ bands near 1.6 μm (Weak-CO$_2$), and 2.06 μm (Strong-CO$_2$), with two linear polarizations [P and S], respectively; it also has one TIR band, covering a wide spectral range (650–1,800 cm^{-1} (Figure 2.1-3).

Figure 2.1-4 shows the TANSO-FTS optics layout. The optics unit consists of a pointing mechanism, a beam splitter, complementary metal oxide semiconductor (CMOS) image sensor camera (CAM), relay optics, TANSO-FTS aft-optics mechanism, detectors, and analog-signal processors. Figures 2.1-5 and 2.1-6 show interior views of the TANSO-FTS optics system. The solar diffuser plate is mounted at the top of the cover and used for solar irradiance calibration. The black body and deep space window are mounted on the sidewall and used mainly for TIR spectral calibration.

TANSO-FTS has a two-axis pointing mechanism (cross-track [CT], ±35°, along-track [AT], ±20°), and an instantaneous field of view (IFOV) of 15.8 mrad, which corresponds to a ground footprint approximately 10.5 km in diameter at nadir observation. Figure 2.1-7 shows the nominal TANSO-FTS grid observation pattern. GOSAT nominal observation is initially set for five-point CT scanning. However, the primary pointing system has a pointing offset that cannot be detected using an angular resolver (Kuze et al., 2012). The pointing mechanism was therefore changed to a nominal three-point CT scanning mode over land in August 2010 (Figure 2.1-8). The settling time of AT pointing in the primary system began to worsen starting in September 2014; therefore, the pointing system was switched from primary to secondary in January 2015. Secondary pointing is relatively stable, with a pointing offset that is almost negligible. In addition to the nominal grid pattern, GOSAT has a target mode function that uses an agile pointing system and glint mode for ocean targeting. Using this system, GOSAT can obtain unique observations over major emission sources and calibration/validation sites.

GOSAT is equipped with a total of eight monitor cameras (CAM-H1~H8) to check the deployment of solar array paddles and antennas, the presence of contamination during the fairing and satellite separation, and the status of the satellite in orbit. One of them (CAM-

H8) was installed to check the field of view of TANSO-FTS, because FTS does not have an inherent imaging capability. Table 2.1-2 shows GOSAT CMOS camera (CAM-H8) specification. The camera captures at least one image during FTS interferogram acquisition in daytime observation, at a spatial resolution better than 100 m (Nakamura, 2010). Cloud-contaminated scenes can be filtered using these camera images (Figure 2.1-9).

Table 2.1-1. TANSO-FTS specifications.

Observation rang	Cross Track: +/- 35 deg., Along Track: +/- 20 deg.			
Data sampling	4.0, 2.0, 1.1, 2.0, sec/interferogram			
Aperture diameter	68 mm			
FOV	15.8mrad. , 10.5km (Nadir)			
MOPD	±2.5 cm, 0.2 cm^{-1}			
Band	Band 1	Band 2	Band 3	Band 4
Wavelength [μm]	0.75 – 0.77	1.56 – 1.72	1.92 – 2.08	5.5 – 14.3
wavenumber [cm^{-1}]	12900 – 13200	5800 – 6400	4800 – 5200	700 – 1800
SNR (measured)	>340	>320	>410	>280
Detector	Si	InGaAs	InGaAs	PC-MCT
Onboard calibration	Solar irradiance, Lunar, Deep space (Radiance) Diode laser (ILS)			Black body, Deep space (Radiance)

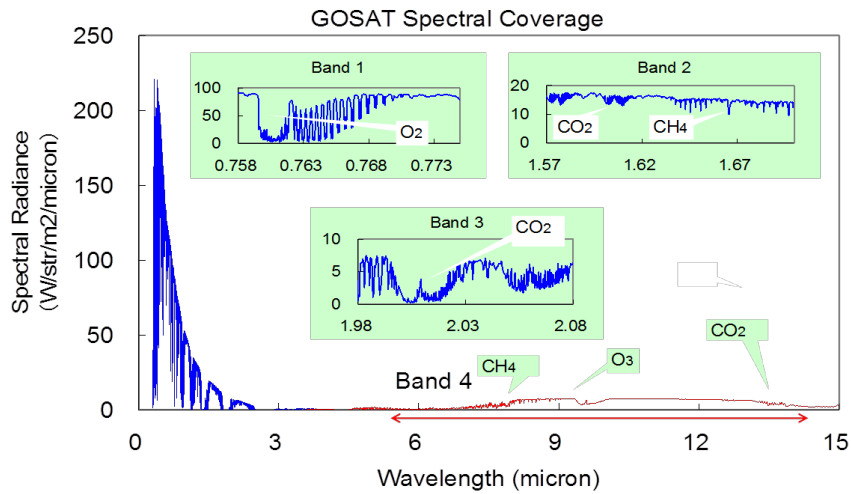Figure 2.1-3. TANSO-FTS spectral coverage
(Source: JAXA/EORC GOSAT website).
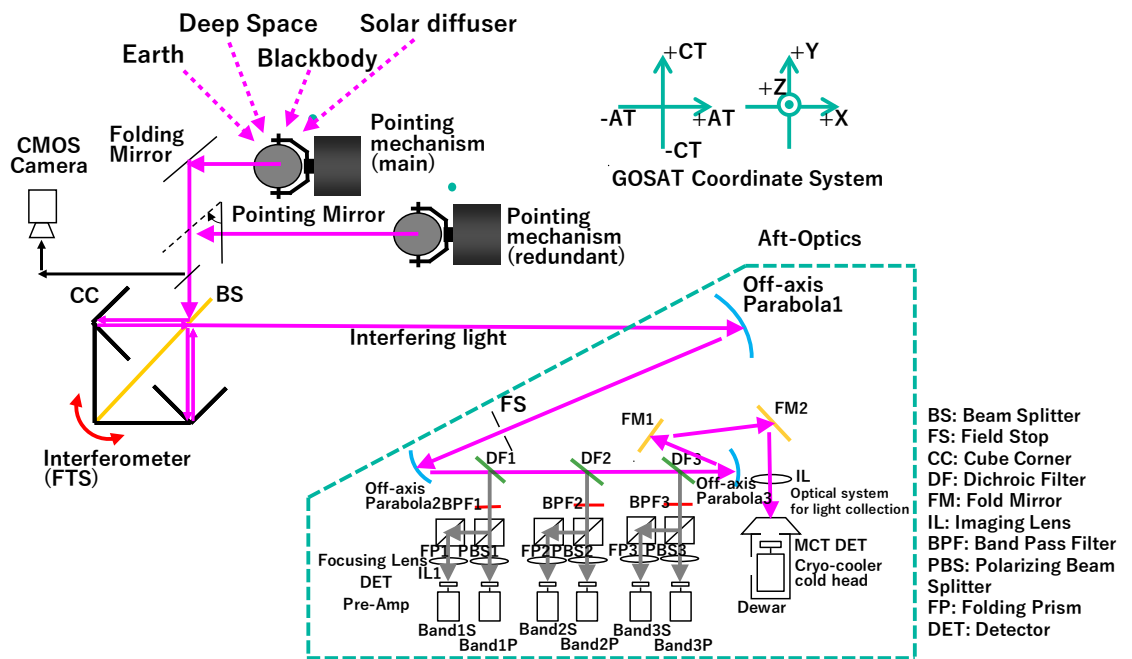
Figure 2.1-4. TANSO-FTS optics layout (Source: NEC corporation document).
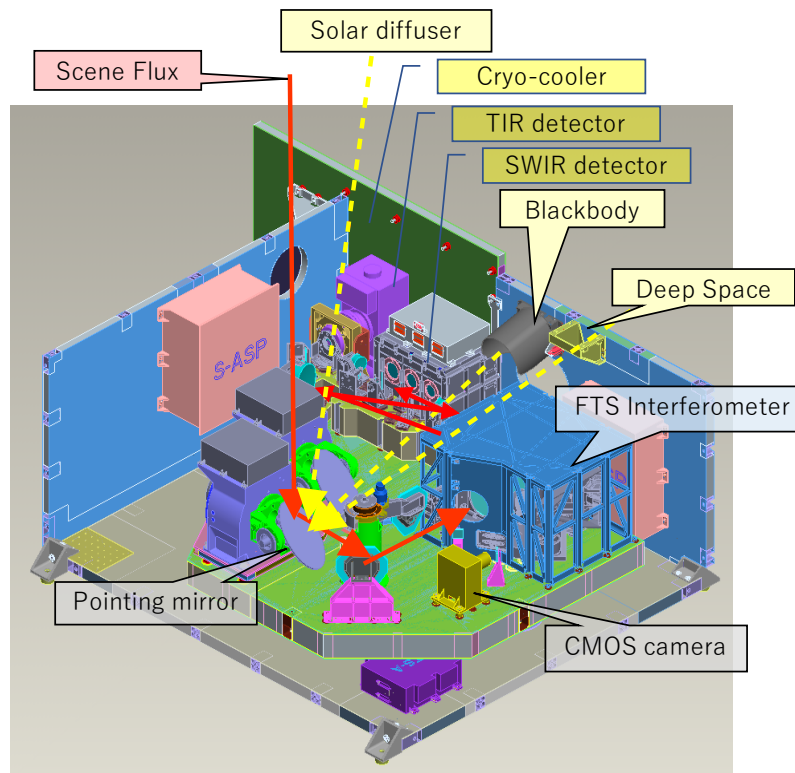
Figure 2.1-5. Interior view of TANSO-FTS optics view inside and optical path
(Source: NEC corporation document).
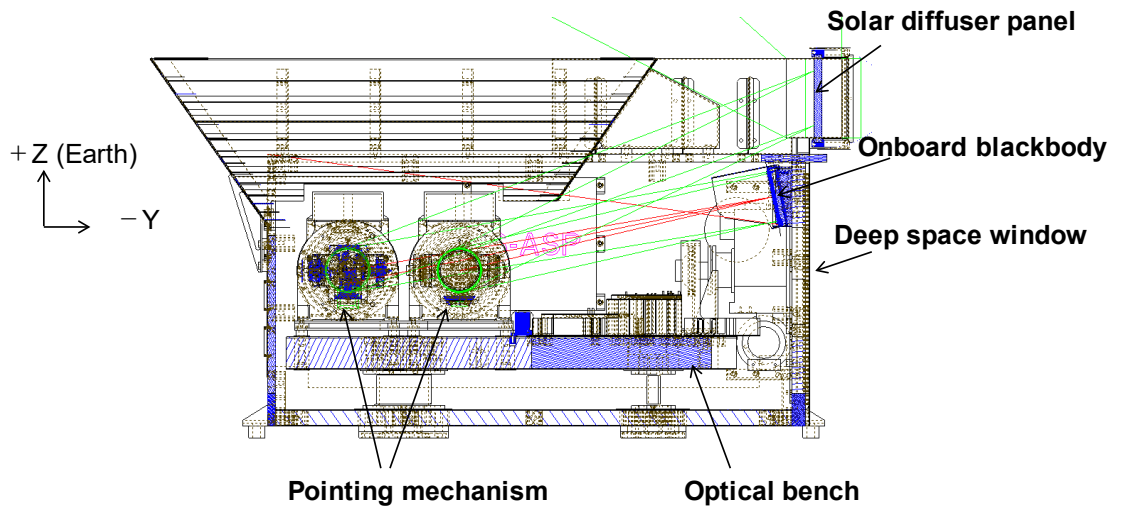
Figure 2.1-6. Side vies of TANSO-FTS optics
（Source: NEC corporation document）.
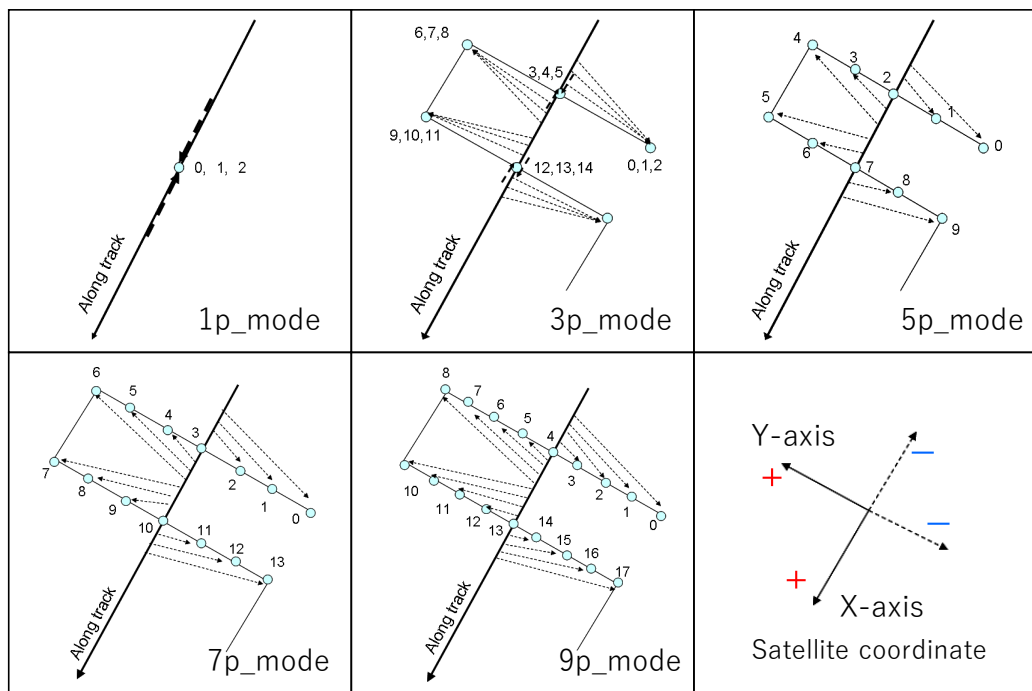
Figure 2.1-7. TANSO-FTS grid observation pattern.
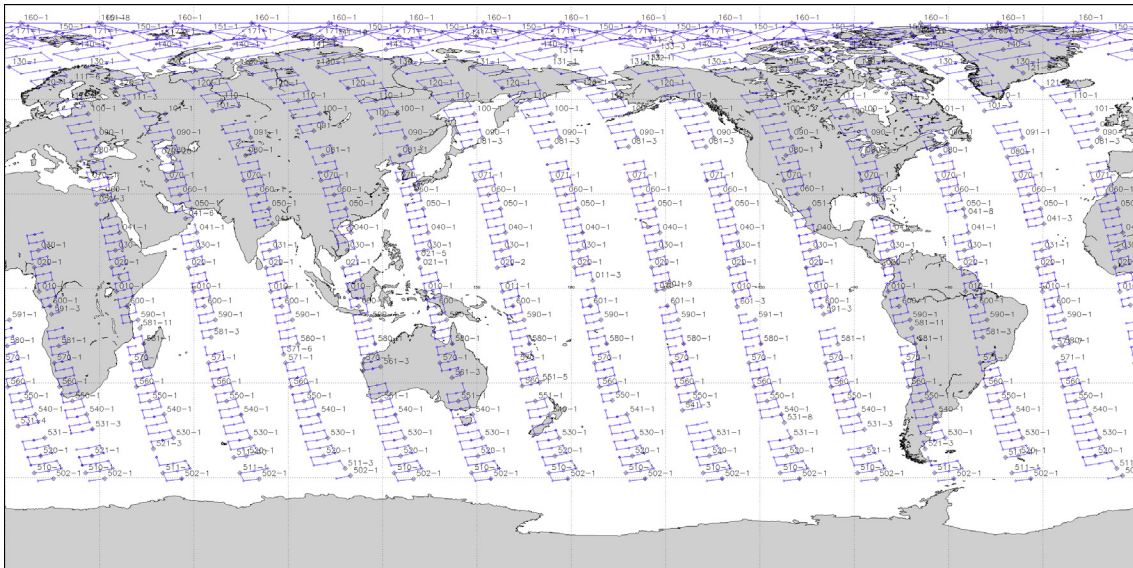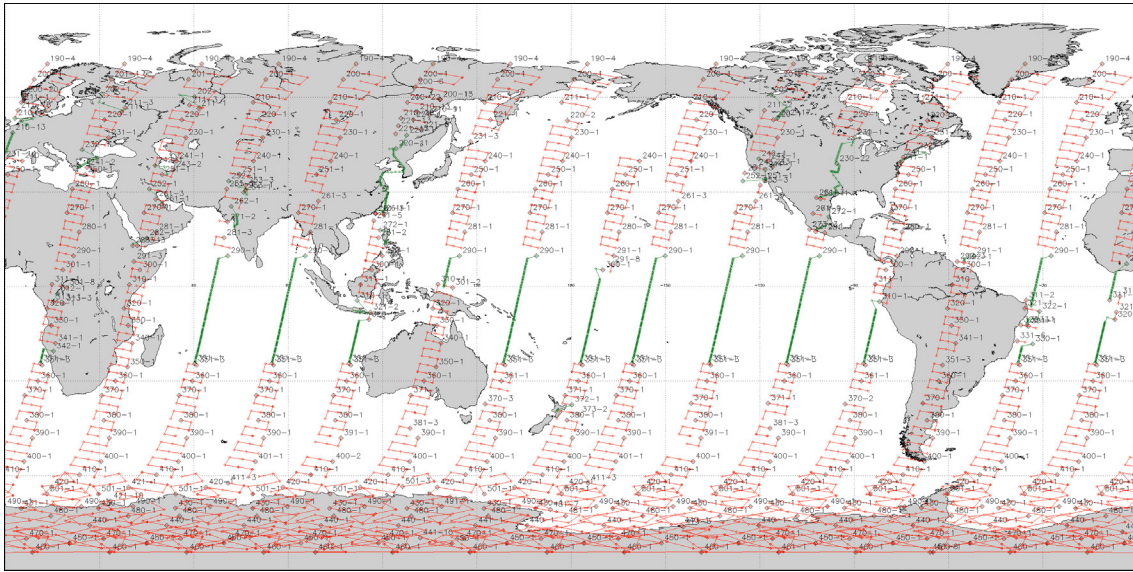
Figure 2.1-8. TANSO-FTS observation map on 1 January 2013. Top panel shows a dayside observation; bottom panel shows a nightside observation. Red and blue dots show nominal three-point cross-track scanning mode; green plots show target mode, including the emission source, calibration/validation sites, and sunglint.

Figure 2.1-9. Overview of the two-dimensional complementary metal oxide semiconductor image sensor (CMOS) camera (CAM) and an image captured near Nagoya, Japan (image credit: JAXA).

Table 2.1-2. TANSO-FTS CMOS camera (CAM-H8) specifications.

Dimensions	90 mm × 130 mm × 127 mm
Weight	0.8 kg
Power consumption	1.7 W（nom）, 3.8 W（max）
Permissible temperature	-20 °C ~ 45 °C
Effective pixel	approx.1.3 million pixels
Imaging device	1 / 3.3 type CMOS color
Focal length	45.5 mm
Brightness	F9.1
Viewing angle	5.32°×4.26°（SXGA）, 5.32°×3.99°（VGA_SKIP）
Object distance	35 m ~∞
Recording pixels	1280×1024（SXGA）, 640×480 (VGA_CUT, SKIP)
Frame rate	SXGA, VGA_CUT：(max) 6.6 fps, VGA_SKIP：(max) 26.6 fps
Shutter speed	Auto, Manual：$1/2^n$（n＝1~12）s
Compaction function	JPEG: 15 steps variable

2.2. TANSO-FTS infrared detector

Infrared detectors are classified into quantum and thermal types. Quantum infrared elements detect light based on the interaction between charges and photons in a semiconductor, whereas TIR elements detect the temperature of the element according to the absorption of infrared rays. Quantum infrared detectors have higher response and sensitivity levels than thermal elements. Disadvantages of the quantum type include high cost, power consumption, and system size due to the necessity of a large cooling unit, which also carries the risk of micro-vibration. Thermal detector performance is lower than that of the quantum detector; however, the thermal system is compact and lightweight due to elimination of the cooling unit. Because thermal detectors can be mass-produced at low cost, they are in high demand as consumer products. Table 2.2-1 lists the characteristics of both types of infrared detector (Rogalski, 2011; Hamamatsu Photonics, 2011). Infrared detectors are used for a wide range of applications in various fields, including thermometer applications, laser detection, and spectrometry (Table 2.2-2).

Table 2.2-1. Infrared detectors; types and characteristics.

Type			Detector	Spectral Response	Operating Temperature
Thermal type	Thermocouple Themopile Bolometer Pneumatic cell Pyroelectric detector				300
Quantum type	Intrinsic type	Photoconductive	InSb	$2-6$	213
			HgCdTe	$2-20$	77
			PbS	$1-3.6$	300
			PbSe	$1.5-5.8$	300
		Photovoltaic	InSb	$1-5.5$	77
			InAs	$1-3.1$	77
			HgCdTe	$2-12$	77
			Ge	$0.8-1.8$	300
			InGaAs	$0.7-1.7$	300
	Extrinsic type		Ge : Au	$1-10$	77
			Ge : Hg	$2-14$	4.2
			Ge : Nu	$2-30$	4.2
			Ge :Zn	$2-40$	4.2
			Si : Ga	$1-17$	4.2
			Si : As	$1-23$	4.2

Table 2.2-2. The applications of infrared detectors.

Application \ Detector	InAs	InSb	Ge	HgCdTe	PbS	PbSe	InGaAs
Temperature Sensors	X	X	X	X	X	X	X
Radiometers	X	X	X	X	X	X	X
FTIR Spectroscopy	X	X		X			X
Pulsed Laser Monitors	X			X			X
CO2 Laser Detection				X			
Laser Diode Control			X				X
Spectrometry	X	X	X	X	X		X
NDIR Spectroscopy					X	X	
Flame Spectroscopy					X	X	
Optical Pyrometry					X	X	
Thermal Imaging		X		X			
Heat-Seeking Guidance		X		X			X
Optical Power Meters	X						
Industrial Process Control				X			
Environmental Gas Analysis						X	X

Quantum cooling infrared sensors are designed using intrinsic or extrinsic semiconductors and can be either photovoltaic (PV) or PC. Intrinsic detectors generally operate at higher temperatures, have higher quantum efficiency, and dissipate less power than extrinsic devices. In the longer-wavelength region, PC detectors operate in extrinsic mode. Extrinsic materials include Si and germanium (Ge), doped with arsenic (As), copper (Cu), gold (Au), or indium (In). Extrinsic detectors require considerably more cooling than intrinsic detectors to achieve high sensitivity and suppress noise. The most popular intrinsic detectors are constructed using HgCdTe (MCT) and indium antimonide (InSb). InSb-based detectors have the most stable performance at wavelengths < 5 μm, and operate at about 77 K. Intrinsic HgCdTe detectors are most common at short wavelengths (< 20 μm) and are often adopted for intrinsic PV and PC detectors. PC detectors are based on the PC effect, in which the generation of a charge by infrared radiation decreases the resistance of the semiconductor active region. This resistance change is sensed as a voltage change on application of a constant current bias. The current bias, which flows in the detector when it does not receive light, is dependent on the operating temperature and spectral characteristics. PV detectors are based on the PV effect, i.e., the creation of voltage and electric current in the semiconductor upon exposure to light.

The PC-MCT detector shows a non-linear response to photon flux, causing radiometric errors and undesirable spectral artifacts in quantitative spectroscopy measurements, whereas the PV-MCT detector has a better linear response. Voltage is generated in proportion to the amount of light; however, the FTS sensor often incorporates an PC-MCT detector, because

the PV-MCT detector accommodates a narrower spectral band (5–12 μm) than the PC-MCT detector (~20 μm) and requires significant production time and cost (Abe et al., 1998). Applications of these MCT detectors for infrared spectrometry in space are listed in Table 2.2-3.

Table 2.2-3. Mercury–cadmium–telluride (MCT)-based infrared detector applications.

	Imager	Spectrometer
PV-MCT	Terra/ASTER Terra/MODIS Aqua/MODIS GCOMC/SGLI	Aqua/AIRS Aura/TES MetOp/IASI Sentinel-5P/TROPOMI ISS/HISUI GOSAT-2/TANSO-FTS-2
PC-MCT	Terra/MODIS Aqua/MODIS	Aqua/AIRS MetOp/IASI GOSAT/TANSO-FTS GOSAT-2/TANSO-FTS-2

GOSAT/TANSO-FTS Band 4 has adopted an PC-MCT detector. This detector is often used for TIR remote sensing at high spectral resolution. PC-MCT exploits the physical property whereby electric resistance changes in a negative relationship with incident light, such that the resistance value of the PC-MCT detector decreases more slowly as incident light increases. The conductive response of the MCT detector is proportional to the 1/3 power of incident light intensity (Bartoli et al., 1974).

Regardless of the illumination of the detector, its series resistance can cause nonlinearity. Detector nonlinearly distorts the true interferogram, especially in the center burst region, where the most significant photon flux variation occurs. Figure 2.2-1 shows a schematic of the distortion of interferogram measurements with a nonlinear photon flux response. Photon flux incoming to a detector can be separated into a modulated AC component and a non-modulated DC component. Thus, the interferogram can be written as follows:

$$I(x) = I^{AC}(x) + I^{DC}$$
$$I_m(x) = I_m^{AC}(x) + I_m^{DC}$$
$$I(x) = \eta \left(I_m(x) \right),$$

<div align="right">(2.2-1)</div>

where I is the true interferogram, and I_m is the measured interferogram, which has been

perturbed by nonlinearity. The interferogram consists of DC component I^{DC}, which is independent of the optical path difference x, and the varying AC components $I^{AC}(x)$. The DC component is defined as constant offset, including photon fluxes from the scene and optical components. η is the nonlinear detector response to input photon flux.

Nonlinearity coefficients are assumed to remain constant under stable detector operating conditions, i.e., constant instrument temperature. Different orders of the nonlinear detector response have been proposed, including second-, third-, and high-order responses (Iwata et al., 1997), as follows:

$$I(x) = I_m(x) + aI_m + bI_m^2(x) + cI_m^3(x) + \text{high orders.}$$
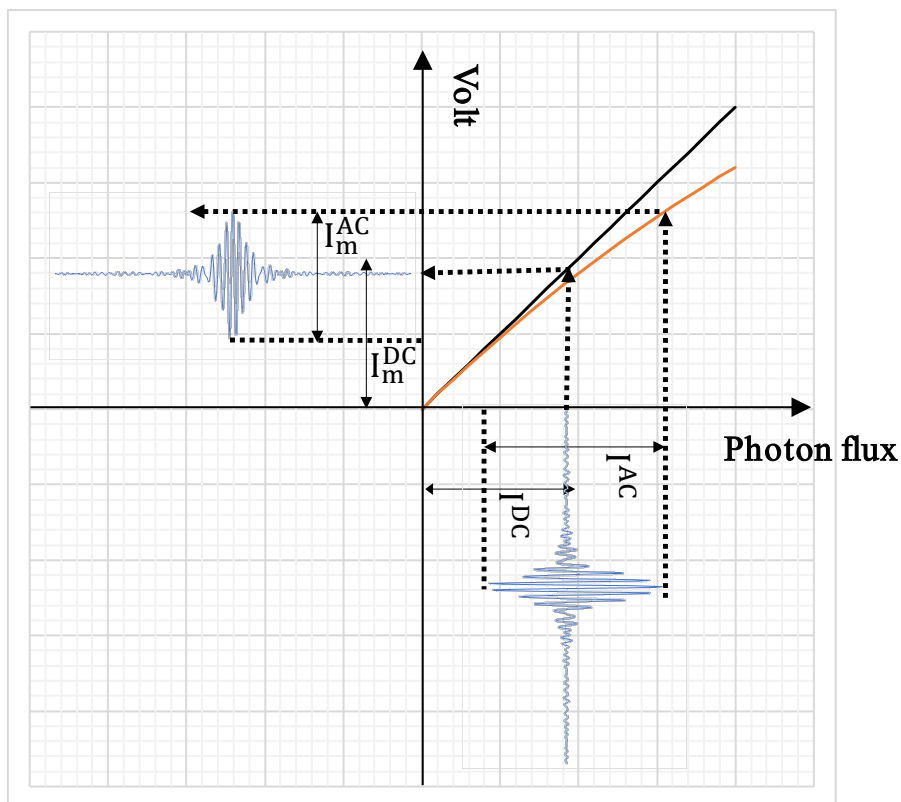
$$(2.2\text{-}2)$$

Figure 2.2-1. Schematic of the photoconductive mercury–cadmium–telluride (PC-MCT) detector non-linearly. I is the true interferogram and I_m is the measured interferogram, which has been perturbed by nonlinearity. The interferogram consists of a modulated (AC) component and a non-modulated (DC) component.

Effective correction of the nonlinearity of the interferogram is performed using out-of-band and in-band methods.

The out-of-band method estimates the coefficients by minimizing out-of-band signals, which occur below the detector cut-off frequency. This process virtually eliminates the response to incident radiation. Nonlinear characteristics of the PC-MCT detector and electronic signal processing circuitry affect signals above and below the cut-off frequency; therefore, Keens et al. (1990) suggested that two correction factors should be calculated using Fourier-transform spectrometry.

The first correction factor is determined by linear fitting to the portion of the spectrum below the cut-off frequency and extrapolating this linear fit to a frequency of zero. The correction factor is calculated by dividing the signal at zero frequency by the integral of the square of the portion of the spectrum above the cut-off. The second correction factor is a function of the first correction factor and the integral of the spectrum signal above the cut-off. Both corrections factors are then used to calculate a second-order approximation, to correct the interferogram.

In the in-band method, nonlinearity coefficients are calculated from three reference measurements with different brightness temperatures (Lachance et al., 1998). The common radiance measured by FTS can be expressed as:

$$F\{\eta(I_m)\} = \bar{G}(L + \bar{O}),$$

(2.2-3)

where F is the Fourier transform operator, which converts interferograms into equivalent spectra, $\bar{G}$ is the responsivity (gain) of the instrument, L is the true incident spectral radiance from the scene, $\bar{O}$ is the instrument emission (offset), and overbars indicate complex quantities, comprising a real part and an imaginary part.

Gain can be determined using two non-equivalent calibration observations of hot and cold temperature(T_H and T_C, respectively), which are expressed as:

$$\bar{G} = \frac{\bar{M}_H - \bar{M}_C}{L(T_H) - L(T_C)},$$

(2.2-4)

where $\bar{M}_H$ and $\bar{M}_C$ are the uncalibrated complex spectrum obtained by hot and cold temperature measurement.

If the nonlinearity coefficient η is to be expressed with only one coefficient, three different measurements are required to solve Eq. (2.2-3). Solving for the gain, we obtain the following relation:

$$\frac{F\{\eta(I_M) - \eta(I_C)\}}{L(T_M) - L(T_C)} = \frac{F\{\eta(I_H) - \eta(I_C)\}}{L(T_H) - L(T_C)} \, ,$$

$$(2.2\text{-}5)$$

where T_M is the third measurement made at a temperature $T_C \neq T_M \neq T_H$. To solve this equation for η, we apply the simplex minimization algorithm (Caceci et al., 1984) to the residual form of the modified Eq. (2.2-5), as follows:

$$Minimize \left\{ \sum_{\sigma=\sigma_{min}}^{\sigma_{max}} \left[\left| \frac{F\{\eta(I_M) - \eta(I_C)\}}{F\{\eta(I_H) - \eta(I_C)\}} \right| - \left(\frac{L(T_M) - L(T_C)}{L(T_H) - L(T_C)} \right) \right]^2 \right\}.$$

$$(2.2\text{-}6)$$

The sums of squared residuals are computed between specific spectral limits, defined as σ_{min} and σ_{max}. These values can be set as the physical spectral limits of the detector, or restricted to a shorter range to increase precision for specific measurements. In this manner, the correction can be tailored for greater effectiveness over a given spectral range.

3. Thermal infrared spectrometer calibration methods

3.1. Thermal infrared remote sensing of the atmosphere

Earth's energy budget is a balance between incoming solar radiation and outgoing earth radiation. Solar radiation is concentrated at shorter wavelengths with a peak at 0.5 μm, called shortwave radiation. Earth radiation has a peak at the longer wavelength of 10 μm and is called longwave radiation or thermal radiation.

The spectral distribution of Earth's thermal radiation can be discussed based on the following fundamental laws:

Planck's law states that spectral radiation emitted from a blackbody at a specific wavelength is a function of the temperature of the blackbody.

$$B_\lambda(T) = \frac{2hc^2}{\lambda^5 \left(e^{\frac{hc}{k\lambda T}} - 1 \right)}$$

(3.1-1)

B_λ : Spectral radiance of blackbody $[W/m^2/\mu m]$

h : Planck constant = 6.626×10^{-34} Js

c : Speed of light = 2.9989246×10^8 m/s

λ : Wavelength [μm]

k : Boltzmann constant = 1.3806×10^{-23} J/K

T : Temperature [K]

The Stefan-Boltzmann law states that total radiation emitted by a blackbody is a function of temperature.

$$I = \sigma T^4$$

(3.1-2)

I : Total radiance $[W/m^2]$

σ : Stefan-Boltzmann constant = 5.6697×10^{-8} $W/m^2/K^4$

T : Temperature [K]

Wien's displacement law allows determination of the wavelength at which the maximum spectral radiance is emitted from a blackbody.

$$\lambda_{max} = \frac{C}{T}$$

(3.1-3)

λ_{max}: wavelength of maximum spectral radiance [μm]

C: Wien's constant =2.8978×10^{-3} mK

T: temperature [K]

Kirchhoff's law states that absorptivity of a material is equal to its emissivity under the condition of thermal equilibrium.

$$\varepsilon_\lambda = \alpha_\lambda$$

(3.1-4)

ε_λ : material emissivity

α_λ : material absorptivity

The total radiation flux including absorption, reflection, and transmission is equal to unity.

$$\alpha_\lambda + \rho_\lambda + \tau_\lambda = 1$$

(3.1-5)

ρ_λ : material reflectance

τ_λ : material transmittance

The radiative property of most materials is opacity, meaning the transmittance of the material is zero. Based on Kirchhoff's radiation law, α_λ can be replaced with ε_λ as follows.

$$\varepsilon_\lambda = 1 - \rho_\lambda$$

(3.1-6)

The emissivity of a material is an important factor for determining the thermal radiation leaving the material. The emissivity depends on surface temperature, surface type, surface conditions, viewing zenith angle, and wavelength. The Advanced Spaceborne Thermal Emission Reflection Radiometer (ASTER) project provides a spectral library for a variety of materials over the wavelength range of 0.4–15.4 μm (Baldridge et al., 2009). The library

includes the spectra of rocks, minerals, soils, vegetation, snow, ice, and anthropogenic materials. This library is widely used in studies of geology and thermal infrared remote sensing. Figure 3.1-1 shows the emissivity of typical natural materials and is reproduced from the ASTER spectral library.
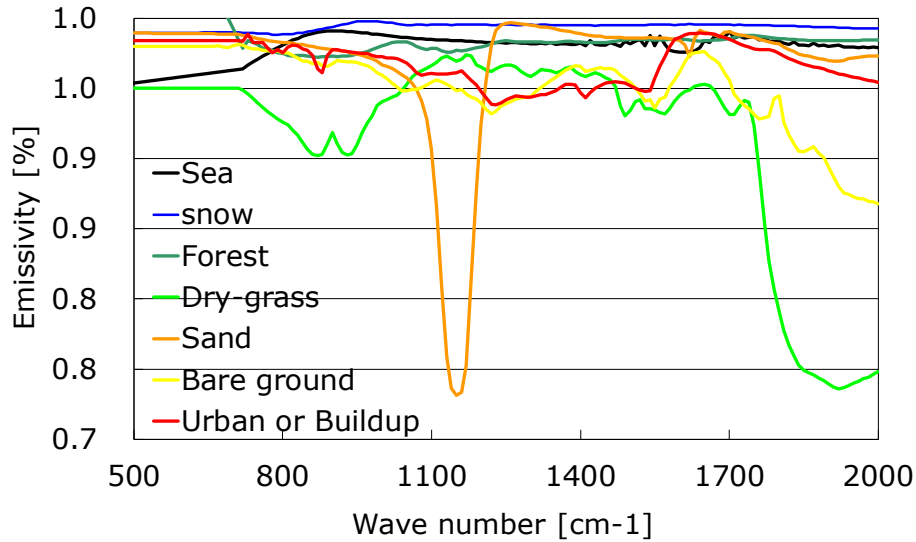
Figure 3.1-1. Emissivity of a variety of materials reproduced from the ASTER spectral library.

Figure 3.1-2 shows the Earth's thermal spectral radiance, with Planck curves at 300, 310, and 320 K. The spectrum of Earth's thermal radiation within the spectral range of 8–12 μm is relatively transparent. However, some atmospheric absorption is present, in particular for CO_2 at 4.5 and 15 μm, H_2O at 6.3 and 12.0 μm, O_3 at 9.6 μm, and CH_4 at 7 μm.

Figure 3.1-2. Intensity spectra of Planck radiation and Earth's thermal radiation.

The Earth's thermal spectral radiance ($L(\lambda)$), with reference to surface temperature and emissivity, can be observed with a sensor and expressed with the following equation.

$$L(\lambda) = \varepsilon(\lambda)\, L_B(\lambda, T)\, \tau(\lambda) + L_u(\lambda) + \frac{\left(1 - \epsilon(\lambda)\right) L_d(\lambda)\, \tau(\lambda)}{\pi}$$

(3.1-7)

L : Spectral radiance $[\text{W/m}^2/\text{str}/\mu\text{m}]$

λ : Wavelength $[\mu\text{m}]$

ε : Emissivity of the surface
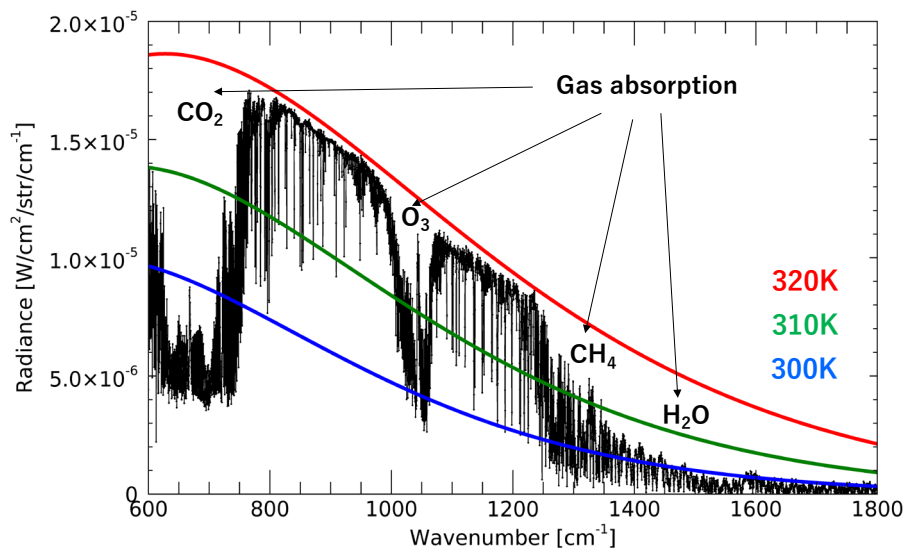
T : Surface temperature $[\text{K}]$

L_B : Radiation emitted from the surface

τ : Transmission of the atmosphere

L_u : Atmospheric upwelling radiation

L_d : Downwelling radiation

The first term on the right side of equation (3.1-7) represents the radiation emitted from a surface with emissivity ε and the surface temperature T. The second term is atmospheric upwelling radiation, and the third term is downwelling radiance reflected at the surface (1- ε). Radiation emitted and reflected from the surface experience different absorption and emission processes in individual atmospheric layers.
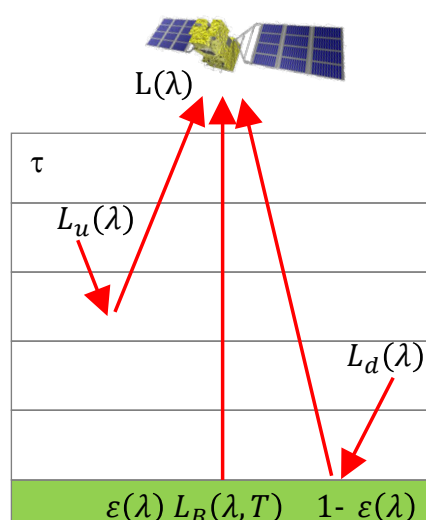

Figure 3.1-3. Thermal infrared radiation observations.

The radiative transfer model (RTM) is used to calculate theoretically the thermal infrared radiation attenuated through each layer. RTM allows calculation of the radiation at the top of the atmosphere (TOA) from a satellite-borne sensor or a specific height from an airborne sensor with specified observation geometry. Any radiation value is an average of the monochromatic radiances, as expressed in equation (3.1-7). Line-by-line (LBL) calculation exploits the accuracy of transmittance and radiance spectra at each frequency with a nominal spectral sampling rate of less than the mean line half-width using a spectroscopic database (line parameter) and atmospheric information (vertical profiles of meteorological parameters and atmospheric composition).

Here, we described the LBL-based RTM covering the thermal infrared spectral range at high spectral resolution.

・RFM (Reference Forward Model)

RFM is the LBL radiative transfer model initially developed at Oxford University and currently supported by the UK National Centre for Earth Observation (Dudhia, 2017). The general purpose of RFM is to provide reference spectra for the limb-viewing infrared Fourier-transform spectrometer MIPAS (Michelson Interferometer for Passive Atmospheric Sounding) onboard ENVISAT (Bormann et al., 2006). This model was developed based on GENLN2 (General Line-by-Line Atmospheric Transmittance and Radiance Model). RFM has an extended spectral range from infrared to microwave wavelengths and is suitable for a variety of spectroscopic calculations. The current RFM employs HITRAN spectroscopic data; this is described later in this chapter.

・KOPRA (Karlsruhe Optimized and Precise Radiative transfer Algorithm)

KOPRA is an LBL radiative transfer code developed by the Karlsruhe Institute of Technology (KIT), Germany (Stiller et al., 2000). It was designed to provide a stand-alone algorithm, including all relevant physics from the troposphere to the thermosphere as well as the specific response function of the MIPAS/ENVISAT instrument. The model carried out not only the forward calculation of infrared atmospheric transmittance and radiance spectra but also retrievals of limb- and upward-viewing instruments.

・ARTS (Atmospheric Radiative Transfer Simulator)

ARTS is a radiative transfer model that simulates the infrared energy flux in the millimeter and sub-millimeter spectral range. Its core development was conducted at the University of Hamburg, Germany, and Chalmers University, Sweden (Buehler et al., 2005, Eriksson et al.,

2011). The first version of the model, ARTS-1, was a traditional microwave to infrared forward model with no treatment of scattering. The current version of ARTS includes the scattering process and, optionally, polarization effects. The viewing geometries handled by this model include upward, limb and downward angles.

・4A (Automatized Atmospheric Absorption Atlas)

The 4A model has been discussed in the framework of the international radiative transfer community since the 1980s (Scott et al., 1981). The operational version of 4A (4A/OP) has been used as the official radiative transfer model for IASI level 1 calibration and validation processing (online: http://ara.abct.lmd.polytechnique.fr/index.php?page=4a#3). 4A is a pseudo line-by-line radiative transfer model with a spectral range of 600–3000 cm^{-1} and spectral resolution of 5.10^{-4} cm^{-1}. The 4A concept is a compressed look-up-table (LUT) of optical depths with 15 cm^{-1} blocks, which is associated with thousands of combinations of spectral steps, layers, temperatures, and gas species.

・MODTRAN (MODerate resolution atmospheric TRANsmission)

MODTRAN was developed by Spectral Sciences, Inc. (SSI) and the Air Force Research Laboratory (AFRL) and is widely used for atmospheric research. MODTRAN is used to calculate atmospheric spectral transmittances and radiances from the ultraviolet (UV) through the long-wavelength infrared spectral region (0–50,000 cm^{-1}) with high spectral resolution (>0.2 cm^{-1}) (Berk et al., 2014). The core of the MODTRAN radiative transfer (RT) calculation is an atmospheric "narrow-band model" algorithm, and the current version of MODTRAN includes a line-by-line algorithm for high-resolution RT calculations (Berk et al., 2015).

・RTTOV (Radiative Transfer for TOVS)

RTTOV was developed to enable the direct assimilation of radiances during the 1990s at the European Centre for Medium-Range Weather Forecasts (ECMWF) to enable direct assimilation of radiances and was used for the initial development of the TIROS operational vertical sounder (TOVS) radiometers (Saunders et al., 2018). RTTOV is used for simulations of top-of-atmosphere radiances measured by several instruments in the microwave (MW), infrared (IR) and visible (VIS) spectral regions. RTTOV allows the option of line-by-line calculation utilizing regression coefficients based on various line-by-line models to obtain accurate radiance and atmospheric transmittance (Matricardi et al., 2009).

· LBLRTM (Line-By-Line Radiative Transfer Model)

LBLRTM is an accurate and widely used line-by-line radiative transfer model derived from the fast atmospheric signature code (FASCODE) and developed and maintained by Atmospheric and Environmental Research (AER) Inc. (Clough et al., 1992, 2005). LBLRTM can simulate the spectral radiance spectra from the ultraviolet to the sub-millimeter and is compatible with HITRAN databases of any version. This model has been widely used as the forward model for retrieving atmospheric profiles of temperature and trace gases from high-resolution spectral radiance data. LBLRTM does not account for multiple scattering.

The spectral line profiles of molecules are computed based on the line-by-line calculation through summing of the line shapes of single absorption lines. The spectral line profiles of molecules are characterized by the spectral line center, the intensity, the line width, and the shape. Observed spectral lines are always broad due to the effect of Doppler and pressure (collisional) broadening. Doppler broadening occurs due to the thermal motion of molecules at a given temperature. Pressure broadening is caused by collisions between molecules. The line shape of Doppler broadening follows a Gaussian profile, while pressure broadening can be represented with a Lorentzian profile. The combined effect of the Doppler broadening and the pressure broadening is called the Voigt profile.

Here, we list the representative molecular spectroscopic databases, and note the thermal infrared spectral range of each.

· HITRAN (HIgh-resolution TRANsmission)

HITRAN is a widely used and well-known high-resolution transmission molecular absorption database (Gordon et al., 2017). HITRAN includes several components: (1) line-by-line spectroscopic parameters from the microwave to ultraviolet region of the spectrum ($0.00001 - 25232.0$ cm^{-1}); (2) infrared absorption cross-sections; (3) collision-induced absorption datasets; (4) tables of aerosol refractive indices; and (5) global data that apply to the archive in general. This database is mainly used for terrestrial applications and primarily includes important molecules o in the Earth's atmosphere at temperatures below ~300 K.

· HITEMP (HIgh TEMPerature molecular spectroscopic database)

HITEMP is a molecular spectroscopic database for high-temperature (up to 3000 K) gas absorption and is analogous to the HITRAN database (Rothman et al., 2010). The database includes molecular transitions for five species: H_2O, CO_2, CO, NO, and OH. The structure of the database is almost identical to that of the HITRAN database.

・GEISA (management and study of spectroscopic information)

GEISA was developed by the Atmospheric Radiation Analysis (ARA) group at the Laboratoire de Météorologie Dynamique (LMD) in France (Jacquinet-Husson et al., 1997, 2008). The 2015 edition of the GEISA contains 52 molecular species (118 isotopic species), with transitions in the spectral range of 10^{-6} to 35,877.031 cm^{-1} (Jacquinet-Husson et al., 2016). The GEISA database includes the line transition parameters, infrared and ultraviolet/visible absorption cross-sections, and microphysical and optical properties of atmospheric aerosols. GEISA has been applied to the assessment of the capabilities of the IASI/MetOp mission.

3.2. Calibration method of the thermal infrared spectrometer

In this section, we describe the calibration method of the thermal infrared (TIR) spectrometer. Generally, the calibration of TIR spectra is used for the onboard blackbody and deep space view data. Here, we describe the calibration method used for the recent TIR spectrometers, including AIRS (Atmospheric Infrared Sounder), TES (Tropospheric Emission Spectrometer), and IASI (Infrared Atmospheric Sounding Interferometer).

AIRS is a grating spectrometer onboard the EOS Aqua spacecraft launched in May 2002. The AIRS instrument was designed for a 5-year mission. However, the sensor has been operating for more than 17 years with excellent sensor stability. AIRS is a multi-aperture array grating spectrometer comprised of a temperature-controlled (about 157 K) spectrometer with a two-stage passive radiator and 17 linear arrays of HgCdTe (MCT) detectors cooled by an active-pulse-tube cryogenic cooler. AIRS acquire 2378 spectral channels at resolutions ($\lambda/\Delta\lambda$) ranging from 1086 to 1570 in the spectral range from 3.7 to 15.4 μm. The focal plane assembly (FPA) contains 15 individual photovoltaic (PV)-MCT detectors (3.7 to 13.7 μm) and two photoconductive (PC)-MCT detectors (13.7 to 15.4 μm). The spatial resolution relative to the nadir is about 13.5 km.

Careful prelaunch calibration was conducted, including extensive laboratory testing by the prime contractor of the instruments, BAE System. Prelaunch calibration of the AIRS spectral response functions showed an excellent accuracy of "1% of a width" (Pagano et al., 2003a). Onboard calibration of AIRS utilized a 360-degree rotation scanning mirror and several on-board calibrators. The scanning mirror rotates and acquires the IR data every 2.667 seconds. AIRS obtain an Earth view withing the first 2.017 seconds. The remaining 0.650 seconds is used to acquire views of on-board calibrator (OBC), deep space, blackbody (nominally 308 K), a spectral reference source (Parylene), and the VIS/NIR channel photometric calibrator. (Pagano et al., 2003b).

The scene spectral radiance of AIRS is calculated with the following equation.

$$N_{sc,i,j} = \frac{a_0(\theta_j) + a_{l,i}(dn_{i,j} - dn_{sv,i}) + a_2(dn_{i,j} - dn_{sv,i})^2}{1 + p_r p_t cos2(\theta_j - \delta)}$$

$$(3.2\text{-}1)$$

$$a_0(\theta_j) = P_{sm} p_r p_t [cos2(\theta_j - \delta) + cos2\delta]$$

$$(3.2\text{-}2)$$

The second function of the gain and offset correction, undertaken every scan, is to perform gain correction using the OBC blackbody. The gain is the first order responsivity of the AIRS in terms of radiance units ($mW/m^2/sr/cm^{-1}$) per digital number (dn). We discuss the calibration of the OBC blackbody below.

$$a_{i,j} = \frac{N_{OBC,i}(1 + p_r p_t cos2\delta) - a_0(\theta_{OBC}) + a_2\left(dn_{obc,i} - dn_{sv,i}\right)^2}{(dn_{obc,i} - dn_{sv,i})}$$

(3.2-3)

$N_{sc,i,j}$: Scene radiance of the ith scan and j^{th} footprint [$mW/m^2/sr/cm^{-1}$]

a_o : Radiometric offset, which is nonzero due to polarization

$a_{1,i}$: Radiometric gain. This term converts dn to radiance based on the radiometric gain as determined using the OBC blackbody.

a_2: Nonlinearity correction

θ : Scan angle ($\theta = 0$ is nadir)

$dn_{i,j}$: Raw digital number in the Earth view for the ith scan and j^{th} footprint

$dn_{sv,i}$: Space view counts offset (8 AIRS raw space views)

$p_r p_t$: Polarization product, which is the polarization factor from the scan mirror and the spectrometer

P_{sm} : Planck radiation function evaluated at the temperature of the scan mirror

$N_{OBC,i}$: Radiance of the on-board calibrator [$mW/m^2/sr/cm^{-1}$]

i : Scan index

j : Footprint Index (1 to 90) numbers.

δ : Phase of the polarization of the AIRS spectrometer

The radiometric performance can be discussed based on the following three categories: a) sensitivity b) accuracy and c) stability.

Radiometric sensitivity is defined as the noise equivalent temperature difference (NEdT) at a scene temperature of 250 K. The NEdT for AIRS is measured by interpolating the noise obtained from viewing cold space and the OBC at 308 K. These results showed a negligible difference between pre-launch and in-orbit noise performance. The detector material is affected by radiation in orbit, which is generally caused by radiation hitting the spacecraft as it passes through the South Atlantic Anomaly (SAA). Some of the AIRS channels have degraded during the long-term operation. On the other hand, several channels have been recovered by switching to the redundant detectors (Pagano et al., 2003b).

The accuracy and stability of the Level 1B radiances are evaluated through the comparison

of observed AIRS spectra with radiative transfer model and meteorological datasets, such as the European Center for Medium-Range Weather Forecast (ECMWF) and National Centers for Environmental Prediction (NCEP) (Pagano et al., 2003b). Comparison with a well-calibrated sensor is another effective method for validating the full range of spectra. Tobin et al. (2006) validated the AIRS spectra with the Scanning High-Resolution Interferometer Sounder (S-HIS) over the ocean. They concluded that the resulting brightness temperature differences are less than 0.2 K. Aumann et al. (2006, 2012) calculated sea surface temperature (SST) using the window channels and their monitoring of longwave surface channel stability showed trends of 2 mK/yr.

TES is an infrared Fourier transform spectrometer onboard the EOS-Aura spacecraft, which was launched in August 2004. TES is the first on-orbit interferometer, acquiring high-frequency spectra and retrieving data for a variety of atmospheric gased from space. TES was designed for a 5-year mission but far outlasted that term. A mechanical arm on the interferometer began stalling intermittently in 2010, affecting the instrument's ability to collect data continuously. In January 2018, NASA decided to decommission the instrument after almost 14-years of TES operation.

TES employed a PV-MCT type detector to avoid the PC-MCT detector, which shows a non-linear response. However, the PV-MCT sensor could not cover a wide spectral band, and TES was therefore divided into four focal planes. The frequency ranges of these bands are as follows: 2B1 (650–930 cm^{-1}), 1B2 (920–1160 cm^{-1}), 2A1 (1090–1350 cm^{-1}), and 1A1 (1890–2260 cm^{-1}). Only one filter can be used per scan, but filters can be changed between scans. A single interferometer scan creates 64 interferograms using a 16-detector array in each of the four focal planes. Scan times are 4 seconds for 0.1-cm^{-1} resolution at the nadir and calibration views and 16 seconds for 0.025-cm^{-1} resolution at the limb views. Each individual linear array has a field of view of 0.75 $\times$ 7.5 mrad, corresponding to projections of 0.5 km in the along-track direction and 5 km in the cross-track direction at the Earth's surface projections (Beer et al., 2001).

The TES Level 1B algorithm for processing the spectral radiance data from interferograms consists of the following steps: (1) transformation of interferograms into spectra, (2) radiometric calibration, (3) off-axis ILS correction, (4) spectral calibration and (5) data quality assessment. For details, refer to the "Tropospheric Emission Spectrometer (TES) Level 1B Algorithm Theoretical Basis Document (ATBD)" (Worden et al., 1999).

The technique for performing both phase correction and radiometric calibration, known as "complex calibration", was developed by Revercomb et al. (1998) and is a standard method for calibrating Fourier-transform spectroscopy (FTS) instruments. TES spectral calibration

is conducted using routinely collected reference data from a blackbody at 340 K and a view of cold space.

$$L_{target} = \frac{C_{target} - C_{CS}}{C_{BB} - C_{CS}} \varepsilon_{BB} B(T_{BB})$$

(3.2-4)

L_{target} : Calibrated TES target radiance

C_{target} : Complex target spectrum

C_{CS} : Complex cold space view spectrum

C_{BB} : Complex blackbody spectrum

ε_{BB} : Blackbody emissivity

$B(T_{BB})$: Planck function for ta blackbody at temperature T.

Target data for Earth could not be acquired simultaneously with onboard calibration data. For nominal global survey observations, the period between calibrations was 82 seconds. The operating scenarios were planned so that calibration data were collected before and after target data. Based on prior studies of calibration stability, the temporal linear interpolation algorithm is capable of estimating changes in the instrument's offset radiance. Early in the mission, the optical bench was periodically warmed to remove the buildup of ice on the detector arrays. This is called a decontamination cycles and is used to maintain the alignment of the instrument beam splitter. However, since the signal strength weakened from the end of 2004 to November 2005, the optical bench was warmed by 6 K between 29 November and 2 December 2005. This decision resulted in increased signal levels at the detector, especially at Filter 1A1. Rinsland et al. (2006) showed that the degrees of freedom for signal (DOFS)of CO increased by a factor of 2 (from 0.72 to 1.45 averaged over 30°S–30°N).

Assessing the quality of the TES radiance, Worden et al. (2006) and Shephard et al. (2008) reported the comparisons of TES L1B V002 spectra with those from airborne sensors and other satellites. A comparison of TES with S-HIS over the ocean show differences in means and standard deviation of less than 0.3 K at warmer brightness temperatures of 290–295 K. These differences are less than 0.4 K at brightness temperatures of 265–270 K. TES/AIRS comparisons show mean differences of less than 0.3 K at 290–295 K and of less than 0.5 K at 265–270 K with standard deviations of less than 0.6 K for the majority of spectral regions and brightness temperature ranges. Connor et al. (2011) simulated the window region spectral radiance using the optimal spectral sampling (OSS) radiative transfer model and the real-time global sea surface temperature (RTGSST) data product. This test was performed at 30°N –

30°S over the ocean spanning four years from mid-2005 to mid-2009. The trends of brightness temperature residuals (observations minus calculations) in terms of the standard deviation of the residuals was approximately equal to 0.6 K for the 2B1, 1B2, 2A1 filters, and 0.9 K for filter 1A1. These trends for the TES instrument have been very stable for over four years.

IASI is a Fourier-transform spectrometer payload on the Metop series of European meteorological polar-orbiting satellites; Metop-A, Metop-B, and Metop-C. Its mission objectives are to contribute data to the numerical weather prediction (NWP) and climate monitoring communities. IASI provides atmospheric emission spectra that can be used to derive temperature and humidity profiles and total column amounts of trace gases, such as CO_2, CH_4, O_3, and N_2O. The sounder pixel size at the nadir is 12 km, and the thermal infrared spectral range from 645 to 2760 cm^{-1}, with an apodized spectral resolution of 0.5 cm^{-1}. A 1.54-μm frequency-stabilized laser is used as a reference for sampling the interferogram. In the FTS instrument, the dichroic plates separate the incident IR light into three spectral bands: Band 1 at 645–1190cm^{-1}, Band 2 at 1190–2000 cm^{-1}, and Band 3 at 2000–2760 cm^{-1} (with narrow spectral overlap exists between the bands). The detector types differ: Band 1 uses HgCdTe PC detectors, Band 2 uses HgCdTe PV detectors, and Band 3 uses InSb PV detectors. All detectors are cooled with a passive cryo-cooler. The swath of the scan mirror is ±48.3 degrees perpendicular to the satellite track, with field motion compensation to avoid scene variations during acquisition

The instrument's output should be linear to its input energy. The Band 1 employs the PC-MCT detector, which requires a non-linearity correction step for the interferograms. In the normal operation mode, IASI retrieves 37 measurements including 30 Earth views, 2 space views, 2 blackbody views, and 3 unused measurements during mirror movement. The internal blackbody is used as a hot reference (S_{BB}) with precise temperature (T_{BB}) monitoring, and the space view provides the cold reference (S_{CS}).

$$\tilde{S}(v) = Planck(T_{BB}, v)Re\left[\frac{S(v) - S_{CS}(v)}{S_{BB}(v) - S_{CS}(v)}\right] = Re\left[A(v)\big(S(v) - B(v)\big)\right]$$

(3.2-5)

$\tilde{S}$: Calibrated IASI radiance

v : Wavenumber

S : Complex target spectrum

S_{CS} : Complex cold space view spectrum

S_{BB} : Complex blackbody spectrum

$Planck(T_{BB})$: Planck function for the blackbody at temperature T_{BB}.

Equation (3.2-5) is referred to as the Revercomb et al. (1998) method, which solves the problem of phase correction between the onboard calibration (cold and hot) raw spectra and atmospheric raw spectra through complex calibration. The IASI onboard processing system generates Level 0 calibrated spectra from raw interferograms using non-linearity correction and radiometric calibration (Patrick et al., 2017, Hébert et al., 2017). IASI spectral data are processed on the ground system at the following three levels: level 1A comprises decoding, spectral calibration, radiometric post-calibration, IASI/AVHRR co-registration, location, and dating; level 1B involves resampling the spectra; and level 1C is the application of an apodization function.

Spectral validation of IASI radiances is conducted using the advanced along track scanning radiometer (AATSR), which has a brightness temperature (BT) accuracy of 30 mK. IASI BT agrees with the AATSR BT within 0.3 K, with an uncertainty around 0.1 K and coincident matchup points over the ocean. The agreement is particularly good at 11 μm, where the difference is less than 0.1 K (Illingworth et al., 2009).

Wang et al. (2010) compared AIRS and IASI using the GOES imagers with the double difference method. This technique allows quantification of the radiometric difference between AIRS and IASI radiance values with no effect from GOES imager calibration bias. This comparison was conducted over warm e tropical regions for the 16 months. The results indicated that, at the 95% confidence level, the mean values of the IASI–AIRS BT differences are minimal, with values of -0.0641 ± 0.0074 K, -0.0432 ± 0.0114 K, and -0.0095 ± 0.0151 K for the GOES-11 6.7-, 10.7-, and 12.0-μm channels, respectively, and -0.0490 ± 0.0100 K, -0.0419 ± 0.0224 K, and -0.0884 ± 0.0160 K for the GOES-12 6.5-, 10.7-, and 13.3-μm channels.

4. Thermal infrared band spectra and retrievals from GOSAT/TANSO-FTS

4.1. GOSAT Operation history

GOSAT had achieved 5 years of design lifetime in January 2014 and has now been in operation for more than 11 years. Currently (January 2020), the two main sensors, Thermal and Near-infrared Sensor for Carbon Observation Fourier-transform Spectrometer (TANSO-FTS) and Cloud and Aerosol Imager (TANSO-CAI), are in regular use. Five significant anomalies have been observed by the GOSAT TANSO-FTS during long-term operation. In this chapter, we describe these anomalies.

GOSAT carries a pair of solar array paddles, each of which consist of three solar panels connected by a yoke. The solar array paddle rotation mechanism is a hinged joint that connects the paddle to the satellite body. On 24 May 2014, one of the two solar paddles stopped rotating. The GOSAT onboard computer automatically shut down TANSO-FTS, including the FTS mechanism, detector electronics, and cryocooler. Equipment mounted on the TANSO-FTS optical bench including the telescopes, FTS mechanism, and aft-optics cooled down, and the TIR detector and its optics warmed up. On 30 May 2014, the TANSO-FTS both shortwave infrared (SWIR) and thermal infrared (TIR) band observations restarted.

On 26 January 2015, the TANSO-FTS pointing system was switched from the primary to the secondary (redundant) by rotating the optical path selector by 45° (Figure 2.1-2). TANSO-FTS has a two-axis agile pointing system that allows image motion compensation (IMC) during every 4 s and target observation with a large off-nadir angle. From early September 2014, the settling time of the TANSO-FTS primary pointing system worsened, resulting in the pointing error exceeding 0.1° at the start of interferogram acquisition. The GOSAT operation team tried to adjust pointing control parameters or to cancel target mode observations. However, these efforts did not solve the problem and they decided to switch from the primary to the secondary system. Pointing system settling and stability became much smaller than 0.1°, which was a great improvement over the primary system.

On 2 August 2015, the cryocooler shutdown occurred suddenly as a single event anomaly. The TANSO-FTS pointing system, FTS mechanism, and other electronics continued to function normally. The temperature of the TIR detector increased from the cooling temperature (72.7 K) to ambient temperature (about 295 K), while the SWIR bands operated regularly, providing the normal spectra. On 14 September 2015, the cryocooler restarted

again. During the suspension of the TIR observations, the telescopes and FTS mechanism remained unchanged.

On 17 May 2018, a command and data management system (CDMS) incident occurred, and GOSAT switched to the least load mode (LLM). All the instruments, including the cryocooler and data recorders, were shut down. This situation was similar to the May 2014 anomaly event in that equipment mounted on the TANSO-FTS optical bench was cooled down. GOSAT resumed the observation and communication with the ground stations on 29 May 2018.

On 24 November 2018, a rotation anomaly of the second solar paddle occurred, GOSAT switched to the LLM again, and TANSO-FTS and TANSO-CAI shut down. As the Earth sensor had been switched-off in October 2018, the used of sun acquisition mode (SAM) after the incident influenced the GOSAT orbit. GOSAT returned to the nominal orbit on 18 December 2018, and TANSO-FTS resumed nominal grid observation and calibration observation on 28 December 2018. Target observation started on 31 December 2018.

The cryocooler is a significant heat sources. Following the cryocooler shutdown and restart, the thermal balance was changed suddenly and recovered slowly over time. With a limited number of temperature sensors on board, accurate simulation of instrument temperature distribution requires careful calibration and correction using deep space (DS) data to produce a quality-preserving dataset during cryocooler shutdown accidents.

4.2. TANSO-FTS Level 1B product update

GOSAT TANSO-FTS Level 1A (raw interferogram) and 1B (spectral radiance) dataset are generated by the Japan Aerospace Exploration Agency (JAXA) and transferred to the National Institute for Environmental Studies (NIES).. Since the GOSAT launch, the Level 1 algorithm has been revised several times, with versions numbered as V006, V007, V050, V080, V100, V110, V130, V150, V161, V201, and V210. To date, the latest release version is TANSO-FTS Level 1B V210.210, where the formatting [VAAA.PPP] indicates three-digit algorithm number and parameter version numbers ranging from 000 to 999. The internal test versions of the TANSO-FTS products were processed as V203 and V205 in preparation for V210. TANSO-FTS Level 1B V205 spectra are the same as those of V210. The on-orbit operation and data processing algorithms, including the SWIR bands, have been described by Kuze et al. (2012, 2016). The TANSO-FTS Level 1B product is distributed by the NIES GOSAT Data Archive Service (GDAS).

The TANSO-FTS Level 1B product update and GOSAT operation history are listed in Table 4.2-1. In this table, only major Level 1B algorithm versions with respect to TIR spectra are described. Reprocessing of past data is performed on a moment-to-moment basis.

Table 4.2-1. Thermal and Near-infrared Sensor for Carbon Observation Fourier-transform Spectrometer (TANSO-FTS) Level 1B product update and Greenhouse Gases Observing Satellite (GOSAT) operation history.

FTS L1 ver.	L1 release date	2009	2010	2011	2012	2013	2014	2015	2016	2017	2018	2019	2020
V006	Jan,2009	★ Jan 2009: Launch											
V100	Mar,2010												
V130	Apr,2011												
V150	Apr,2012												
V160	May,2013						★ May 2014: One solar paddle rotation stop ★ Dec 2014: FTS pointing mirror swith(Primary? Seconday)						
V201	Aug,2015												
V210	Mar,2018										★ May 2018: CDMS incident ★ Nov 2018: Solar paddle roration incident		

TANSO-FTS TIR spectral processing has involving the following calibration issues.

a) A mercury–cadmium–telluride photoconductive (PC-MCT) detector was adopted for the TIR band; this detector exhibits a nonlinear response to photon flux.

b) Most of the radiance caught by the TIR detector is derived from the scene flux, although a non-negligible amount of background radiation also arises from the detection system, which consist of the telescopes, pointing mechanism, FTS mechanism, aft-optics, and detector optics.

c) In the TANSO-FTS TIR band, the reflectivity of the pointing mirror is low; therefore polarization sensitivity is slightly high in some TIR spectral regions.

The TANSO-FTS Level 1B TIR spectral calibration issues and update versions are further summarized in Table 4.2-2. The radiometric calibration method or models have been reviewed several times during the past decade. Details of the TIR spectral calibration method are described in the next section.

Table 4.2-2. TANSO-FTS Level 1B thermal infrared (TIR) spectral calibration issues and update versions.

	V006 (First release version)	V100	V130	V161	V201	V210
Detector non-linearity correction	Included	update coefficients	not updated	Included	not updated	update coefficients
Background radiation model	Pre-launch thermal model	not updated	not updated	not updated	not updated	update (consider anomalies*)
Polarization correction	Not included	modeled	not updated	not updated	modify the model	not updated
DS view obscuration	Not included	Not included	Included	Not included	Not included	Not included

*GOSAT anomalies events:

(1) Launch until May 2014: one solar paddle rotation stopped

(2) Until August: 2015 Cryo-cooler shutdown

(3) Until May 2018: CDMS incident

(4) Until November 2018: solar-paddle-rotation incident

(5) Current

4.3. TANSO-FTS TIR band calibration

Figure 4.3-1 shows the TANSO-FTS TIR (Band 4) Level 1 data processing flow. TANSO-FTS has conducted the onboard calibrations using onboard blackbody (BB) and a deep space (DS) data. These onboard calibrations are performed twice during the daytime and four times during the night with a single-orbit period of 98 min. TANSO-FTS TIR observes emissions from the Earth's surface, atmosphere, and cloud, with a wide spectral range (700–1800 cm^{-1}), Thus, the detector and amplifier are both indispensable for a wide dynamic range. The TIR photoconductive detector exhibits a nonlinear response to incident flux (Lachance et al., 1998). Before applying the complex radiometric calibration using BB and DS views as calibration points, all the interferograms must be corrected for nonlinearity, including scene flux, BB, and DS calibration.

In the next section, we describe two critical corrections in detail; non-linearity correction and offset level estimation at the interferogram level, and radiometric and polarimetric correction at the spectrum level.
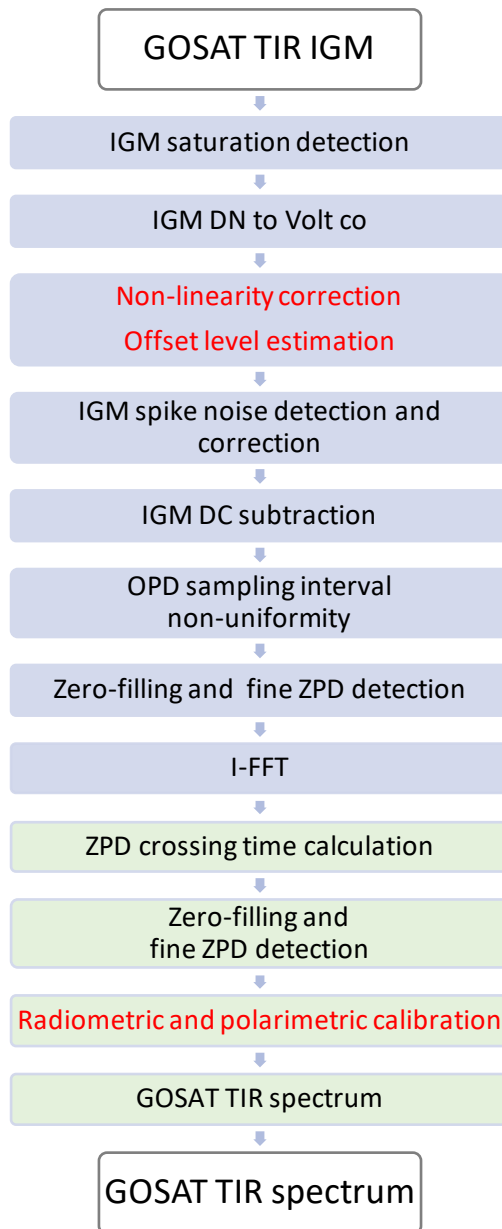
```
┌─────────────────────────────┐
│       GOSAT TIR IGM         │
└─────────────────────────────┘
               ↓
┌─────────────────────────────┐
│   IGM saturation detection  │
└─────────────────────────────┘
               ↓
┌─────────────────────────────┐
│     IGM DN to Volt co       │
└─────────────────────────────┘
               ↓
┌─────────────────────────────┐
│   Non-linearity correction  │
│   Offset level estimation   │
└─────────────────────────────┘
               ↓
┌─────────────────────────────┐
│  IGM spike noise detection  │
│        and correction       │
└─────────────────────────────┘
               ↓
┌─────────────────────────────┐
│      IGM DC subtraction     │
└─────────────────────────────┘
               ↓
┌─────────────────────────────┐
│    OPD sampling interval    │
│        non-uniformity       │
└─────────────────────────────┘
               ↓
┌─────────────────────────────┐
│ Zero-filling and fine ZPD   │
│          detection          │
└─────────────────────────────┘
               ↓
┌─────────────────────────────┐
│            I-FFT            │
└─────────────────────────────┘
               ↓
┌─────────────────────────────┐
│  ZPD crossing time calculation │
└─────────────────────────────┘
               ↓
┌─────────────────────────────┐
│       Zero-filling and      │
│      fine ZPD detection     │
└─────────────────────────────┘
               ↓
┌─────────────────────────────┐
│ Radiometric and polarimetric calibration │
└─────────────────────────────┘
               ↓
┌─────────────────────────────┐
│      GOSAT TIR spectrum     │
└─────────────────────────────┘
               ↓
┌─────────────────────────────┐
│      GOSAT TIR spectrum     │
└─────────────────────────────┘
```

Figure4.3-1. TANSO-FTS TIR (Band 4) Level 1 data processing flow.

4.3.1. Non-linearity correction and offset level estimation

TANSO-FTS Level 1A interferogram DN values are converted to voltage using the gain of the analog-to-digital converter. For the TANSO-FTS TIR Band 4, both the interferogram modulated portion (V_{AC}) and non-modulated portion (V_{DC}) are recorded separately. V_{AC} is the AC-coupled signal, sampled at 38,168 points per interferogram. V_{DC} is the mean DC-coupled signal, sampled at 38 times during the interferogram data collection. The AC and DC components are both used for non-linearity correction of the PC-MCT detector. The non-linearity corrected signal, $V_{NLcorrected}$, is calculated using the original signal and a quadratic non-linearity term as follows:

$$V_{Pamp} = -\left(\frac{V_{DC} - V_{DCoffset}(t)}{g_{DC}}\right) - \frac{V_{AC}}{g_{AC}}$$

(4.3-1)

$$V_{NCcorrected} = V_{Pamp} + a_{nlc}V^2_{Pamp},$$

(4.3-2)

where V_{pamp} is the output of the preamplifier (Figure 4.3-2) and V_{AC} and V_{DC} are observed interferogram data; all others symbols represent correction parameters. $V_{DCoffset}$ is the offset component estimated from the DS view data and prelaunch data; however, its level changes due to detector-amplifier temperature variation. The gain factors of the circuit (g_{DC} and g_{AC}) are fixed at 0.681 and 110.103, respectively. The parameter a_{nlc} is a quadratic non-linearity correction coefficient, which is determined from prelaunch thermal vacuum testing using a well-characterized BB light source at 340 K, which generates a large photon input. When the detector exhibits non-linearity, the most significant signal around at zero path difference (ZPD) is distorted, and a harmonic artifact appears in the low-wavenumber regions of the Fourier-transformed spectra. The quadratic parameter, a_{nlc}, which is assumed to be time-independent, is determined by fitting the combined AC plus DC signal to be flat in the out-of-band regions, i.e., 300–600 cm^{-1} and 2200–3500 cm^{-1}. The parameter a_{nlc} is determined to be 0.6056 V^{-1} for the TANSO-FTS V201 and earlier versions.
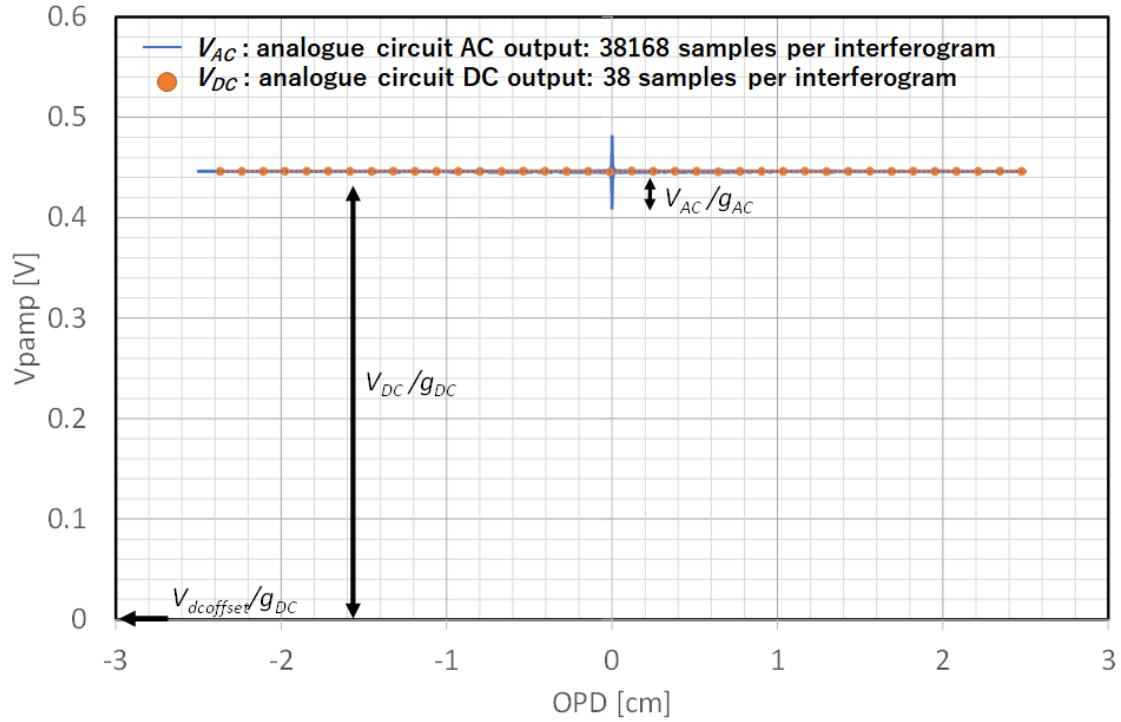
Figure 4.3-2. Output level of the preamplifier, V_{Pamp}, which consists of a modulated portion (V_{AC}), non-modulated portion (V_{DC}), and an offset component ($V_{DCoffset}$). The associated gain factors of the circuit are g_{DC} and g_{AC}, respectively.

$V_{DCoffset}$ is strongly related to the detector amplifier temperature. The $V_{DCoffset}$ model is a function of the time from launch. Because DS radiation can be assumed to be an ideal 3-K BB (cosmic microwave background radiation), DS calibration data yield V_{DC} as the magnitude of background radiation of the environment. Figure 4.3-3 shows that $V_{DCoffset}$ is calculated from the V_{DC} level obtained from the DS view (V_{DC_DSCAL}) and the estimated background radiation from the FTS optics and environment (V_{DC-BG}). The prelaunch value of $V_{DCoffset}$ is expressed as follows:

$$V_{DCoffset}(t_0) = V_{DC_{DSCAL}}(t_0) + V_{DC-BG}(t_0),$$

$$(4.3\text{-}3)$$

where t_0 is the time at prelaunch. The prelaunch thermal vacuum test estimates $V_{DC-DSCAL}(t_0)$ from the linear extrapolation of the prelaunch TANSO-FTS radiometric calibration results using an external cavity BB with temperature set at 260, 280, 300, 320, and 340 K. The value of $V_{DC-BG}(t_0)$ is estimated using the thermal model of the FTS instruments.

On-orbit values of $V_{DCoffset}$ are expressed as follows:

$$V_{DCoffset}(t) = V_{DC_{DSCAL}}(t) + V_{DC-BG}(t),$$

(4.3-4)

where t is the time elapsed from launch. After launch, $V_{DCoffset}(t)$ is estimated from the individual DS view. Assuming that V_{DC-BG} remains unchanged in space, $V_{DC-DSCAL}(t)$ provides the trend of $V_{DCoffset}(t)$ as a function of time elapsed since launch. $V_{DCoffset}$ is strongly dependent on the temperature of the detector-amplifier system and readout electronics. Ground testing of spare electronics after launch revealed that $V_{DCoffset}$ varies by 0.23 V with a change of 1 K in detector temperature.
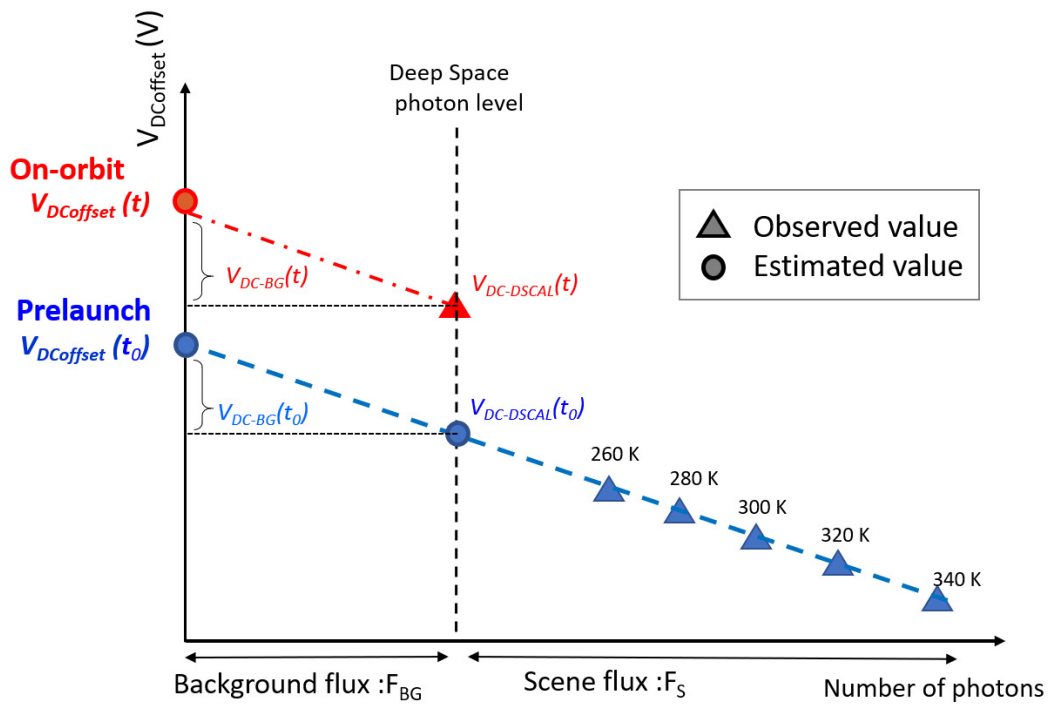
Figure 4.3-3. Schematic of $V_{DCoffset}$ estimation from linear extrapolation of the prelaunch thermal vacuum testing data for TANSO-FTS radiometric calibration using an external cavity blackbody (BB) with temperatures set at 260, 280, 300, 320, and 340 K. Background radiation was estimated from a thermal model of the FTS instruments. After launch, $V_{DCoffset}$ is estimated from the V_{DC} value, from the on-orbit deep space (DS) view ($V_{DC-DSCAL}$) and the estimated background radiation from the FTS optics and environment (V_{DC-BG}).

Figure 4.3-4 shows a schematic view of the TANSO-FTS Band 4 aft-optics including the PC-MCT detector, dewar, and cryocooler subassembly. As mentioned in section 4.1, GOSAT has experienced several significant anomalies that have affected the thermal balance of the TANSO-FTS optics, background, and the detector. These anomalies may also have caused instrument contamination or decontamination issues.

Spacecraft instrument hardware contamination control is important for the success of scientific missions. Contamination is generally divided into two categories: molecular and particulate. Molecular contamination refers to the cumulative buildup of individual molecules of foreign matter, such as outgassing from structural materials, propulsion system plume materials, and ground operation phase residues; molecular contamination related to water vapor is usually the greatest concern. Particulate contamination refers to the deposition of visible conglomerations of matter. Contamination of thermal control surfaces can alter absorbance/emittance ratios and thermal balance, whereas contamination of solar arrays can decrease power output (Tribble et al., 1996).

Ross et al. (2014) reported the performance of the Atmospheric Infrared Sounder (AIRS) and its pulse tube coolers aboard the National Aeronautics and Space Administration (NASA) Earth observation satellite mission Aqua. AIRS is equipped with a hyperspectral IR spectrometer spanning visible to 15.4-μm bands with an MCT focal plane cooled to 58 K using a pair of 55-K pulse tube cryocoolers manufactured by TRW (now Northrop Grumman Aerospace Systems [NGAS]). The optical bench assembly (OBA), which houses the spectrometer optics and supports the focal plane dewar, is passively cooled to ~155 K using a 150-K/190-K two-stage cryogenic radiator. The cryocooler pulse tube housing contains primary and redundant pulse tube coolers above the optical bench. Prior to launch, it was expected that periodic decontamination cycles would be required during the mission to remove accumulated water ice from cold pulse tubes and optical surfaces. After launch, AIRS was subjected to a 36-day decontamination period to allow substantial dissipation of residual water vapor in the surrounding spacecraft structure and multilayer insulation (MLI). After instrument startup, ice accumulation was monitored by tracking the loss of IR transmissivity of the instrument's optics within broad absorption features of water at 4.2 and 10.4 μm; IR transmission losses remained within the acceptable limit of 50%, but the cooler drive rate continued to increase over time. During the summer and autumn of 2002, three deicing cycles were performed on the AIRS instrument. Because frequent decontamination would cause excessive stress to AIRS, the NASA Aqua project decided to implement a dual cooler operational strategy as of November 2002. Although some anomaly events have occurred during long-term operation, the focal plane temperature has continued to show excellent

stability since 2002, and decontamination warmup of the AIRS instrument has not been performed during this period.

Rodriguez et al. (2012) reported the on-orbit performance of the Aura Tropospheric Emission Spectrometer (TES) and its pulse tube cryocooler system. TES is a high-resolution IR imaging FTS with four MCT focal plane arrays in two separate housings cooled to 65 K by a pair of NGAS single-stage pulse tube cryocoolers. The optical bench instrument's two-stage passive cooler maintains the cooling of interferometer and associated optics at ~180 K. The TES instrument was subjected to a 36-day outgassing period after launch. However, moisture remained surrounding the instrument and periodic decontamination cycles were performed every ~2 weeks within the first few months of operation. The level of icing significantly decreased over time; therefore, the interval of decontamination cycles was extended. Detector temperatures increased from 65 to ~230 K during decontamination; however, there was no evidence of detector damage.

Blumstein et al. (2009) reported the instrument status of MetOp-A/IASI. The IASI interferometer and optical bench has regulated at 20°C, while the cold box containing cold optics and detection subsystem is cooled at 91.7 K. On the field lens at the entrance of the cold box, the contamination of water has deposited from the hot parts of the instrument and increase the spectra noise between 700 and 1000 cm^{-1}. The loss of the transmissivity of Band 1 around 850 cm^{-1} reached more than 17 % in March 2008. The maximum acceptable degradation of transmission was to be 20 % and the first decontamination, raised the temperature of cold box to keep at a 300 K in 20 days, performed in March 2008 after 16 months from launch. After the decontamination, all the ice was removed, and the radiometric noise was back to the level measured in December 2006. The occasional decontamination has performed with heating the cold box up to only 200 K.

Crisp et al. (2017) and Na-Nakornpanom et al. (2017) reported the on-orbit performance of the Orbiting Carbon Observatory 2 (OCO-2) instrument. OCO-2 measures reflected sunlight with three wavelength bands: the 0.76-μm O_2A (ABO_2), 1.60-μm weak CO2 (WCO_2), and 2.06-μm strong CO_2 (SCO_2) bands. Presumably because the initial 32-day outgassing period was insufficient for complete water vapor removal from the instrument, a thin layer of ice accumulated on the thermal straps that connect the cryocooler cold head to the focal plane arrays (FPAs). OCO-2 has been periodically decontaminated by warming to near room temperature for a few days to remove ice accumulation, and then re-cooled to operating temperature. A hybrid visible silicon (HyViSI) FPA is used for the ABO_2 band and two MCA FPAs are used for the WCO_2 and SCO_2 bands. The FPA for the ABO_2 band has anti-reflection (AR) coating, conferring a refractive index similar to that of water ice; therefore, its sensitivity is directly affected by the decontamination cycles.

As shown in Figure 4.3-4, the TANSO-FTS detector receives the scene flux and background radiation from the optics and the environment. The detector temperature is thermally controlled by the cryocooler and mechanically isolated from the cryocooler vibration using a thermal coupler system that creates a thermal gradient between the well-temperature controlled cold head and PC-MCT detector. Before the GOSAT launch, the subassembly window was closed, the thermal coupler decontaminated, and the detector maintained under stable and cool conditions. Immediately prior to launch, the subassembly window was opened. The temperature gradient between the cold head and detector is typically about 5 K but may have undergone abrupt changes following cryocooler shutdown or restart in association with GOSAT sensor anomalies. The temperature telemetry resolution of the cryocooler is 0.001 K, whereas that of the PC-MCT detector is 0.7 K. The coarse temperature resolution of the detector makes it difficult to estimate of the temperature gradient, given the limited number of telemetry sensors and the instability of background radiation.
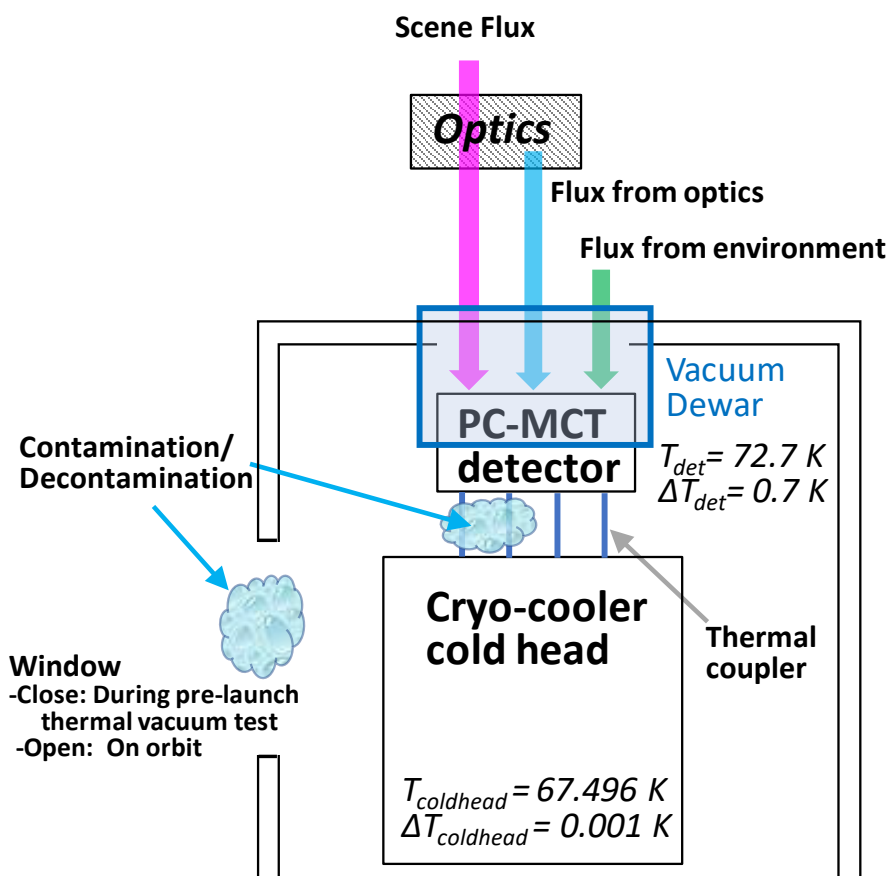

Figure 4.3-4. Schematic layout of TANSO-FTS aft-optics including the photoconductive mercury–cadmium–telluride (PC-MCT) detector, dewar, and cryocooler subassembly. The

detector is thermally conducted with a cryocooler and mechanically isolated from cryocooler vibration by a flexible connector. The thermal gradient between the cold head and detector is temperature-controlled. Rapid changes in the thermal balance of the TANSO-FTS optics, background, and detector may lead to occasional ice contamination or decontamination on the thermal coupler.

4.3.2. Complex radiometric calibration and correction

TANSO-FTS TIR spectral radiometric calibration is performed based on the complex radiometric calibration methods developed by Revercomb et al. (1998) (Figure 4.2-6). This method uses an onboard internal BB as the hot reference and the external DS view as the cold reference. During every orbit, DS and BB calibration are conducted twice during the daytime and four times during the night. Each onboard calibration acquires two sets of forward and backward interferograms. This calibration method thus requires precise monitoring of BB temperature, but it does not require prelaunch calibration and is not affected by on-orbit optical efficiency degradation. The calibration spectral radiances emitted from DS and BB spectra are expressed as follows:

$$B_{obs}(v) = \frac{S_{obs}(v,d) - (S_{DS}(v,d) - \Delta S_{DS}(v,d))}{S_{BB}(v,d) - (S_{DS}(v,d) - \Delta S_{DS}(v,d))} B_{BBeffective}(v) \,,$$

$$(4.3\text{-}5)$$

where $B_{obs}(v)$ is the calibrated spectral radiance and $S_{obs}(v,d)$, $S_{DS}(v,d)$, and $S_{BB}(v,d)$ are the measured spectra of the Earth, DS, and BB views, respectively. $B_{BBeffective}$ is the effective spectral radiance, v is the wavenumbers, and d is the scan direction of the FTS mechanism.
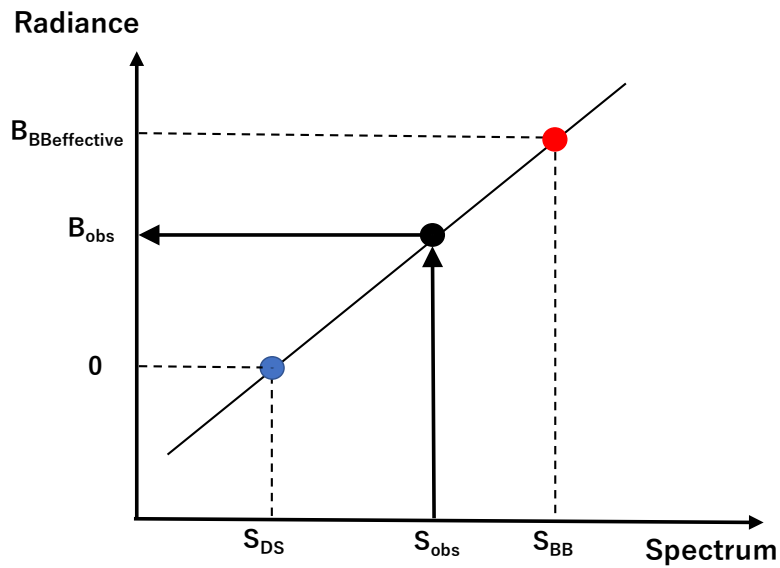

Figure 4.2-6. Schematic of the complex radiometric calibration process.

Form May 2009, the pointing stability of the TANSO-FTS primary system had got worse, perhaps due to the angular resolver bias or insufficient electrical power to properly drive the along-track (AT) motor. Using the onboard camera (CAM), the pointing offset was estimated up to 1°, corresponding to about 10 km on the ground. Due to his pointing instability, the DS view is estimated to have been obstructed by about 3% of the entire scene flux by the inner surface of the DS view hood. The DS view obscuration correction term ΔS_{DS} is expressed as :

$$\Delta S_{DS} = \gamma \frac{B(T_{DShood})}{B(T_{BB})}(S_{BB} - S_{DS}) \,,$$

(4.3-6)

where γ is the obscuration fraction, and T_{DShood} and T_{BB} are the temperatures of the DS view hood and BB, respectively. $B(T)$ is the spectral radiance of the BB at a given temperature T. T_{DShood} is an estimated value of 250 K, and T_{BB} is the BB temperature measured by the three onboard platinum resistance thermometers. This DS view obscuration correction was applied in the processing of the TANSO-FTS Level 1B V130 and V150 product. However, further analysis indicated that the effect of DS view obscuration on longwave spectra was overcorrected, and the correction was removed from V161 processing.

The effective spectral radiance $B_{BBeffective}$ is calculated as follows:

$$B_{BBeffective}(v) = \varepsilon B(T_{BB}) + (1 - \epsilon)B(T_{BG}(t)),$$

(4.3-7)

where ε is the BB emissivity and T_{BG} is the temperature of the environment. The BB emissivity measured before and after launch is shown in Figure 4.2-7. Until the version V150 processing, the emissivity ε was set to 1 in processing. However, to estimate the effective spectral radiance more accurately, consideration of BB emissivity and background temperature was required. From V160 processing, the BB emissivity after launch and background temperature were applied for the Level 1B processing as follows:

$$T_{BG}(t) = T_{AMP} \times sin\left(\frac{2\pi(time_{obs} - time_{asc})}{T_{period}} + Phase_{BG}\right) + T_{BGoffset} \,,$$

(4.3-8)

where T_{AMP} is the amplitude of the background radiation temperature incident on the calibration BB, $time_{obs}, time_{asc}$, and T_{period} are the observation, ascending, and orbital periods, respectively. $Phase_{BG}$ is the phase for T_{BG} estimation and $T_{BGoffset}$ is the temperature offset for T_{BG} estimation.
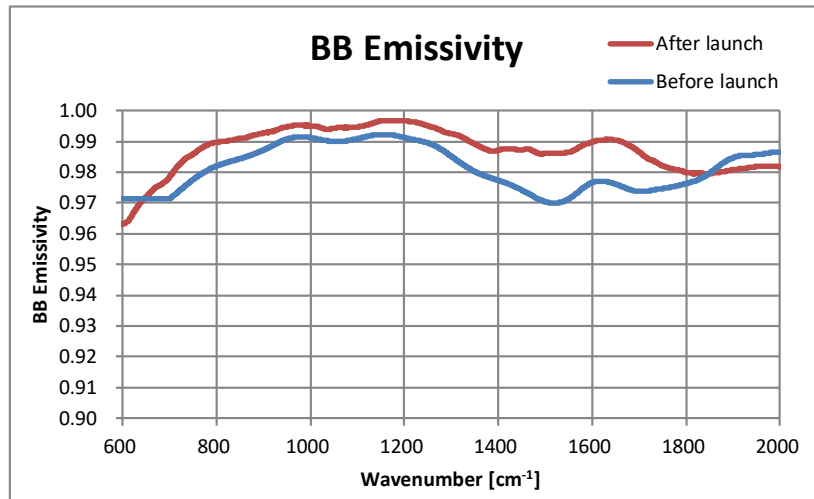

Figure 4.2-7. Blackbody emissivity measured before and after launch.

4.3.3. Polarization correction

The TANSO-FTS pointing mirror facility rotates horizontally by 90° with views toward the DS and BB calibration sources, whereas the Earth scene flux is acquired from the nadir. The silver-coated pointing mirror has been optimized for the SWIR wavelength region with > 99% reflectivity. Reflectivity of the TIR region is lower; however, polarization sensitivity is higher.

The pointing mirror, fold mirror of the FTS mechanism, and FTS aft-optics all exhibit polarization sensitivity in the TIR spectral region. For nadir viewing, polarization effects are corrected using the following relationship relation between $B_{obscorrected}(v)$, $B_{obs}(v)$, and $B_{mirror}(v)$ as follows:

$$
\begin{aligned}
B_{obscorrected}(v) = & \frac{\left((p_2^2 + q_2^2)(p_1^2 + q_1^2) - (p_2^2 - q_2^2)(p_1^2 - q_1^2)\right)}{\left((p_2^2 + q_2^2)(p_1^2 + q_1^2) + (p_2^2 - q_2^2)(p_1^2 - q_1^2)\right)} B_{obs}(v) \\
& + \frac{2(p_2^2 - q_2^2)(p_1^2 - q_1^2)}{\left((p_2^2 + q_2^2)(p_1^2 + q_1^2) + (p_2^2 - q_2^2)(p_1^2 - q_1^2)\right)} B_{mirror}(v) + B_{bg}(v) \,,
\end{aligned}
$$

(4.3-9)

where p_1^2 and q_1^2 are the optical efficiencies of the two linear polarizations of the pointing mirror, and p_2^2 and q_2^2 correspond to the FTS optics and the aft-optics. $B_{mirror}(v)$ is the radiation from the pointing mirror surface, which is estimated from the temperature telemetry data near the pointing mirror. $B_{bg}(v)$ is the difference in background radiation between BB and DS calibrations, estimated from the temperature using the orbit phase variation model. $B_{obscorrected}(v)$ is the final Level 1B TIR product. A more general polarization correction equation using the Mueller matrix is described as follows.

The Mueller matrix is used to correct the along-track(AT) angle (θ_{AT}) and the cross-track (CT) angle (θ_{CT}) dependency of the pointing mirror in slant viewing. Measured spectral radiance is expressed using the scene flux, pointing mirror thermal radiation, and background radiation as follows:.

$$
\begin{aligned}
S_{Toutput} = & M_{opt} M_r(-\theta_{CT}) M_m(\theta_{AT}) M_r(\theta_{CT}) S_{Tinput} \\
& + M_{opt} M_r(-\theta_{CT}) M_e(\theta_{AT}) S_{Tmirror} + \Delta S_{BG} \,,
\end{aligned}
$$

(4.3-10)

where $S_{Toutput}$, S_{Tinput}, S_{mirror}, ΔS_{BG} are the Stokes vectors of the output signal, input

signals, and radiation from the pointing mirror; and ΔS_{BG} is the difference in background radiation between calibrations. M_{opt}, M_r, M_m, and M_e are Mueller matrices of the FTS aft-optics optical efficiency, CT rotation, pointing mirror reflectivity, and pointing mirror emissivity, respectively.

4.4. Greenhouse gases retrieval from TANSO-FTS TIR band

The greenhouse gases (GHGs) retrieval algorithm for TANSO-FTS TIR radiance was developed before its launch. Saitoh et al. (2009) simulated CO_2 retrieval from computed GOSAT pseudo-measurement spectra. Despite possible errors in the atmospheric conditions, they retrieved CO_2 vertical profiles from TANSO-FTS TIR radiance spectra at 700–800 cm^{-1} with an accuracy of 1% at 600–100 hPa in every latitude region.

GOSAT Level 2 TIR CO_2 product version 1 (V1) was created from TANSO-FTS Level 1B V161.160 radiance spectra. The detailed TIR retrieval algorithm was described by Saitoh et al. (2016). In this algorithm, the spectral bias of TANSO-FTS TIR radiance was corrected by simultaneously adjusting the surface emissivity and surface temperature. However, some negative bias of 1.0–1.5 % in CO_2 concentration remains in lower- and mid-troposphere regions, compared with the Comprehensive Observation Network for TRace gases by AIrLiner (CONTRAIL), particularly in summer (Saitoh et al., 2017).

Payan et al. (2017) conducted yearly time-series retrieval of column-averaged CO_2 dry air mole fraction (XCO$_2$) over the Arctic Ocean in summer (July, August, and September) from 2009 to 2015 using several TANSO-FTS Level 1B product versions (V150, V160, V201, and V203). They retrieved XCO$_2$ from the narrow CO_2 band at 940–980 cm^{-1}, which contains the so-called laser band, and surface temperature from the atmospheric window channel. Two anomalies were found in the XCO$_2$ retrievals. First, XCO$_2$ perturbation was observed around the timing of the TANSO-FTS cryocooler shutdown in 2015. The second XCO$_2$ anomaly consisted of differences between V201 and V203 in 2014. In May 2014, the TANSO-FTS sensor shut down, and the background radiation may have changed during this period. Examination of this phenomenon led to the release of the V203 spectra as an internal product, which was considered to be the most reliable version at the time. The XCO$_2$ retrievals showed a reasonable trend of 2.6 ± 0.3 ppmv/year from July 2009 to July 2014 over the Arctic Ocean. Payan et al. (2017) suggested a comparison of TANSO-FTS TIR spectra using IASI temporal coincident and collocated data collected over the ice-free Arctic Ocean, which is a good target for checking radiometric calibration and GOSAT TIR spectral improvement.

Olsen et al. (2017) validated GOSAT Level 2 TIR CH_4 product version 1 (V1) using two satellite-based FTS systems, the Canadian Space Agency (CSA) Atmospheric Chemistry Experiment (ACE) and the ESA Michelson Interferometer for Passive Atmospheric Sounding (MIPAS), as well as one ground-based FTS, the Network for the Detection of Atmospheric Composition Change (NDACC), developed by NASA, the National Oceanic and Atmospheric Administration (NOAA), and the Chemical Manufacturers Association (CMA). For inter-

comparison, all instruments were interpolated into a single pressure grid and smoothed using TANSO-FTS a priori and averaging kernels. TANSO-FTS and NDACC-FTS showed good agreement in the upper troposphere. Below 15 km, the TANSO-FTS profile agreed with ACE-FTS and MIPAS-FTS retrievals to within 4% (± 40 ppbv).

de Lange et al. (2018) retrieved the CH_4 profile from TANSO-FTS Level 1B V161.160 radiance spectra between 1210 and 1310 cm^{-1} using the RemoTeC analysis software. A sensitivity peak was detected at an altitude of around 9 km. Compared with the Monitoring Atmospheric Composition and Climate (MACC) project model field, scaled to total column measurements of the Total Carbon Column Observing Network (TCCON) product, the retrieved CH_4 profile showed about 10% positive bias at peak sensitivity altitudes. To mitigate this bias, a correction scheme was developed using principal component analysis of spectral residuals between observed and calculated values and incorporating knowledge of the state of the atmosphere. The bias of the CH4 profile was thus reduced to < 2%.

An advantage of GOSAT is the simultaneous measurement of both SWIR and TIR spectra for the same footprint. Hence, Kikuchi et al. (2017) attempted to retrieve the partial column density of two layers of the troposphere using the existing SWIR retrieval algorithm by adding TIR windows. However, radiometric calibration uncertainties caused errors in the CO_2 and CH_4 profile retrievals. In the future, reducing biases in TIR radiometric calibration through nonlinearity correction will lead to diminished retrieval error, improving our understanding of local emission and transportation of greenhouse gases.

5. GOSAT TANSO-FTS vicarious calibration with S-HIS

The vertical profiles of atmospheric gases and temperature can be retrieved using the GOSAT TANSO-FTS TIR spectra. The retrieval accuracy of atmospheric gases critically depends on the calibration accuracy of observation radiance spectra. Onboard calibration of the TANSO-FTS TIR spectra has been performed using the complex radiometric calibration using the deep space (cold target) and the onboard blackbody (hot target). The TANSO-FTS measures broad spectral coverage (5.5–14.3 μm) using a single PM-MCT detector. It is difficult to characterize and calibrate the errors of the TANSO-FTS TIR radiance correctly. The spectral comparison with a well-calibrated sensor is an effective means for validation of the nonlinearity correction and onboard calibration in the TANSO-FTS TIR Level 1 processing.

The Scanning High-Resolution Interferometer Sounder (S-HIS) is an important and frequently used validation tool for TIR spectra that controlled by the Space Science and Engineering Center, University of Wisconsin-Madison, Madison (UW SSEC). The S-HIS is a scanning Fourier transform interferometer which measures emitted thermal radiation at a high spectral resolution between 3.3 and 18 μm with laser-controlled sampling. The S-HIS mounted on the NASA high-altitude ER-2 aircraft flew over the TANSO-FTS observed footprint at the time of GOSAT overpasses. The S-HIS FTS covers an almost same spectral range of TANSO-FTS TIR band with a spectral resolution of 0.5 cm^{-1} and IFOV of 100 mrad.

We validated TANSO-FTS TIR radiance with S-HIS radiance using the double difference method. This technique corrects the difference in observation geometry conditions between the TANSO-FTS and the S-HIS using a line-by-line radiative transfer model (LBLRTM).

This work describes the spectral validation of the whole spectral range of TANSO-FTS TIR band with well-calibrated ground-based and airborne FTS sensors. In this chapter, we mainly described the analysis of TANSO-FTS Level 1B V130.130 with the vicarious calibration campaign at Railroad Valley (RRV) in June 2011.

5.1. Summary of GOSAT vicarious calibration campaign in Railroad Valley

The vicarious calibration campaign conducted at the Railroad Valley (RRV) dry desert playa in Nevada, U.S.A. (38.497°N, 115.691°W, elevation 1,437 m) by the joint team of JAXA GOSAT team, NASA Atmospheric CO_2 observations from Space (ACOS) team, and the University of Wisconsin from 19 to 26 June 2011. The vicarious calibration campaign has been performed around the summer solstice every year in collaboration with the ACOS team (current NASA OCO team) since 2009, the year of GOSAT satellite launch (Kuze et al., 2011). The TIR vicarious calibration was to complement a SWIR, however, the coincident validation of the SWIR and TIR bands is a unique aspect of this field campaign.

The RRV field site is a dry lake located in the Great Basin Desert, which is part of the Great Basin between the Sierra Nevada and the Wasatch Range. The filed has a large spatial extent and relatively uniform surface, which is suitable for large footprint sensors. Drying at high altitude also reduces the probability of aerosol, clouds, and surface reflectance variations from changing surface moisture. The surface reflectance is greater than 0.3, which reduce the impact of atmospheric uncertainty. The surface emissivity in this RRV filed is spatially relatively uniform, however, it has a spectral dependence characteristic of a mixture of silicates and halites. The surface temperature in summer daytime could be exceed 320 K or more.

Figure 5.1-1 shows the location of the RRV site and the GOSAT observation paths in the day and night side. During the day, TANSO-FTS pointed toward the RRV site from the GOSAT descending paths 36 (looking from East) and 37 (looking from West) with target observation mode. At night, TANSO-FTS looks from the ascending path 13 (looking from East). The GOSAT overpass time of the RRV site is around 20:44 UT, 21:16 UT, and 7:47 UT from paths 36, 37, and 13, respectively.
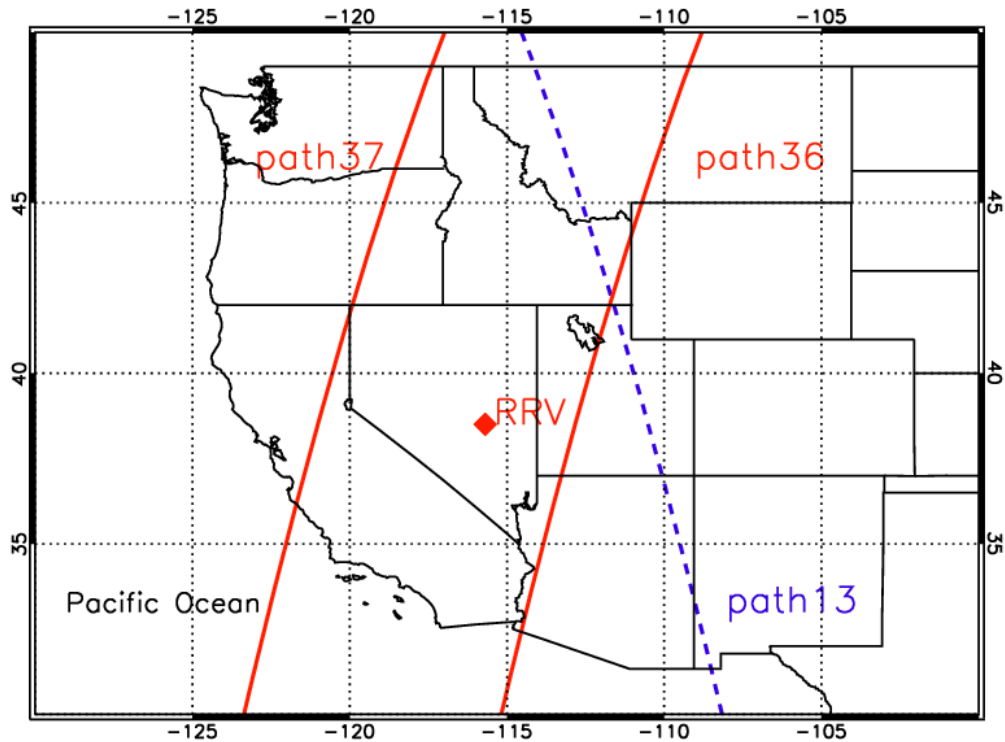
Figure 5.1-1. Location of the vicarious campaign RRV site and the GOSAT observation paths: dayside orbit corresponds with descending paths 36 and 37, and nightside orbit are ascending path 13.

During the campaign, we conducted the field measurement coincident with GOSAT overpasses. The schedule of the campaign and observed parameter are summarized in Table 5.1-1. Figure 5.1-2 illustrates the schematic of observation instruments and measurement items. To obtain the vertical profiles of temperature, relative humidity, and pressure, we launched a Vaisala RS92 radiosonde coincident with the GOSAT overpass, which up to an altitude of about 25 km. We operated the ground-based Surface-Atmospheric Emitted Radiance Interferometer (S-AERI) and measured the upwelling and downwelling radiance at the surface. On 20 June 2011, S-HIS sensor equipped with the NASA ER-2 aircraft flew over the RRV playa and measured upwelling infrared radiance from 20 km altitude. Table 5.1-2 summarizes the specification of TANSO-FTS, S-AERI, and S-HIS, which designs are based upon the Fourie Transform Spectrometer. Since three FTSs operated with difference platforms, the footprint size and spectral resolution are different. Fig. 4.1-3 shows the Instrument Line Shape (ILS) models of TANSO-FTS, S-HIS, and S-AERI. In RRV filed, the meteorological elements (the air temperature, wind speed and direction, relative humidity, and pressure) had been monitored with surface meteorological station managed by JPL. The aerosol properties (aerosol optical thickness, Angstrom exponent) was estimated from the

CIMEL sun-photometer, which is as part of AErosol RObotic NETwork (Holben et al., 1998). Figure 5.1-4 shows the instrument of meteorological station and sun-photometer. Atmospheric CO_2 and CH_4 concentration had measured with two sets of PICARRO instruments, based on Wavelength-Scanned Cavity Ring Down Spectroscopy (WS-CRDS), conducted by NASA/AMES team. One instrument was set up at the base camp to monitor temporal variation near the surface during the campaign. The other was equipped with the NASA/AMES Alpha jet and flew over the RRV playa to measure the vertical profiles of CO_2 and CH_4 coincident with GOSAT overpass. Figure 5.1-5 shows the PICARRO measurements in the ground and the air. These measured datasets were used to implement the input parameters for the radiative transfer calculations.

Table 5.1-1. Summary of schedule and measurement elements in the 2011 RRV campaign.

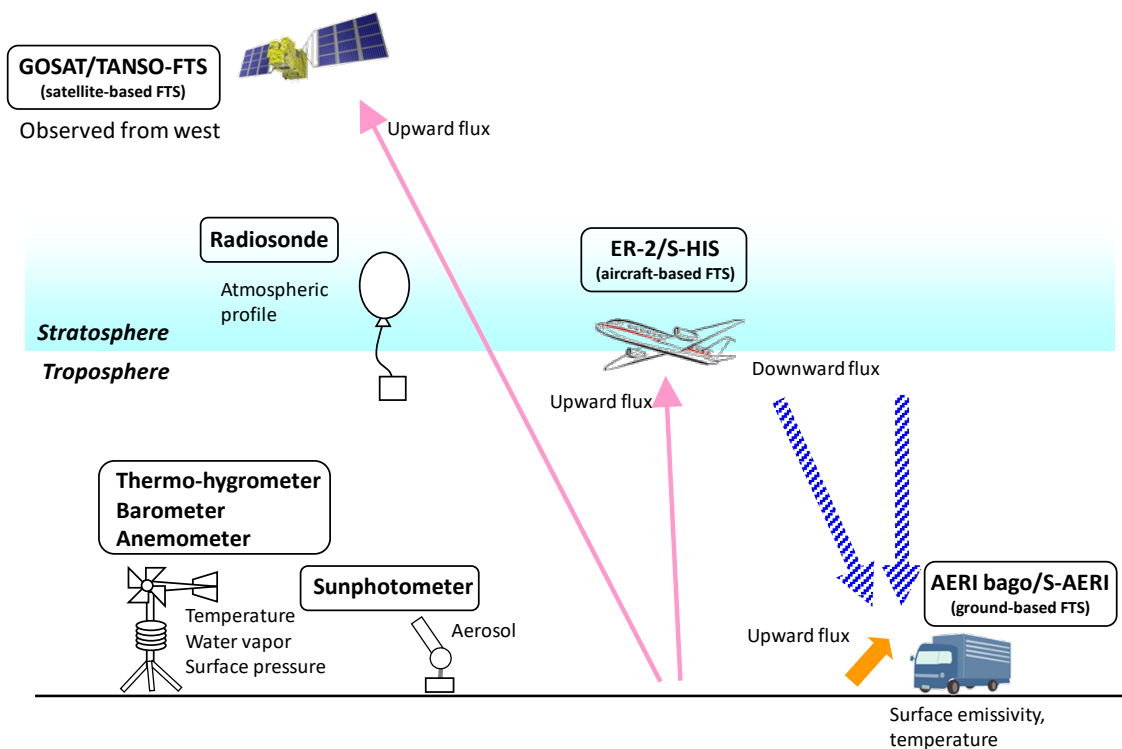| Date	Path	TANSO-FTS	Surface reflectance	Weather station	Radio sonde	AERONET	S-AERI (M_03)	S-HIS	Weather condition
19-June	36	X	M_03, L_09	X	X	—	X	—	Cloudy, Windy
20-June	13	X	—	—	X	—	X	—	Clear
	37	X	M_03, L_08	X	X	X	X	X	Clear
22-June	36	X	L_04	X	X	X	X	—	Small cloud fraction
23-June	13	X	—	—	X	—	X	—	Clear
	37	X	M_03, H_14				X	—	Clear
25-June	36	X	M_03, M_20	X	X	X	X	—	Small cloud fraction
26-June	13	X	—	—	X	—	X	—	Clear
	37	X	M_03, H_21	X	X	X	X	—	Clear

Figure 5.1-2. Schematic view of observation instruments and measurement items in the 2011 RRV campaign.

Table 5.1-2. Radiometric and geometric specification of S-AERI, S-HIS, and TANSO-FTS.

	S-AERI	S-HIS	TANSO-FTS
Spectral coverage	$550 - 3000$ cm^{-1}	$500 - 3000$ cm^{-1}	$700 - 1800$ cm^{-1}
MaxOPD	± 1.037 cm	± 1.037 cm	± 2.5 cm (before truncation)
Spectral resolution	0.48 cm^{-1}	0.48 cm^{-1}	0.2 cm^{-1}
IFOV (FTS, full angle)	46 mrad.	40 mrad.	15.8 mrad.
IFOV telescope	N/A	100 mrad.	N/A
Aperture size	22 mm	45 mm	68 mm
Altitude	5 m (AERI-BAGO) above the local surface	20 km (ER-2 aircraft) above the sea level	666 km (GOSAT spacecraft) above the sea level
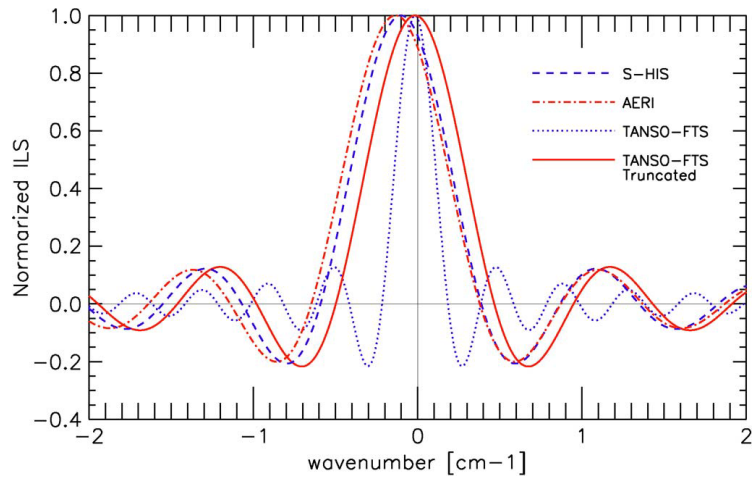
Figure 5.1-3. Normalized ILS models of TANSO-FTS before (dotted) and after truncation (solid), S-HIS (bold), and S-AERI (dash-dotted) at 1000 cm^{-1}. These ILS models are before the finite field of correction. The field of view configuration creates self-apodization that causes an effect on ILS to be broadened and shifted in wavenumber or reduced in amplitude.
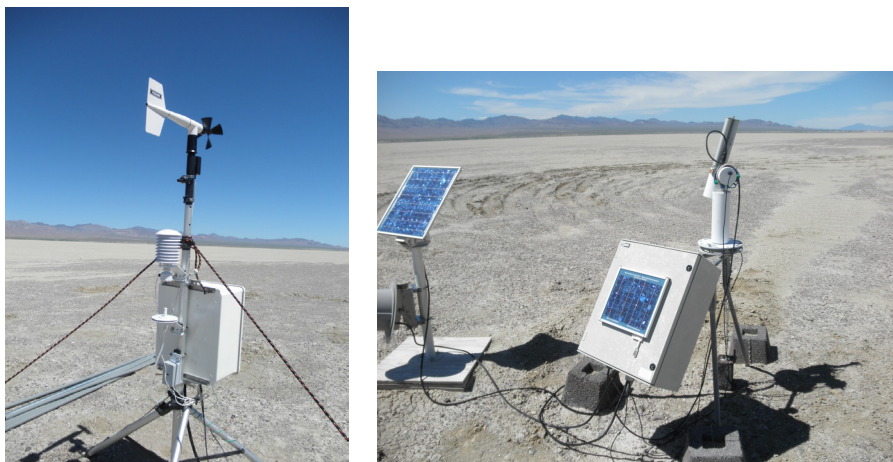

Figure 5.1-4. Pictures of meteorological station and sun-photometer in the RRV field.

Figure 5.1-5. Pictures of PICCARO instrument set up at the base camp and NASA/AMES Alpha jet flew over the RRV playa.

5.1.1. Ground-based S-AERI

The S-AERI is a ground-based passive remote sounding instrument, employing double pendulum FTS, and equipped on the University of Wisconsin research vehicle used in the campaign. S-AERI use two photoconductive HgCdTe and InSb detectors, cooled to cryogenic temperatures, to cover wide thermal infrared spectral ranges. The S-AERI measures the upwelling and downwelling thermal infrared radiation from the atmosphere and surface, respectively. The spectral range is 3.3–18.2 μm (3000–550 cm^{-1}), and IFOV is 46 mrad full angle. The OPD scan speed is 4 cm/s, and the MOPD is $\pm$1.037 cm, which means the spectral resolution is about 0.48 cm^{-1} unapodizd (Knuteson et al., 2004a). The S-AERI instrument was developed for the U.S. Department of Energy Atmospheric Radiation Measurement (ARM) Program by the University of Wisconsin Space Science and Engineering Center. The ARM program uses the AERI instrument to measure the downwelling infrared radiance spectrum to better than 1% absolute accuracy at sites located in diverse climates (Knuteson et al., 2004b). The radiometric accuracy is ensured by regular calibration views of two high-quality blackbodies. The Hot Blackbody (HBB) is temperature-controlled to 333 K, and the Ambient Blackbody (ABB) passively follows ambient temperature. Onboard reference blackbodies are viewed as part of each cross-track scan, providing updated calibration information every 20-30 seconds. The absolute radiometric uncertainties are less than 0.1 K (3 σ) at near ambient air temperature.

Figure 5.1-6 shows the S-AERI research vehicle and S-AERI instrument. During the campaign, the vehicle parked near theM_03 site (38.484°N, -115.685°W), which is close to the center of the playa. The S-AERI was operated at the time of GOSAT day and night overpasses. The downwelling radiance emitted from atmospheric was observed with two viewing angles (zenith and the sky view at 60° from zenith). The upwelling radiance emitted from surface obtained at three viewing angles (30, 45, and 60°) from nadir. The measured upwelling radiance is used to retrieve surface temperature and emissivity. The S-AERI upwelling radiance measurement conducted at two additional sites to check the spatial variation of emissivity within the playa. The detail retrieval algorithm for estimating the surface temperature and emissivity is described in Antonelli et al. (2004) and Knuteson et al. (2004c). The downwelling radiance is also used to confirm the atmospheric temperature, CO_2, and O_3 profiles used in the radiative transfer calculations.

Figure 5.1-6. S-AERI research vehicle and S-AERI instrument side view.

5.1.2. Aircraft-based S-HIS

The S-HIS is a cross-track scanning airborne FTS is approximately the same configuration of S-AERI. S-HIS is designed to validate the spectral radiance of satellite sensors and provide retrievals of atmospheric and surface properties. The full angle of the entrance beam is 100 mrad, which is equivalent to about 2 km diameter nadir footprint at the ER-2 altitude of 20 km. In each cross-track scan sequence, the scene mirror is rotated and obtain 13 distinct Earth views, followed by five Hot blackbody views and five Ambient blackbody views used for calibration. The spectrally random noise on the S-HIS radiance was reduced using the PCA noise filtering algorithm described in Antonelli et al. (2004). The S-HIS has absolute radiometric uncertainties of less than 0.15 K (3σ) for scene brightness temperatures higher than 250 K.

On 20 June 2011, the NASA ER-2 aircraft took off from the NASA Dryden aircraft operations facility and flew over California and Nevada. The ER-2 carried the S-HIS, the Airborne Visible/Infrared Imaging Spectrometer, and the MODIS/Advanced Spaceborne Thermal Emission and Reflection Radiometer (ASTER) Airborne Simulator (MASTER). Figure 5.1-7 shows the ER-2 flight course, the aircraft height, and outside air temperature. The ER-2 flew over the RRV at about 20 km height and took three passes approximately from 21:00 UT to 21:30 UT. There was no visible cloud in the field of view of the TANSO-FTS conformed with the GOSAT CMOS camera image.

The surface temperature over the RRV playa is not spatially uniform and it varies with time. The radiation from the surface is more dominant than atmospheric radiation in the TIR window channels. An accurate and spatial-temporal coincident surface information is critical for the vicarious calibration of the TIR band. According to a meteorological ground station data, the air temperature during the ER-2 flight over the RRV playa (about 30 min) varied between 1 and 2 K. Therefore, for this analysis, we selected the ER-2 overpass which was coincident in time with the GOSAT observation. The cross-calibration with the airborne sensor commonly conducted over the ocean because of spatial-temporal stability. However, the cross-calibration over this land site is possible because the cross-track S-HIS observations covered the spatial extent of the GOSAT footprint with higher spatial resolution and performed at the precise time of the satellite overpass.
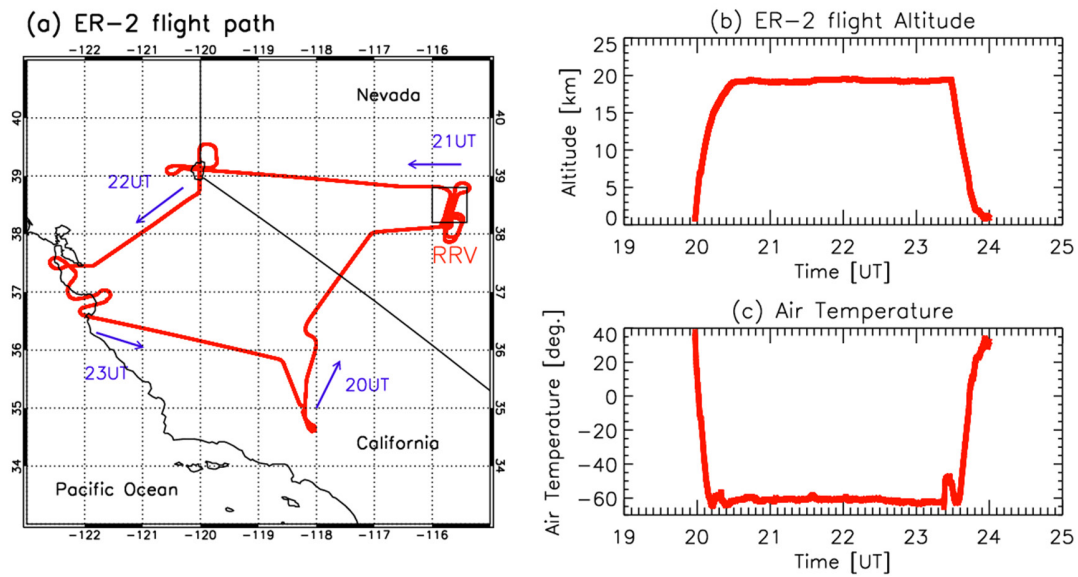
Figure 5.1-7. (a) NASA/AMES ER-2 aircraft flight paths on 20 June 2011. (b) The time series plot of the ER-2 aircraft flight altitude. (c) The time series plot of the air temperature outside ER-2 aircraft.

The previous work of the radiometric validation using S-HIS has conducted with the NASA Atmospheric Infrared Sounder (AIRS) sensor on the EOS Aqua satellite and NASA Tropospheric Emission Spectrometer (TES) sensor on the EOS Aura satellite over the Gulf of Mexico. Tobin et al. (2006) confirmed that AIRS radiometric accuracies are better than 0.2 K for most channels. Shephard et al. (2008) indicated that TES comparison with S-HIS show means and standard deviation differences of less than 0.3 K at brightness temperatures 290 to 295 K and less than 0.4 K at brightness temperatures of 265 to 270 K. These NASA's thermal infrared sensors radiance comparisons with the S-HIS conducted over the ocean. In this paper, we compared the spectral radiance of TANSO-FTS with S-HIS over a land site that had a much higher scene temperature (over 320 K) than is possible over the ocean. This attempt provides a test of the TIR window channels calibration at scene temperatures that are difficult to achieve using inter-calibration with other satellites.

Both TANSO-FTS and S-HIS instruments have operated on the same principle at the same time but at different observational geometries. In order to account for the different slant angle views through the atmosphere, we perform a radiative transfer calculation for each sensor independently while using the same atmosphere profiles as input. A comparison of the two observation minus calculation residuals is known as a "double difference" method, which has proven to be highly effective for this type of radiometric calibration (Tobin et al., 2006).

5.2. Method of forward calculation

5.2.1. Observation geometry

The GOSAT satellite is placed in 666 km altitude sun-synchronous orbit of 13:00 local time with an inclination of 98º. Figure 5.1-2 and Table 5.1-2 summarized the observation geometry of TANSO-FTS and S-HIS. TANSO-FTS observed the RRV playa three times changing the pointing angle with target observation mode. Coincident with GOSAT overpass, S-HIS flew over the RRV playa at an altitude of about 20 km and obtained the thermal infrared radiance with a scan angle approximately $\pm36°$. In this work, we utilized the line-by-line radiative transfer model (LBLRTM) forward calculations to compensate for the difference in sensor observation geometries (Clough et al., 2005). The input parameters and data sources used in the forward calculation are summarized in Table 5.2-2.

Table 5.2-1. Observation information of the TANSO-FTS and S-HIS on 20 June 2011.

	TANSO-FTS			S-HIS
	RRV1	RRV2	RRV3	Center path
Number of exposures	1	1	1	36
Time	21:19:46	21:19:51	21:19:55	21:18:45 – 21:19:40
AT angle [deg.]	-2.45	-4.66	-6.86	-26.5 – 13.5
CT angle [deg.]	32.92	32.90	32.88	

Table 5.2-2. Input parameters and their source for the forward calculations.

	Sources	Remarks
Surface emissivity	S-AERI ASTER	Extrapolated with MODIS emissivity model
Surface temperature	S-AERI APGEE radiometer (spatial distribution within 500m×500m) S-HIS (spatial distribution within TANSO-FTS IFOV)	S-HIS covered the entire TANSO-FTS IFOV
Temperature and humidity vertical profile	Below 30 hPa: radiosonde $10-30$ hPa : GPV/JMA Above 10 hPa : U.S. standard	
O_3 vertical profile	University of Bremen climatology model	Modified for S-HIS spectra
CO_2 vertical profile	390 ppm constant	
Other gases	U.S. standard	

5.2.2. Pressure level grids

The setting of pressure level grids in forward calculation referred to the TES Level 2, which are linearly interpolated in a log pressure scale. The detail of the setting described in the TES Level 2 Algorithm Theoretical Basis Document (1998). Especially in the lower troposphere (below 400 hPa), we set a finer pressure level grid because the vertical profile near the surface is strongly affected by the desert surface temperature. In this work, we set the pressure level grids at 5 hPa intervals below 800 hPa and 10 hPa intervals between 800 and 400 hPa. The setting of forward calculation pressure levels described in Table 5.2-3.

Table 5.2-3. The setting of the pressure grid for the forward calculations.

Pressure range	Pressure grid
Surface pressure	
Below 800 hPa	$\Delta P = 5$ hPa
800 – 400 hPa	$\Delta P = 10$ hPa
383.118 – 1.0 hPa	$Pk = 1000 \times 10^{-(k-2)/24}$
0.825 – 0.1 hPa	$Pk = 1000 \times 10^{-(k-38)/12}$
0.068 – 0.01 hPa	$Pk = 1000 \times 10^{-(k-62)/6}$
0.004 – 0.001 hPa	$Pk = 1000 \times 10^{-(k-77)/3}$

5.2.3. Atmospheric condition

Figure 5.2-1 shows the atmospheric profiles of air temperature, water vapor (H_2O), and O_3. On 20 June, 2011. The vertical profile of air temperature and H_2O obtained from VAISALA RS92 radiosonde launched coincident in time with the GOSAT overpass from the RRV base camp. The weather balloon profile reached about 25 km altitude above the flight level of the NASA ER-2. To extend the temperature and H_2O profiles from the top altitude of the radiosonde to 10 hPa, we used the Grid Point Value (GPV)/Japan Meteorological Agency (JMA) analysis fields interpolated to the GOSAT overpass time at RRV. As for the O_3 profile, we did not have synchronized observation data, both field and satellite measurement at the time of GOSAT overpass. Instead, we selected a profile from the global climatology of ozone database, which was made by the University of Bremen, adjusted to match the S-HIS radiance (Lamsal et al. 2004). At an altitude above the GPV profile (above the height of 10 hPa) and for the other minor gases, we used the LBLRTM built-in model (U.S. Standard 1976). Input profile data for the forward calculation interpolated to the pressure level grid. Since there was no in-site CO_2 vertical profile measurement with the airborne PICARRO (Yates et al., 2011), we assumed a vertically uniform distribution of column-averaged dry-air mole fractions of 390 ppm retrieved from the TANSO-FTS SWIR band by the ACOS Level 2 algorithm. The retrieval error of ACOS CO_2 product is smaller than 3 ppm. The day-to-day variation of in situ measurement and GOSAT data is also smaller than 3 ppm. In order to verify the atmospheric profile setting for the forward calculations, we calculated downwelling radiance and compared with the observed S-AERI downwelling radiance. The radiance comparison between observations and calculations shows good agreement in all bands.
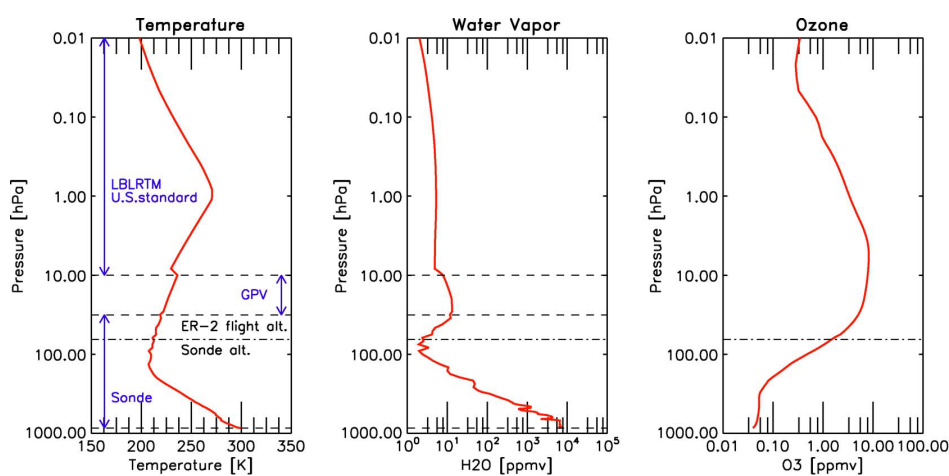

Figure 5.2-1. Vertical profiles of temperature, water vapor, and ozone input for the forward calculations.

5.2.4. Surface condition

ASTER on the EOS Terra satellite overflew the RRV playa on 26 June 2011, 18:38 UT. ASTER has five TIR bands with 90 m spatial resolution, and it is useful to confirm the spatial variation of emissivity and surface temperature (Hook et al., 2005, 2007). Figure 5.2-2 shows the map and the histograms of kinetic temperature and emissivity within TANSO-FTS footprints. ASTER data show the surface emissivity is spatially uniform, but the surface temperature has spatial variability over the playa. However, the ASTER spectral broadband data does not provide the high spectral resolution of emissivity, which need for the input to the forward calculation of high spectral radiance of the TANSO-FTS and S-HIS. In this study, the coincident surface temperature and surface emissivity of the RRV playa retrieved from the ground-based S-AERI upwelling and downwelling radiance observations. University of Wisconsin-Madison team measured the S-AERI infrared radiance at the RRV M_03 site during the nighttime (07:47 UT) and daytime (21:19 UT) GOSAT overpass. We adopted the nighttime spectra for retrieving the surface emissivity. Because it is more stable than daytime spectra and nearly-unchanged in a short time and downward flux from the atmosphere is small.
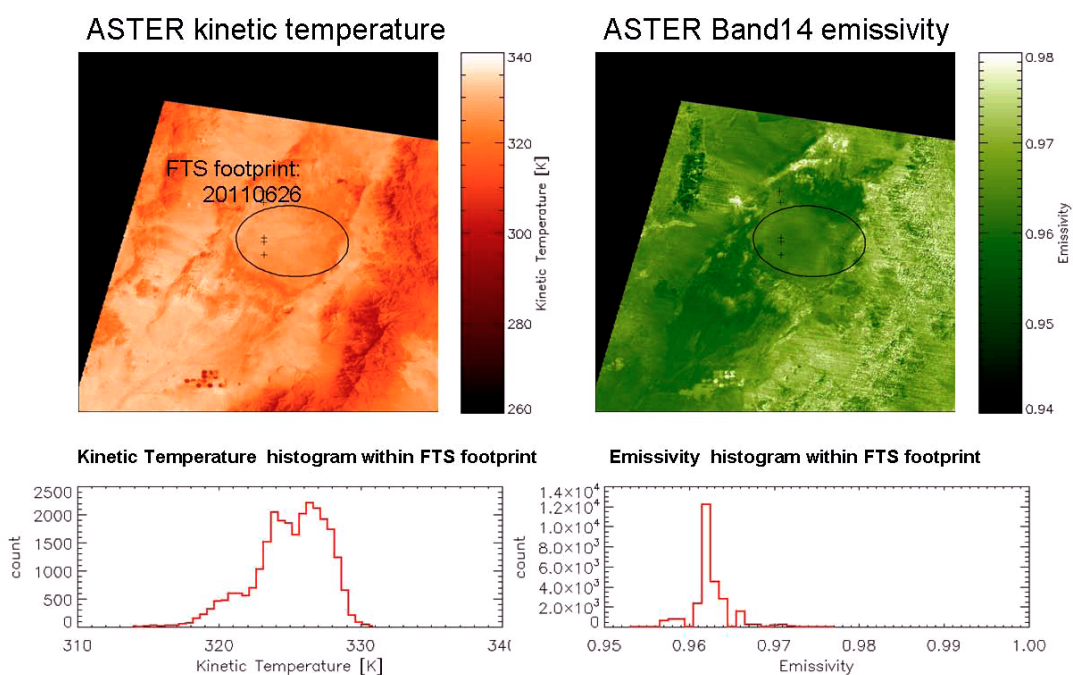

Figure 5.2-2. Upper images show the spatial distribution of kinetic temperature and emissivity in the RRV playa from ASTER TIR data on 26 June 2011. The circle means the TANSO-FTS footprints on 26 June 2011. The below plots are the histograms of kinetic temperature and emissivity within TANSO-FTS footprints, respectively.

The upwelling Earth view radiance obtained by S-AERI is expressed as follows:

$$R_{obs} = \varepsilon(\phi, \nu)B(T_s) - (1 - \varepsilon(\phi, \nu))N_{dn}$$

$$\varepsilon(\phi, \nu) = \frac{R_{obs} - N_{dn}}{B(T_s) - N_{dn}},$$

(5.2-1)

where R_{obs}, N_{dn}, and $B(T_s)$ are the upwelling Earth view radiance observed at 30, 45, and 60° from nadir, the downwelling hemispheric flux, and the Planck function at the surface temperature, respectively (Knuteson et al., 2004a). The surface emissivity $\varepsilon(\theta, \nu)$ with emission angle ϕ of and wavenumber of ν in (5.2-1) and temperature can be retrieved simultaneously in such a way that the difference between online and offline spectral radiance at 909 cm^{-1} is minimized. The retrieved emissivity spectrally smoothed without atmospheric emission and absorption. The S-AERI downwelling atmospheric radiance at 60° from the zenith view was used as an approximation for the downwelling hemispheric flux under the cloud-free conditions at RRV. The moving average filter was applied to reduce the noise present in the derived S-AERI spectral emissivity. For the spectral range outside the region of 750–1250 cm^{-1} where the S-AERI direct measurement is most accurate, we applied the laboratory measurements of RRV surface spectral emissivity with the MODIS UCSB Emissivity Library developed by the MODIS LST group at the University of California, Santa Barbara (UCSB) (Wan et al., 1997). Figure 5.2-3 shows the RRV spectral surface emissivity used for the 20 June 2011 analysis. The surface of the RRV playa is estimated to consist of a mixture of quartz mineral and halite salts (Baldridge et al., 2009). ASTER data indicate that RRV playa emissivity is spatially homogeneous and S-AERI data can be applied throughout the TANSO-FTS footprint.
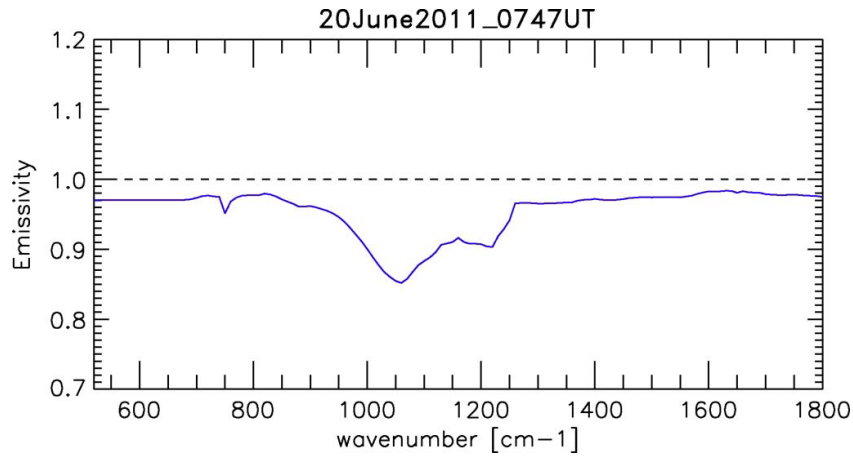

Figure 5.2-3. Spectral emissivity of RRV playa retrieved from the ground-based S-AERI

upwelling and downwelling nighttime radiance measured at M_03 site on 20 June 07:47UT. For the spectral range outside the region of 750–1250 cm⁻¹, we applied the laboratory measurements of RRV surface spectral emissivity found in the MODIS UCSB Emissivity Library.

The accurate estimation of the surface temperature within TANSO-FTS IFOV is essential to evaluate the thermal spectral radiance of the TANSO-FTS. Therefore, we utilized the S-HIS spectral radiance within the TANSO-FTS IFOV and S-AERI measurement at the time of the daytime GOSAT overpass at the M_03 site. The surface temperature of each S-HIS FOV estimated from the S-AERI measured surface skin temperature scaled by the ratio of the S-HIS radiance in a window region (867–870 cm⁻¹) as follows:

$$T_{S_{SHIS\_scan}}(i) = \frac{R_{SHIS\_scan}(i)/\tau_{SHIS\_scan}(i)}{R_{M\_03}/\tau_{M\_03}} \times T_{S_{M\_03}},$$

(5.2-2)

where $T_{S_{SHIS\_scan}}$ is the surface temperature of each S-HIS scan, i is the scan number of S-HIS, R_{SHIS_scan} is the S-HIS averaged radiance in window region at each S-HIS scan, R_{M_03} is same as at M_03 site, τ_{SHIS_scan} is the transmittance at each S-HIS scan, and τ_{M_03} is the same as at M_03 site, and , $T_{S_{M\_03}}$ is the S-AERI measured surface temperature at M_03 site. In order to cancel out the observation angular dependence of the atmosphere, we took account of the transmittance for each S-HIS FOVs. Figure 5.2-4 shows the surface temperature of each S-HIS FOVs within the TANSO-FTS footprint overlaid on theTANSO-CAI Band 3 image. During the GOSAT overpass, we measured the local surface temperature spatial variation using an APOGEE radiometer, consist of a thermopile detector, germanium filter, and precision thermistor, within a 500 m² × 500 m² area at M_03 and other observation sites. These data show a 2 K peak-to-peak spatial temperature variation, which supports the importance of using the S-HIS observations to obtain a weighted surface temperature for the TANSO-FTS footprint. Since the TANSO-FTS IFOV is relatively large (10.5 km at nadir), the surface temperature of TANSO-FTS is given by the average of the S-HIS surface temperature over the entire TANSO-FTS footprint as follows:

$$T_{S_{FTS\_IFOV}} = \sum_j T_{S_{SHIS\_scan}}(j)/N_j,$$

(5.2-3)

where j and N_j is the number of S-HIS scans and total S-HIS scans within TANSO-FTS IFOV, $T_{S_{SHIS\_IFOV}}$ is the averaged surface temperature within TANSO-FTS_IFOV. The estimated surface temperature within the TANSO-FTS IFOV for the daytime 20 June overpass is 322.9 K.
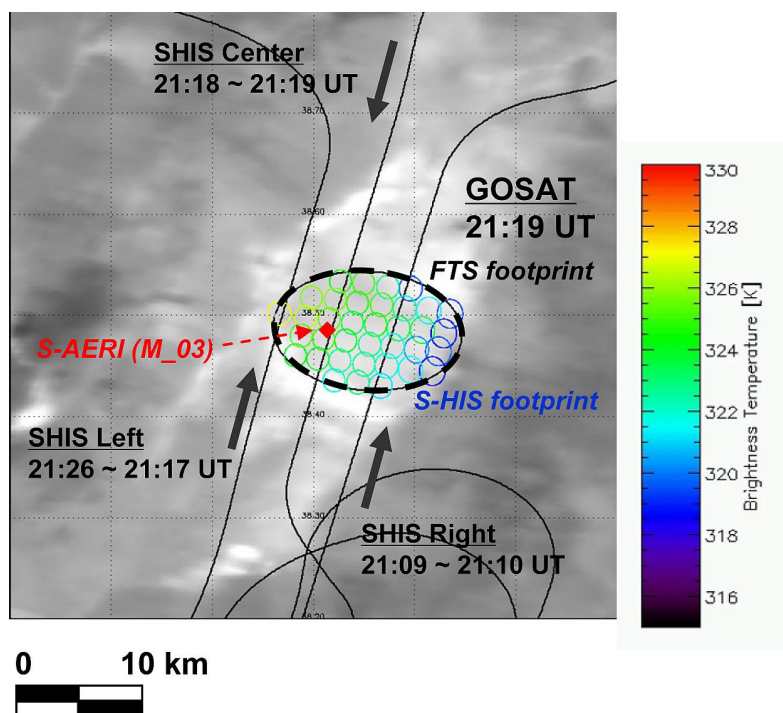

Figure 5.2-4. Colored S-HIS FOV circles are the surface temperature retrieved from the S-AERI and the S-HIS radiance. The background grayscale image is TANSO-CAI Band 3 on 20 June 2011. Bold dotted line means the TANSO-FTS footprint estimated by CMOS camera image and solid lines are the ER-2 aircraft flight paths. The rhomboid shows the location of the S-AERI measurement.

5.3. Method of spectral comparison

The TANSO-FTS measured the thermal infrared radiance three times over the RRV playa during the 20 June 2011 daytime overpass. The left panels in Figure 5.3-1 show the three exposures of observed TANSO-FTS spectra (#1 ~#3). In this work, we evaluated the TANSO-FTS Level 1B V130.130 spectra. The right panel shows the observed brightness temperature differences relative to the second exposure. Three spectra are close to the same, but CO_2 channels, especially in less than 700 cm^{-1} and O_3 channels, slightly varies with slant viewing geometry. In this work, we compared the three TANSO-FTS spectra with S-HIS center path spectra synchronized with GOSAT overpass.

In order to carefully compare the observed spectra with each other or with calculated spectra, some spectral manipulation of FTS data is required. In comparing the spectra between different sensors, the spectral resolution matching is important. The truncation of the interferogram can produce FTS spectra with any spectral resolution lower than the MOPD. Before the truncation operation, some correction, the effect of self-apodization and wavenumber shift, is required for measured spectra. The spectra manipulation of FTS data summarizes in this section.
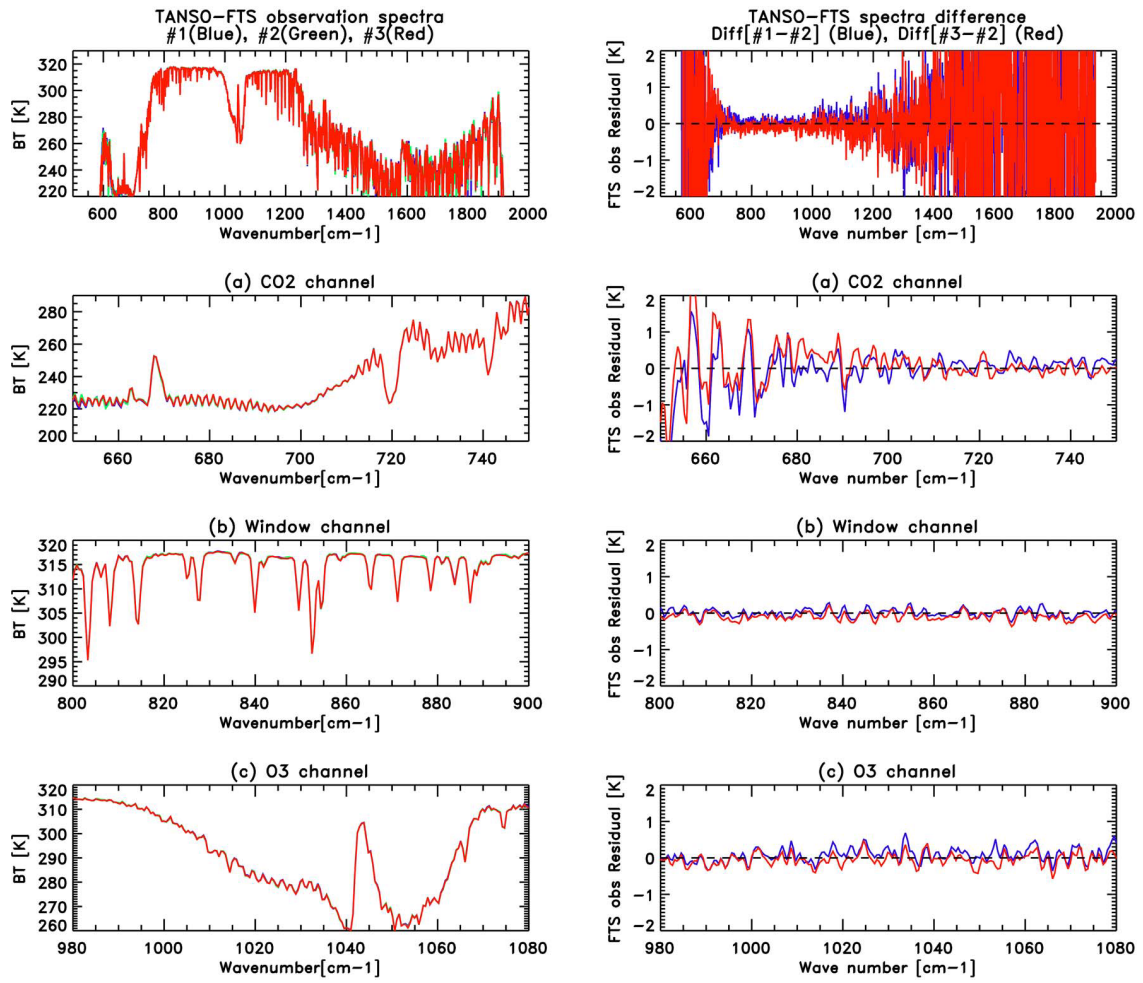
Figure. 5.3-1. Left panel shows three exposures of observed TANSO-FTS spectra (#1 ~#3) over the RRV playa. The right panel shows observed brightness temperature differences relative to the second exposure (#2).

An ideal FTS with an on-axis small-sized detector has a pure SINC function ILS without any self-apodization. In order to detect enough photons to achieve high SNR with limited exposure time, an FTS for remote sensing applications has a finite field of view. The finite size of the detector creates self-apodization due to maximal OPD. The self-apodization of the interferogram results in an ILS that is broadened in wavenumber and reduced in amplitude. Besides, the FTS ILS appears to be shifted in wavenumber. In this work, we corrected the FTS self-apodization of the TANSO-FTS to create wavenumber independent spectral resolution (finite field of view correction). The corrected spectra have an ideal SINC function ILS without a wavenumber shift. The S-HIS spectra are also corrected for self apodization in this manner.

The optical alignment of the sampling laser on TANSO-FTS has possibly changed since launch. The observed wavenumber scale of the TANSO-FTS has gradually changed with time. In this work, we evaluated the wavenumber shift from the comparison between observed and calculated spectra at CO_2 absorption band (730–740 cm^{-1}). The wavenumber shift evaluation required a finer spectral grid, less than an observation sampling grid. The observed and calculated spectra have applied zero-filling processing, which means the additional zero-valued points to end of the observed and calculated interferogram. The observed spectrum wavenumber is shifted to fit calculated spectrum wavenumber as follows:

$$\sigma' = \sigma(1 + \varepsilon),$$

(5.3-1)

where σ is original wavenumber, σ' is shifted wavenumber, and ε is the evaluated wavenumber shift ratio.

To describe a signal with a discontinuity time-domain requires infinite frequency content. However, it is not possible to sample infinite frequency content. The truncation of frequency content causes a time-domain "ringing artifact" on the signal, which is called the "Gibbs phenomenon." The Fourier Transform of either an observed or calculated spectrum which has been inserted into a wavenumber array starting at zero wavenumber with "band guards" or "roll-off" (cosine) functions applied on both ends of the radiance spectrum to minimize the "Gibbs phenomenon." The corrected interferogram is truncated by the desired MOPD (Max OPD). The Max OPD for TANSO-FTS is set to be 2.5 cm OPD, S-HIS is 1.037 cm OPD, and S-AERI is 1.037 cm OPD. After truncation, the inverse Fourier Transform processing is applied to produce spectra at the spectral resolution of each sensor.

The purpose of this study is to intercompare the high spectral radiance of TANSO-FTS with other measurements with lower resolution. For this reason, removing small truncation artifacts with a mathematical apodization does not affect the calibration accuracy. In order to remove the "ringing artifacts" (Gibbs phenomenon) on the signal, an apodization applied the interferograms for observation and calculation, respectively. We applied the following Gaussian module:

$$g(x) = \exp\left(\frac{-x^2}{\sigma^2}\right),$$

(5.3-2)

where x is the optical path difference, and σ is full width half maximum (FWHM). In this work, we applied the Gaussian filter with FWHM = 0.6 in the interferogram domain.

5.4. Comparison of TANSO-FTS and S-HIS

5.4.1. Double difference methodology

The thermal infrared radiance of TANSO-FTS and S-HIS observed with different viewing angles, observation altitudes, and footprint sizes. The spectral characteristics of each sensor are also different. In order to account for these differences, we adopted the double difference method proposed by Tobin et al. (2006). This technique is to compare the residuals between observed and calculated spectra radiances for each instrument using LBLRTM forward calculations. The double difference R_{diff} is defined as follows:

$$R_{diff} = \left(\tilde{R}_{OBS}^{GOSAT} - \tilde{R}_{CALC}^{GOSAT} \right) - \left(\tilde{R}_{OBS}^{SHIS} - \tilde{R}_{CALC}^{SHIS} \right),$$

$$(5.4\text{-}1)$$

where $\tilde{R}_{OBS}^{GOSAT}$ and $\tilde{R}_{OBS}^{SHIS}$ are the observed TANSO-FTS and S-HIS spectral radiance. $\tilde{R}_{CALC}^{GOSAT}$ and $\tilde{R}_{CALC}^{SHIS}$ are the calculated TANSO-FTS and S-HIS radiance, respectively. The calculation flow of double difference comparison is described in Figure 5.4-1. The observed spectra of TANSO-FTS and S-HIS have applied the finite field of view and wavenumber shift corrections. At this stage, TANSO-FTS and S-HIS have a different spectral resolution of 0.2 cm^{-1} and 0.48 cm^{-1}, respectively. In order to compare with the same spectral resolutions, TANSO-FTS interferograms are truncated by S-HIS Max OPD and set to the S-HIS spectral resolution of 0.48 cm^{-1}.

We assume the uniform surface emissivity and the same vertical profiles of temperature, CO_2, O_3, and H_2O within the TANSO-FTS IFOV in the forward calculation. However, the spatial variation of surface temperature within the playa is more significant than the required calibration accuracy. Therefore, the S-HIS radiance $\tilde{R}_{CALC}^{SHIS}$ is calculated with the induvial scan of surface temperature, and the S-HIS radiance residuals are also calculated with individual scans. At the stage of spectra comparison between TANSO-FTS and S-HIS, we take the average of the S-HIS residuals within the TANSOFTS IFOV as follows:

$$\tilde{R}_{residual}^{SHIS} = \sum_{j} \left(\tilde{R}_{OBS}^{SHIS}(j) - \tilde{R}_{CALC}^{SHIS}(j) \right) / N_j ,$$

$$(5.4\text{-}2)$$

where N_j is the number of S-HIS scans within TANSO-FTS IFOV, $\tilde{R}_{residual}^{SHIS}$ is the averaged S-
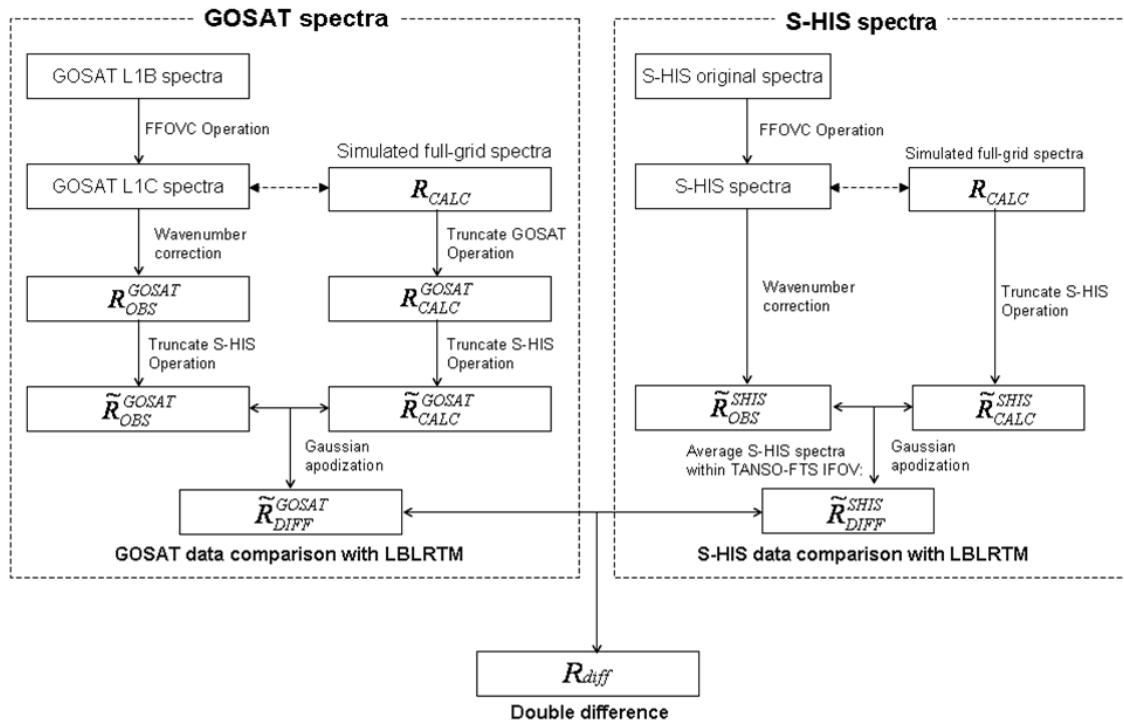
HIS residuals spectra within TANSO-FTS_IFOV.

GOSAT spectra

S-HIS spectra

Figure 5.4-1. Calculation procedure of the double difference comparison between TANSO-FTS and S-HIS.

5.4.2. Double difference comparison of TANSO-FTS and S-HIS

Fig. 5.4-2 shows the TANSO-FTS observed and calculated spectra with 0.48 cm^{-1} spectral resolution and applying the Gaussian filter (here we show the second exposure spectra). Here, we validated the TANSO-FTS Level 1B products V130130, to which the calibration and correction methods are described in Kuze et al. (2012). The top left panel shows the spectral comparison with the entire spectral range of TANSO-FTS Band 4 (650–1800 cm^{-1}). The lower section shows the enlarged figures at CO_2 channels, atmospheric window channels, and O_3 channels. The right panel shows the residual of observed and calculated radiance, respectively. The spectral residuals in the atmospheric window region almost zero, however, large residuals remain in the CO_2 ν_2 band (longer than 700 cm^{-1}) and O_3 band (1040–1060 cm^{-1}).

Figure 5.4-3 shows the S-HIS observed and calculated spectral radiance with 0.48 cm^{-1} spectral resolution and applying the Gaussian filter. S-HIS obtained 36 scans within the TANSO-FTS IFOV at the ER-2 center flight path. The residuals are calculated with each exposure and averaged within TANSO-FTS IFOV. The observed spectral radiance agrees well with the calculated ones except for O_3 channels.

Figure 5.4-4 shows the result of double difference between TANSO-FTS (second exposure) and S-HIS (ER-2 center path observation). The left panel shows the brightness temperature residuals of each sensor. The right panel shows the double difference of TANSO-FTS and S-HIS, respectively. Figure 5.4-5 shows the scatterplots of double differences results as a function of TANSO-FTS brightness temperature in color-coded wavenumbers. The solid line and the bold dashed lines indicate the mean and the 1σ standard deviation. Table 5.4-1 summarized the result of double difference between three exposures of TANSO-FTS and S-HIS (ER-2 center path observation). The double differences almost result in less than 0.5 K except for CO_2 ν_2 band. The other two exposures (TANSO-FTS #1 and #3) shows the same tendency. The O_3 channels are in good agreement within about 0.1 K bias. The atmospheric window region has a positive bias of about 0.5 K with a standard deviation of less than 0.09 K. The warmer temperature in CO_2 channels (700–750 cm^{-1}) also result in about 0.5 K, whereas at cooler temperatures in CO_2 channels (650–700 cm^{-1}) has a significant difference and standard deviation.
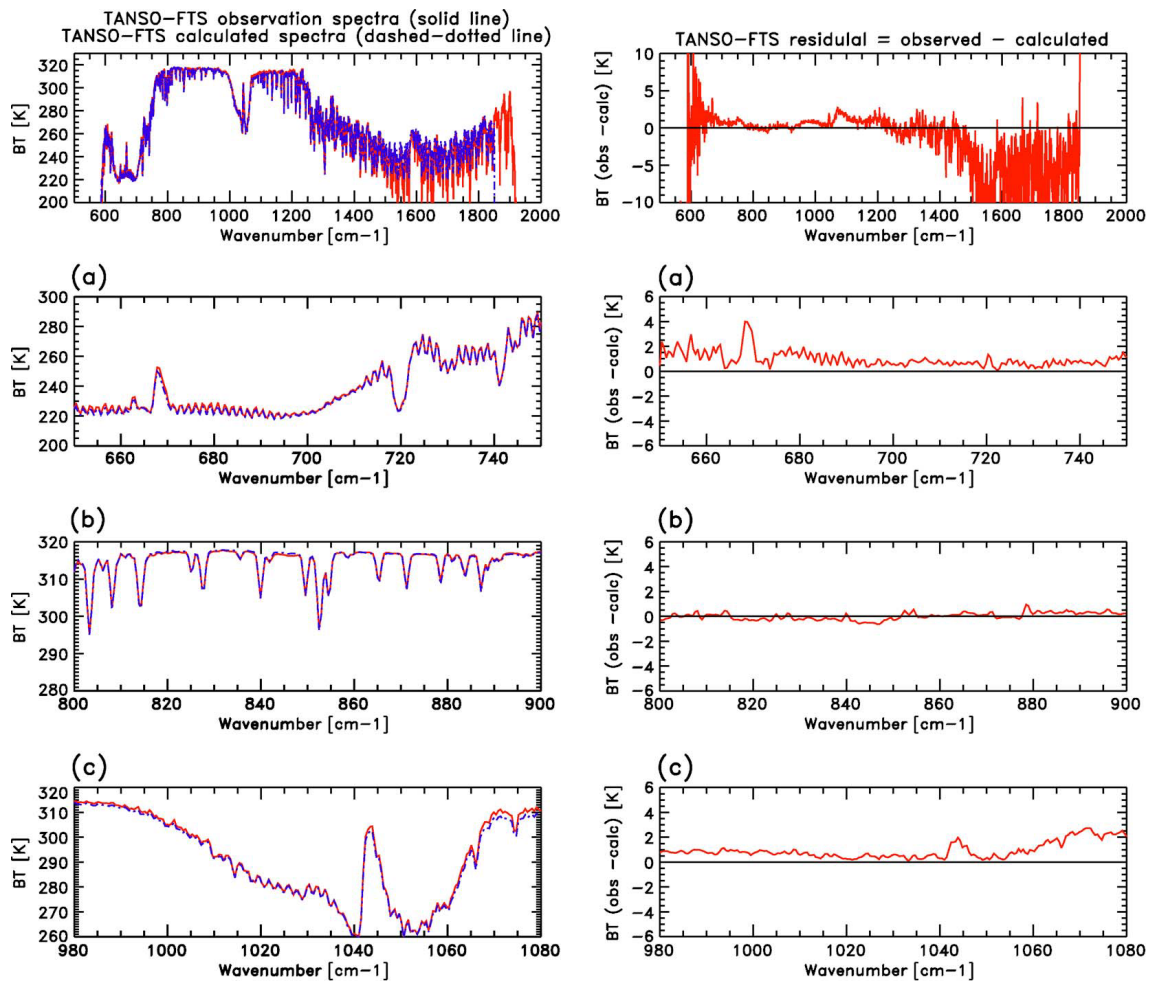
Fig. 5.4-2. Spectral comparison of TANSO-FTS observed and calculated (second exposure). The left top panel shows the spectral comparison in the range of 650–1800 cm^{-1}. The lower section shows the enlarged figures at (a) CO_2 channels, (b) atmospheric window channels, and (c) O_3 channels. The right panel shows the spectral residual between observed and calculated, respectively.
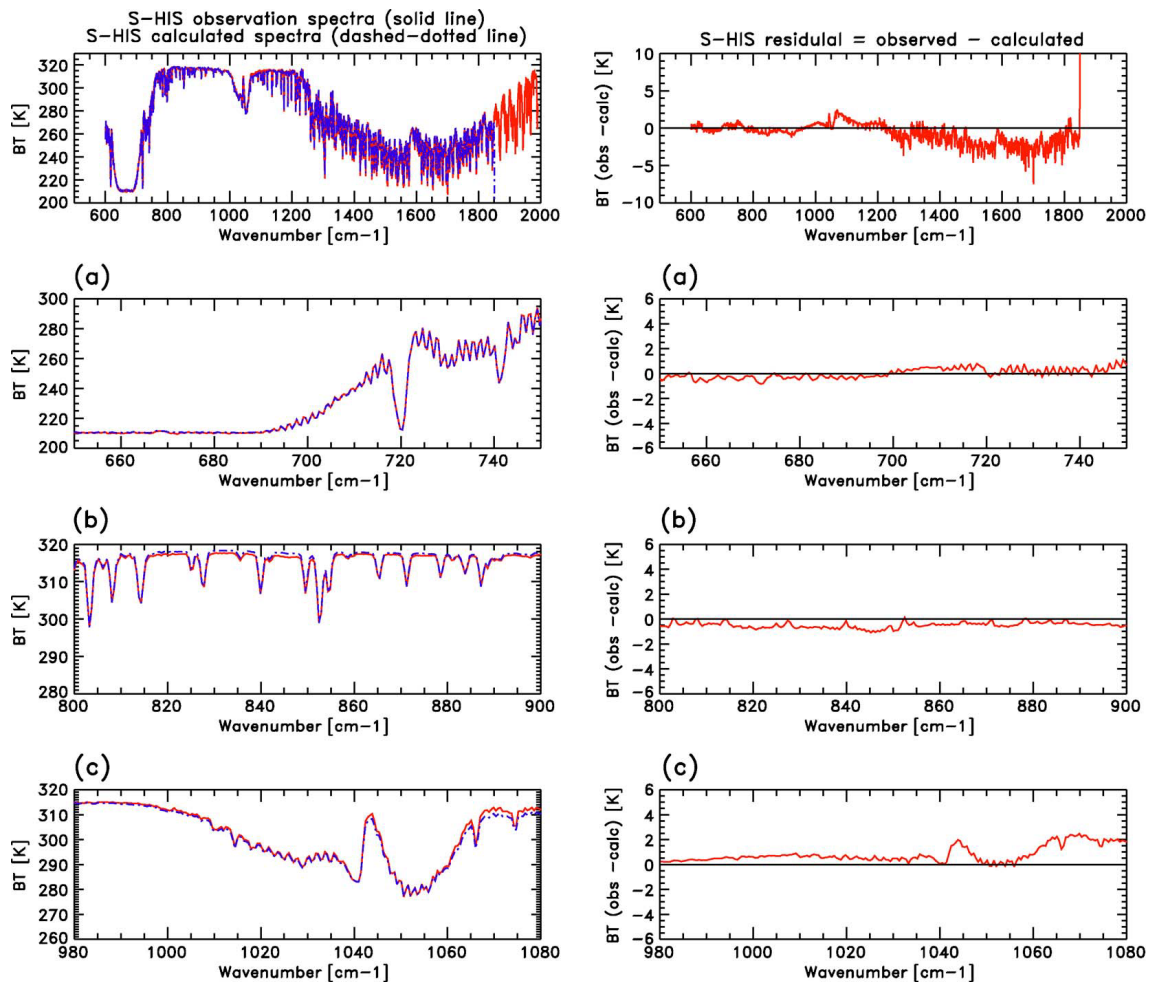
Figure 5.4-3. Spectral comparison of S-HIS observed spectra and calculated spectra at ER-2 center path observation.
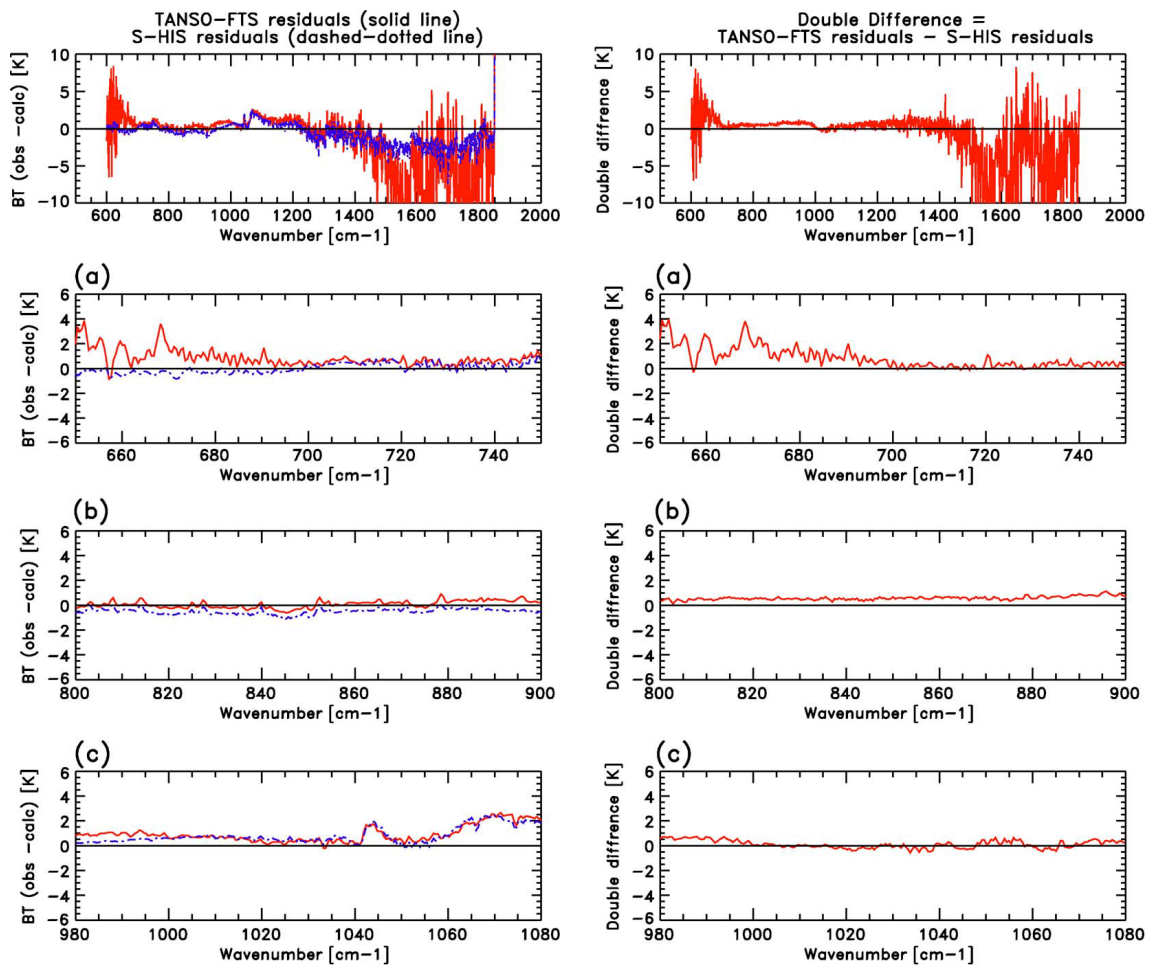
Figure 5.4-4. Results of double difference between TANSO-FTS (second exposure) and S-HIS (ER-2 center path observation). The left panel shows the brightness temperature residuals of each sensor. The lower section shows the enlarged figures at CO_2 channels, atmospheric window channels, and O_3 channels. The right panel shows the double difference of TANSO-FTS and S-HIS, respectively.
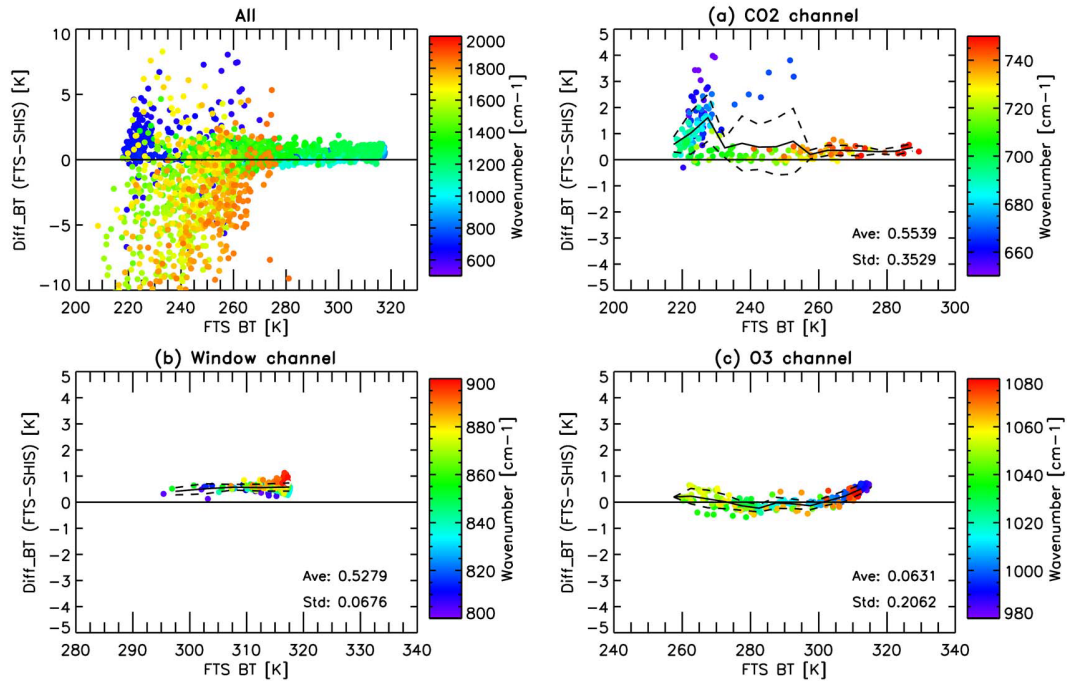
Figure 5.4-5. Scatterplots of double difference of TANSO-FTS and S-HIS as a function of the brightness temperature of TANSO-FTS. The color indicates the frequency. The solid line and bold dashed lines show the mean and the 1 σ standard deviation. The values of mean and standard deviation also indicate in each figure.

Table 5.4-1. Results of double between three exposers of TANSO-FTS and S-HIS at the ER-2 center path observation.

	Wave number	GOSAT #2	GOSAT #3	GOSAT #4
CO$_2$ channels (650 – 750 cm^{-1})	Cooler temp. channels (650 – 700 cm^{-1})	2.207 (1.278)	2.022 (1.058)	2.503 (1.199)
	Warmer temp. channels (700 – 750 cm^{-1})	0.514 (0.051)	0.397 (0.102)	0.441 (0.108)
Window channels (800 – 900 cm^{-1})		0.505 (0.081)	0.528 (0.068)	0.459 (0.089)
O$_3$ channels (980 – 1080 cm^{-1})		0.104 (0.185)	0.063 (0.206)	0.098 (0.194)

The values parenthesis shows the standard deviation.

5.5. Discussion

5.5.1. Sensitivity analysis

A sensitivity analysis is a study of how the double difference result depends upon the input parameters set in the forward calculations. We tested the impact on the double difference by adding the possible error of the atmospheric and surface parameters.

We adopted Vaisala RS92 radiosonde for the vertical profiles of temperature and water vapor up to the ER-2 aircraft altitude. The uncertainties of thermometer and hygrometer are 0.5 K and 5% relative humidity. The uncertainties of O_3 profile are about 10% referred from the climatology database (Vomel et al., 2007), and CO_2 profile is about 3 ppm from GOSAT TANSO-FTS Level 2 product by ACOS team. The surface temperature and emissivity are retrieved with coincident S-AERI measurement. The APOGEE radiometer shows a 2 K peak-to-peak spatial variability of surface temperature within the S-HIS footprint. In this work, we set the same emissivity for TANSO-FTS and S-HIS forward calculation. However, the emissivity has some angular dependence characteristics related to the soil particle size or packing fraction (Pitman et al., 2005), and we set 1% error for the sensitivity analysis. Figure 5.5-1 shows the sensitivity error plots of a single difference and double difference varying with the possible input parameter error mentioned above. These plots indicate the brightness temperature difference between adding error calculating minus nominal calculating at CO_2 cooler channels (650–700 cm^{-1}), CO_2 warmer channels (700–750 cm^{-1}), and window channels (800–900 cm^{-1}). The dashed line means the TANSO-FTS single difference (the residuals between observed and calculated spectra) corresponds to the left y-axis, and the solid line means the double difference (the residual between TANSO-FTS difference and S-HIS difference) corresponds to the right y-axis. For example, at window channels, 5% RH error in water vapor profile results in about 0.5 K for TANSOFTS single difference, however about 0.05 K for double difference. It means the double difference method reduces the errors of the input parameter comparing with the single difference. However, the CO_2 cooler channels hold the potential to have more considerable uncertainties, because these channels are sensitive to high altitude, which does not represent the actual atmospheric state.
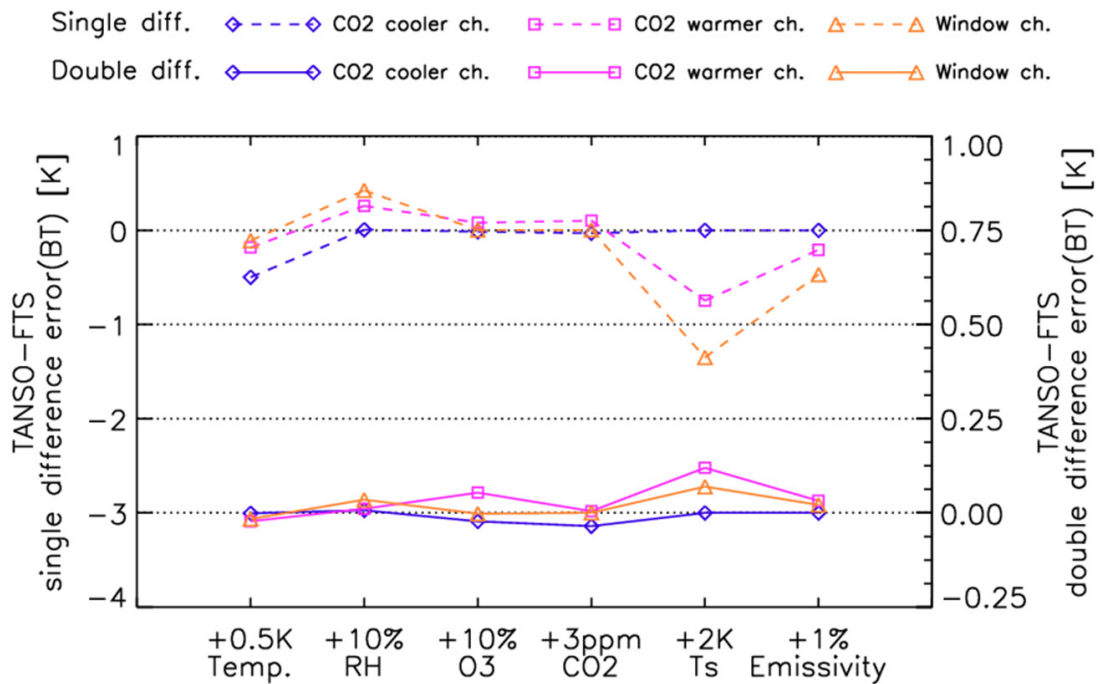
Figure 5.5-1. Sensitivity error plots of single or double difference varying the atmospheric vertical profiles (temperature, relative humidity, O_3, and CO_2) and surface parameters (surface temperature and emissivity). These plots indicate the difference between adding error calculating minus nominal calculating. The dashed line means the TANSO-FTS single difference (the residuals between observed and calculated spectra) corresponds to the left y-axis, and the solid line means the double difference (the residual between TANSO-FTS difference and S-HIS difference) corresponds to the right y-axis.

5.5.2. Error Approximation

The residual of double difference includes the uncertainties of TANSO-FTS and S-HIS measurement, imperfect knowledge of input parameters for forward calculation, the TANSO-FTS pointing accuracy, and spectral resolution reduction. Table 5.5-1 summarized the individual error components of input parameters and S-HIS measurements. The maximum uncertainty, excluding TANSO-FTS measurement, expressed in the root sum of squares (RSS), is less than 0.1 K for 1σ at window channels. Similarly, the RSS difference at CO_2 warmer channels is less than 0.15 K. The residual bias derived from TANSO-FTS pointing accuracy and calibration uncertainty in the TANSO-FTS L1B product. The latter item involves (1) blackbody temperature monitor error, (2) correction of polarization sensitivity, (3) PC-MCT detector nonlinearity, (4) deep space view obscuration, and estimation error of (5) reflection from the blackbody surface (blackbody emissivity error and background radiation model error), and (6) aft optics temperature change between onboard calibrations. In particular, (2), (5), and (6) might have a significant impact on thermal band calibration and cause spectral bias. TANSO-FTS has both SWIR and TIR bands with a single FTS mechanism. Since the SWIR observations remain a priority, the polarization sensitivity is minimized in SWIR bands but larger in TIR band. Also, in the daytime observation, the TIR calibration interval is longer to maximize the SWIR observation time. As the optical throughput is designed to be maximized for high SWIR SNR, the cavity type blackbody with high emissivity cannot be installed due to resource limitations. Additional investigation of the TANSO-FTS TIR calibration is ongoing.

Table 5.5-1 Total uncertainty estimate of double differences expressed in the root sum of squares (RSS) of individual error components at window channels (800-900 cm^{-1}).

Parameter	Uncertainty(1σ)	Source/Comment
[Calculation]		
Uncertainties of input parameters		
-Temperature	<0.02 K	Radiosonde
- Water vapor	<0.04 K	Radiosonde
- Ozone	<0.002 K	Model
- Carbon dioxide	negligible	Model
- Surface temperature	<0.07 K	S-AERI measurement , spatial interpolation error
- Emissivity	<0.02 K	S-AERI measurement, angular dependency characteristics
- Viewing geometry	negligible	Setting vewing angle
- Spectral resolution	negligible	Resolution reduction
[Observation]		
Uncertainties of S-HIS measurement		
	<0.05 K	S-HIS measurement uncertainty (greater than 250K)

Total uncertainty estimate by known source (RSS)

<0.1 K

5.6. Conclusion

In the vicarious calibration campaign, we obtained three different types of FTS observations in RRV playa: satellite-based TANSO-FTS, aircraft-based S-HIS, and ground-based S-AERI with the aim of spectral evaluation of TANSO-FTS TIR band at high-temperature target. We compared TANSO-FTS TIR spectra with S-HIS spectra using the double difference method. This technique utilizes the forward calculations and reduces the effect of differences in the observation geometry and the input parameter error. The atmospheric profile applied for a coincident radiosonde profile and meteorological model data. The surface temperature and emissivity, which are essential in the evaluation of the thermal spectrum, are estimated by a coincident S-AERI upwelling and downwelling radiance. Because the surface temperature has spatial variation within a large TANSO-FTS IFOV, we estimated the TANSO-IFOV-averaged surface temperature using S-HIS spectra.

The results of double difference of TANSO-FTS and S-HIS almost result in 0.1 K at O_3 channels, 0.5 K at atmospheric window channels and CO_2 warmer channels. The residual of double difference contains the uncertainties of less than 0.1 K at window channels and less than 0.15 K at CO_2 warmer channels. The CO_2 cooler channels have large positive residuals with more than 2 K, which includes the imperfect knowledge of input parameters for forward calculations. The S-HIS calibration uncertainty is less than 0.05 K under the environment greater than 250 K. The remaining errors are due to a calibration error in the TANSO-FTS, including the hardware and software, and it is currently under investigation.

6. Long term GOSAT/TANSO-FTS spectral validation and calibration

The TANSO-FTS TIR employed the Mercury Cadmium Telluride Photoconductive detector, which is thermally controlled with the cryocooler and cooled down to 72.7 K. The design of TANSO instrument and prelaunch hardware performance are described in Kuze et al. (2009). The TANSO-FTS TIR band has a wide dynamic range to cover a wide spectral range. Since the Fourier transform spectrometer is based on the linear response for an instrument, the linearity of the detector, amplifiers, and integrated circuits in the analog signal processing chain must be carefully investigated, characterized, and corrected to achieve an accurate radiometric calibration.

In this section, we described the long term GOSAT TANSO-FTS TIR spectral validation with spectral-based and physical quantity-base analysis. These analyses have contributed to the GOSAT TANSO-FTS TIR L1B data update from V201 to V205 (same as V210) with reviewing the non-linearity and offset level estimation.

6.1. Long term TANSO-FTS spectra validation with AIRS

We examined the radiometric stability of the GOSAT TANSO-FTS TIR radiance using time coincident and collocated observation points (called the Simultaneous Nadir Observations: SNOs) of the AIRS sensor from 2009 to 2017. The AIRS sensor employs the grating array spectrometer to measure the thermal spectra with 2378 infrared channels from 3.7 to 15.4 μm. The resolving power of $\lambda/\Delta\lambda = 1200$ and a horizontal footprint diameter of about 13.5 km^2 at nadir. Aumann et al. (2012) have indicated the long-term stability of AIRS spectra as compared with simulated spectra over the night Tropical Ocean. The trend of all AIRS longwave channels with sensitive to the surface was quite small (2 mK/yr). The well-calibrated AIRS dataset has been used to inter-calibration the data of geostationary multi-spectral satellites such as US Geostationary Operational Environmental Satellite system (GOES) and Japanese Multifunctional Transport Satellite (MTSAT) as well as polar orbiting hyper-spectral satellites such as IASI (Hewison, et al., 2013a) and the Cross-track Infrared Sounder (CrIS) aboard the Suomi National Polar-orbiting Partnership Project (Tobin et al., 2013). Hence, the AIRS infrared spectra are suitable for characterizing the radiometric accuracy of the TANSO-FTS sensor as a reference and evaluating its stability. We used AIRIBRAD V005 of AIRS/AQUA Level 1B Infrared geolocated and calibrated radiances from the NASA GESDISC archive. For the time series analysis, we focused on the radiometric comparison in the following spectral regions; CO_2 channel (681.99–691.66 cm^{-1}), window channel (900.31–903.78 cm^{-1}), ozone (O_3) channel (1030.08–1039.69 cm^{-1}), and CH_4 channel (1304.36–1306.68 cm^{-1}) in day and night sides, separately.

At first, we conduct a search of nadir orbit intersections of GOSAT and Aqua satellites for each day. The selecting conditions adopted here for the pixel matchup of nadir TANSO-FTS footprints and AIRS IFOV with the time criterion within 35 min, the distance criterion within 17 km. TANSO-FTS viewing angle selected almost nadir, and the AIRS cross-track angle less than 10°. As shown in Figure 6.1-1, the SNOs are located between 30°and 40°N on the dayside and between 30°and 40°S on the night side. Next, the poor quality of TANSO-FTS data is filtered out if the TIR spectra imaginary part between 800 and 900 cm^{-1} is larger than the noise level. Then, the cloud contaminated TANSO-FTS scenes are screened out if the spatial standard deviation of AIRS brightness temperature at 900 cm^{-1} is larger than 1 K surrounding the TANSO-FTS 10.5 km footprint. Compare to the TANSO-FTS high spectral resolution of 0.2 cm^{-1}, the AIRS resolution is quite low from 0.5 to 1.5 cm^{-1}. The spectral response function (SRF) is expressed as a center wavelength and a full width at half-maximum (FWHM), which

is defined as spectral resolution. Figure 6.1-2 shows the FWHM of AIRS SRF with a spectral range from 600 to 1700cm^{-1}. The FWHM of CO_2, window, O_3, and CH_4 channels are 0.47, 0.64, 0.85, and 1.10 cm^{-1}, respectively. To make the AIRS equivalent TANSO-FTS spectra, the AIRS SRF interpolated to the TANSO-FTS TIR wavenumber scale and multiplied the normalized AIRS SRF to TANSO-FTS spectra and summing over wavenumbers.
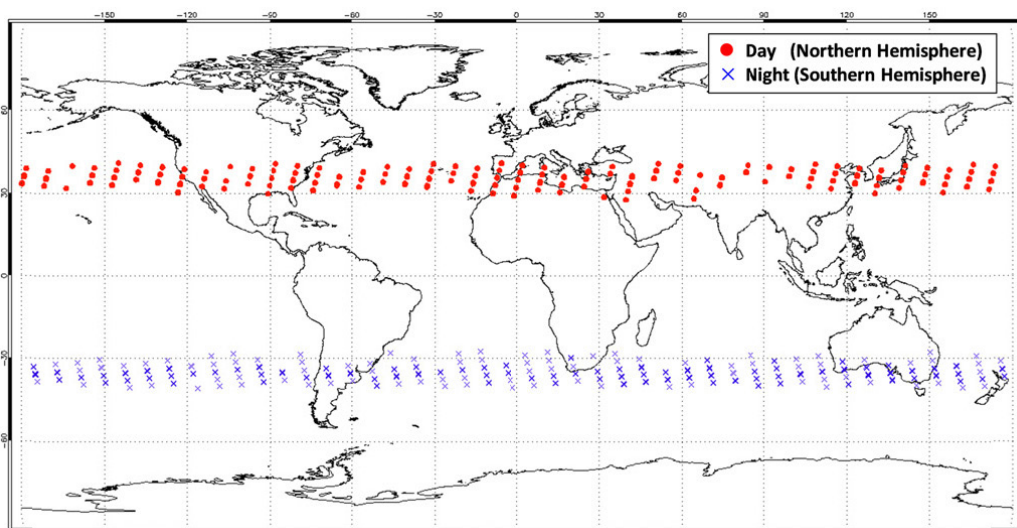

Figure 6.1-1. Map of the GOSAT/TANSO-FTS and Aqua/AIRS SNOs matchup points used in the spectral radiance comparison. The dots and crosses represent the daytime matchups in the northern hemisphere and nighttime ones in the southern hemisphere, respectively.
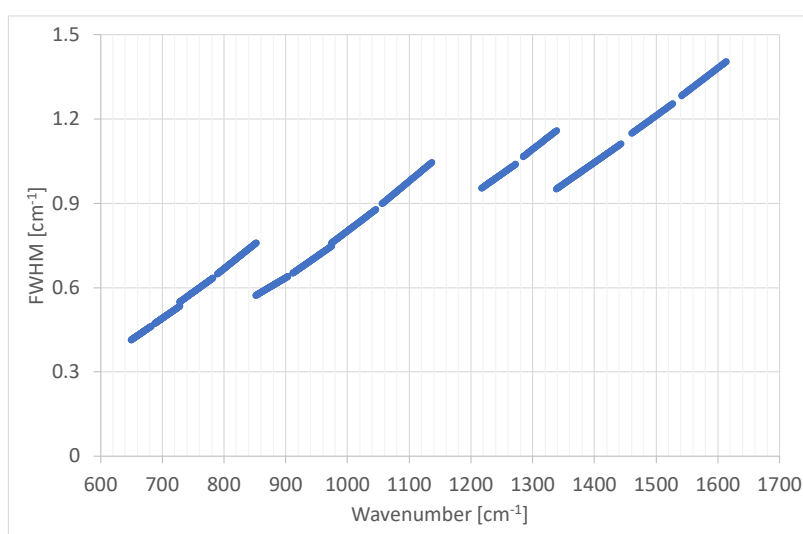

Figure 6.1-2. FWHM of the AIRS spectral response function as a function of wavenumber.

Figure 6.1-3 shows the time series plots of the brightness temperature difference between the TANSO-FTS L1B V201 and the AIRS L1B V005 at CO_2, window, O_3, and CH_4 spectral channels. The figure separately shows the residuals in day observation at Northern Hemisphere and night observation Southern Hemisphere. The number of evaluated SNOs matchups are 1778 points for TANSO-FTS V201. Moreover, a 30-point boxcar-smoothing has applied to the time series of residuals. The TANSO-FTS V201 spectra have a negative bias compare to AIRS, especially in the CO_2 v_2 channel (longer than 700 cm^{-1}) and CH_4 channel. These channels also show the stepwise changes of brightness temperature difference, which were triggered by the GOSAT operation anomalies in May 2014 and in August 2015.
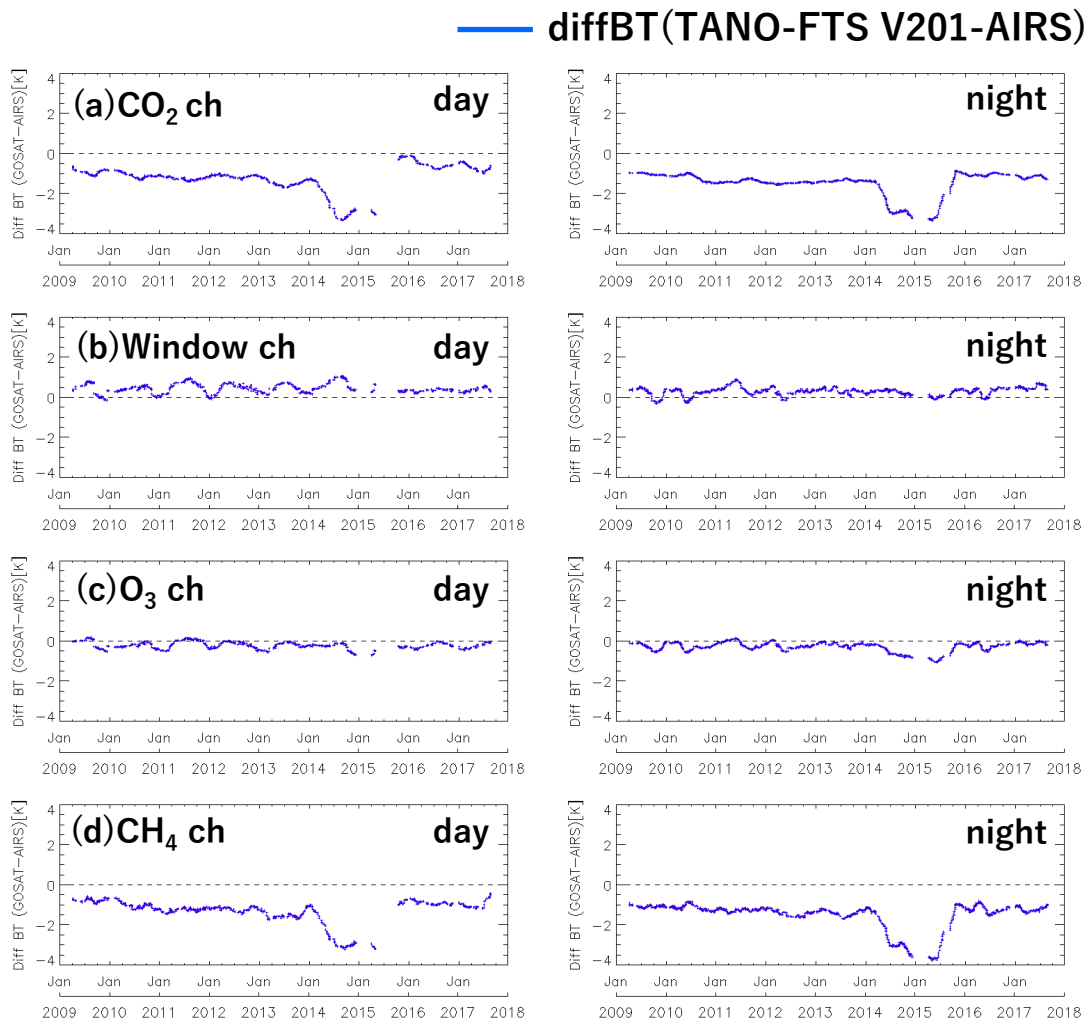

Figure 6.1-3. Time-series plots of the brightness temperature difference between TANSO-FTS L1B V201 and AIRS L1B V005 at (a) CO_2, (b) window, (c) O_3, and (d) CH_4 channels at SNOs matchups. Day and night observations have been analyzed separately.

As mentioned in chapter 4, GOSAT has experienced several significant anomalies since 2014. The cryocooler and/or sensor shutdown strongly affects the thermal condition of TANSO-FTS. In May 2014, both cryocooler and the TANSO-FTS mechanics shut down. The TANSO-FTS optics and background warmed up, but a temperature-controlled detector cooled down. As shown in Figure 4.3-4, the plausible buildup of ice contamination on the thermal coupler has affected the thermal conduction between the cryocooler cold head and the detector. In August 2015, the only cryocooler had shut down suddenly, and other electronics continued to work normally. The cryocooler cooldown restarted six weeks after the anomaly. During the suspension of cooling, only the detector warmed up from 72.7 K to ambient temperature of about 295 K, and it might have decontaminated the thermal coupler. This situation explains the sudden increase and decrease in the temporal behavior of the background radiation. However, the temperature resolution of the PC-MCT detector is quite coarse 0.7 K to estimate the change of the background radiation from the TANSO-FTS optics and environment. The previous TANSO-FTS Level 1 versions of V161 and V201, the background radiation from the TANSO-FTS optics and environment was underestimated, and hence, the value of $V_{DCoffset}(t)$ was too low. As well as no consideration for the seasonal variation or stepwise changes that might have occurred just before and after cryocooler anomalies.

In this study, we estimated the sensitivity of background radiation $V_{DCoffset}$ and the detector temperature in the CO_2 band from the brightness temperature difference between TANSO-FTS and AIRS. In the TANSO-FTS V210 and later versions, we have prepared a table of $V_{DCoffset}$ as a function of day since launch for seamless data processing. Along with a new estimate of the $V_{DCoffset}$, the quadratic non-linearity correction coefficient a_{nlc} was also revised to be 0.7057 V^{-1} for the TANSO-FTS V210 and later versions. Figure 6.1-4 shows the table of $V_{DCoffset}$ before and after the revision. The table of V210 and later versions include a seasonal change and significant stepwise changes in May 2014 and August 2015, in response to the cryocooler shutdowns.

By applying a proper time dependent $V_{DCoffset}$ in FTS V210, the stepwise changes have been minimized, and the spectral residuals with AIRS have been reduced considerably, as shown in Figure 6.1-5.
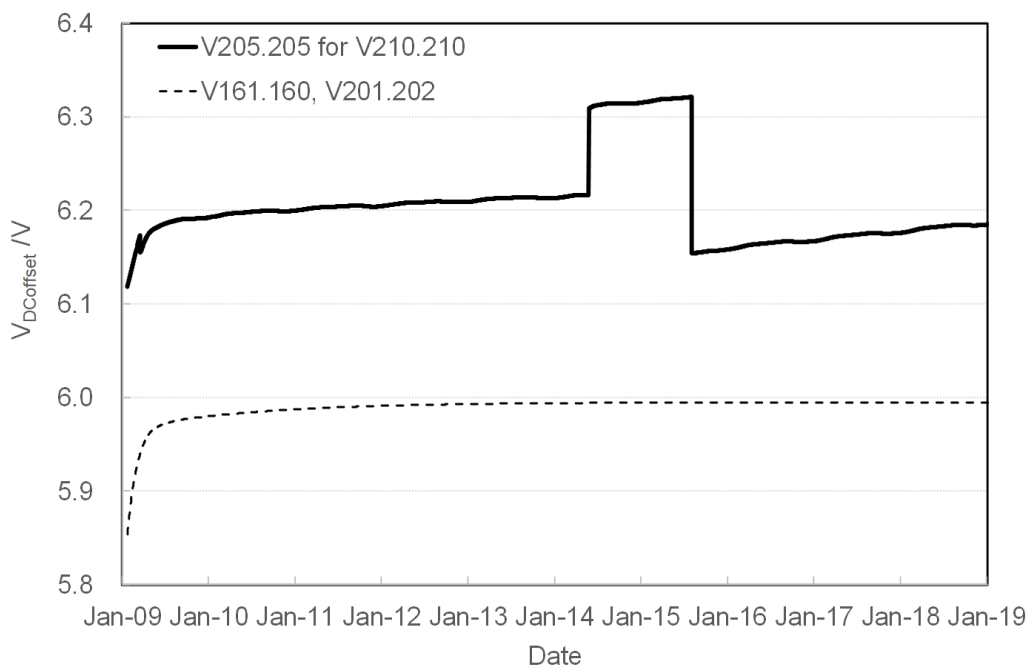
Figure 6.1-4. Background radiation $V_{DCoffset}$ models since launch in different TANSO-FTS Level 1 versions. The dashed line shows $V_{DCoffset}$ in V161 and V201, which underestimated the background radiation and detector temperature. The solid bold line shows $V_{DCoffset}$ in V210, an updated version based on the reanalysis of background radiation and includes a seasonal variation. The instrumental anomalies that occurred in 2014 and 2015 have also incorporated into this new version.

The spectral radiances of the TANSO-FTS TIR band are calculated with the equation of complex radiometric calibration based on Revercomb et al. (1998) using the closest calibration data of onboard BB and the DS view. The GOSAT nominal calibration frequency is twice in the daytime and four times in nighttime observations. Figure 6.1-6 shows the correlation plot of the residuals between the TANSO-FTS V210 and AIRS and the time difference between Earth observation and calibration time. The data in (b) window channel are not strongly correlated with the calibration time difference, while (a) CO_2, (c) O_3, and (d) CH_4 channels show the positive correlation in the dayside and the negative correlation in the night side. This suggests that the detector temperature and/or analog electronics variation in an orbital cycle causes the $V_{DCoffset}$ change. Although V210 does not include an orbital cycle of $V_{DCoffset}$, the consideration of this effect would improve the retrieval accuracy of CO_2 or CH_4 from the TANSO-FTS TIR spectra.
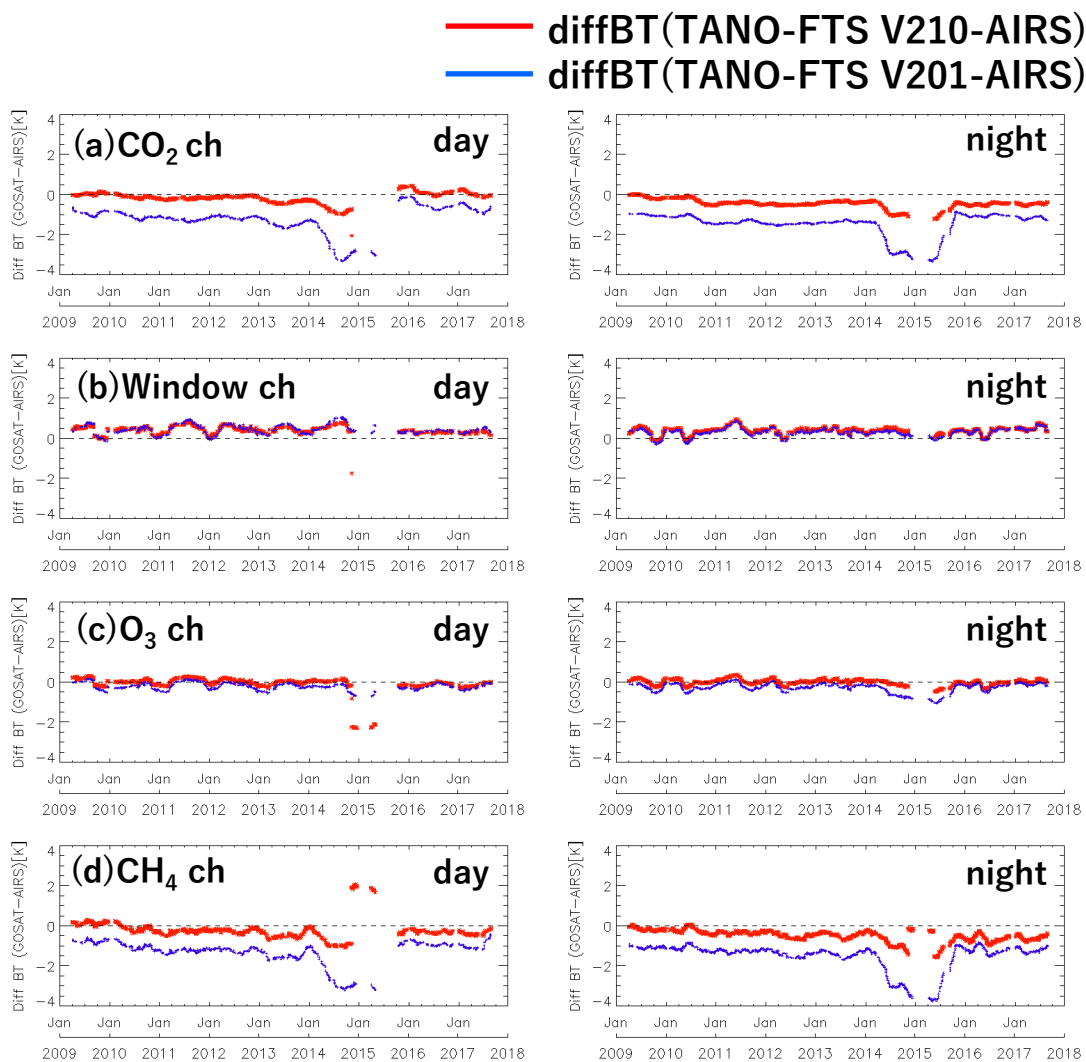
Figure 6.1-5. Time-series plots of brightness temperature difference between TANSO-FTS and AIRS at (a) CO_2, (b) window, (c) O_3, and (d) CH_4 channels at SNOs matchups. Day and night observations have been analyzed separately. The blue and red line indicates the residuals between AIRS and TANSO-FTS V201 or TANSO-FTS V210, respectively.
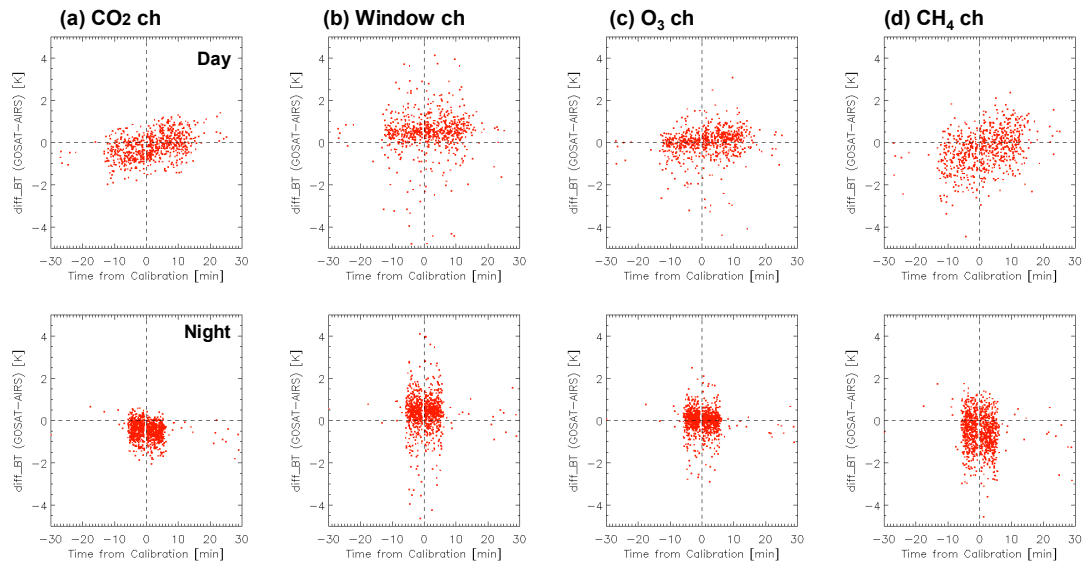
Figure 6.1-6. Correlation plots of the residuals between TANSO-FTS V210 and AIRS and the time difference between Earth observation and the closest calibration data acquisition for (a) CO_2, (b) window, (c) O_3, and (d) CH_4 channels. Upper figures show the results for the dayside observations, and lower ones are nightside observations. The positive correlation is found for the daytime data and the negative correlation for the nighttime data except for the window channel.

6.2. Long term TANSO-FTS sea surface temperature validation with buoy data

The SNOs inter-comparison between GOSAT and AIRS are limited in north or south mid-latitude from 30° to 40°, we conducted the comparison with global sea surface temperature (SST) between the in-situ buoy data and retrieved value from TANSO-FTS TIR spectra. The SST retrievals from TANSO-FTS TIR spectra used an atmospheric window region (10–12 μm), where is less affected by the absorption of trace gases and water vapor. The in-situ SST Quality Monitor (iQuam) Version 2.0 dataset has been processed at the National Oceanographic and Atmospheric Administration Center for Satellite Application and Research (Xu et al., 2014). iQuam retain the SST dataset from ships, drifting buoys, moored buoys, and Argo floats, which are processed with quasi real-time. The vertical temperature structure of SST is variable and complex depending on the level of shear-driven ocean turbulence and the air-sea fluxes of heat, moisture, and momentum (Donlon et al., 2002, 2008). The depth of the SST measurement depends on the observation technique and sensor frequency described in Figure 6.2-1. TANSO-FTS TIR spectra at 10–12 μm measures the skin SST, within the depth of approximately less than 1 m. The drifting buoys are the most applicable for TANSO-FTS retrievals, and they can collect throughout the world's oceans.
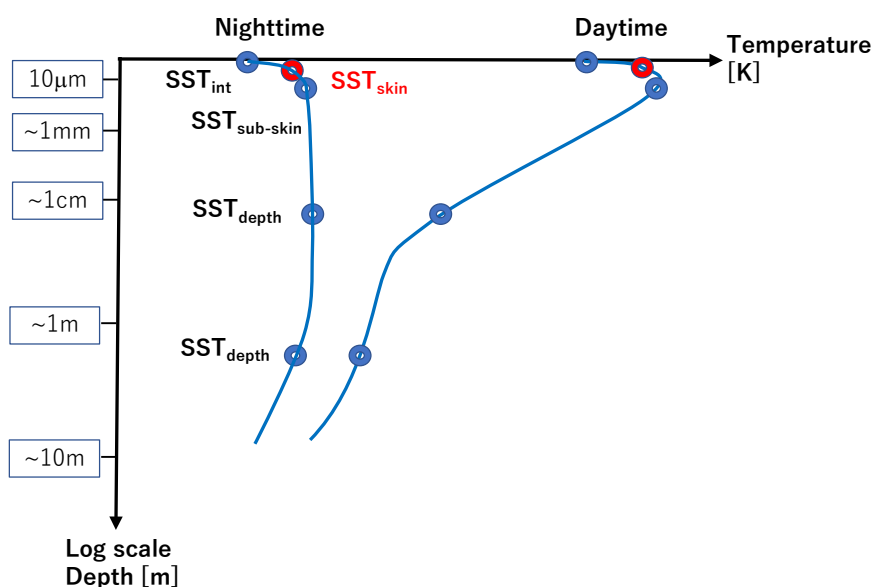

Figure 6.2-1. Temperature stratification of the typical sea surface and underwater in daytime and nighttime. The sensor measurement frequency depends on the depth of underwater temperature.

The GOSAT and iQuam matchup criteria in this work are set with the collocation of 50 km and time difference of 30 min. The cloud screening was applied with the split window technique using the atmospheric window channels of 11 and 12 μm, which is known to be a robust cloud screening method, especially for a thin cirrus cloud (Inoue, 1985). Over the cloud-free oceans, the brightness temperatures difference between11 and 12 μm is mostly proportional to the absorption/emission of atmospheric water vapor. We calculated cloud-free radiance of 11 and 12 μm using the LBLRTM radiative transfer model setting five atmospheric models with varying the values of SST. Table 6.2-1 describes the details of model setting by the season, latitude, and day/night. The linear regression formula was estimated between the SST and the brightness temperature at 11 and 12 μm. Then, we applied this formula to TANSO-FTS TIR spectra with matched iQaum SST and screen out for the cloud scene.

We estimated SST values from brightness temperatures of the TANSO-FTS TIR spectra in the window region using the multiple channel SST (MCSST) method (Kilpatrick et al., 2001). The MCSST method uses two split-window channels to calculate the transmittance through from the surface to the satellite. This method also considers the zenith angle dependence of the atmospheric radiation. The value of SST, *Ts*, is calculated as follows:

$$T_s = c_1 + c_2 T_i + c_3\big(T_i - T_j\big) + c_4\big(T_i - T_j\big)(1 - sec\theta),$$

$$(6.2\text{-}1)$$

where T_i, T_j, and θ are the brightness temperature at 11 and 12 μm of the TANSO-FTS, and the satellite zenith angle, respectively. The parameters $c_1 - c_4$ are regression coefficients calculated from training data, which is clear-sky TANSO-FTS data and matched iQaum SST data in 2011. In this analysis, the regression coefficients are calculated by the season, latitude, and day/night time, separately. The classification of the regression coefficients corresponds to Table 6.2-1. We retrieved the SST values globally from the TANSO-FTS V210 spectra in the long-term from March 2009 to March 2017. Figure 6.2-2 shows the time series of daily mean SST difference (GOSAT-retrieved SST minus iQuam drifting buoy SST) and 30-point running mean. The time trend of SST difference of day and night sides is 3.93 and 10.39 mK/yr, respectively. These results suggest that there is no significant time trend and anomaly in the window channel of the TANSO-FTS TIR spectra relative to the in-situ SST observations, which ensures the TANSO-FTS radiance stability.

Table 6.2-1. Atmospheric model setting used for the linear regression formula of cloud screening and SST retrieval regression coefficients.

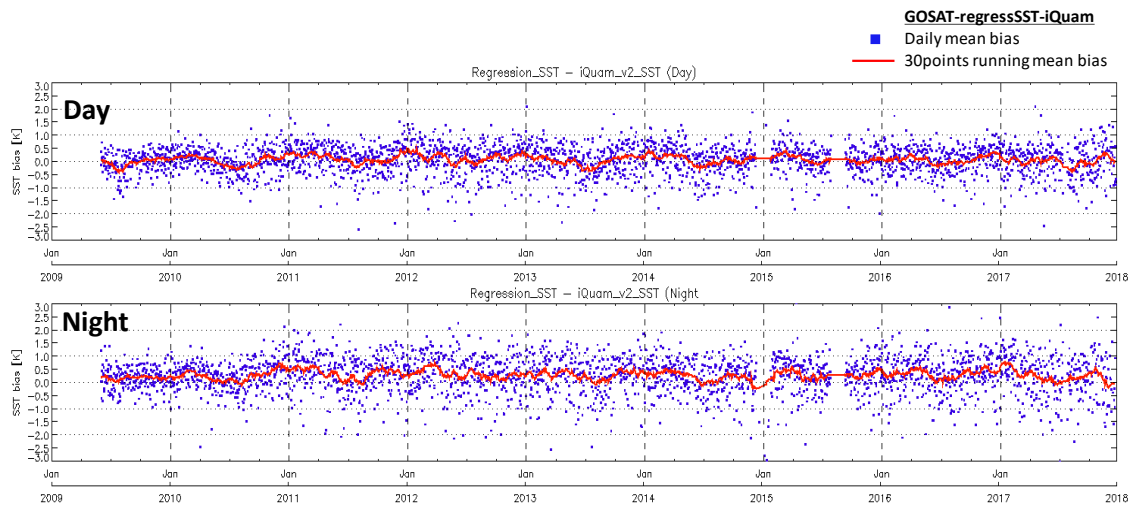| Model	Latitude	Season
Tropical	20°S ~ 20°N	All Season
Mid-latitude summer	20°N ~ 55°N	May ~ Oct
	20°S ~ 55°S	Nov ~ Apr
Mid-latitude winter	20°N ~ 55°N	Nov ~ Apr
	20°S ~ 55°S	May ~ Oct
Subarctic summer	>55°N	May ~ Oct
	<55°S	Nov ~ Apr
Subarctic winter	>55°N	Nov ~ Apr
	<55°S	May ~ Oct

Figure 6.2-2. Time-series plots of the difference between TANSO-FTS retrieved SST and iQuam drifting buoy SST. Small dots show the daily mean SST bias (TANSO-FTS -retrieved SST minus iQuam drifting buoy SST), and the solid line indicates the 30-point running mean.

6.3. Conclusion

This chapter has described the long-term validation of the TANSO-FTS Level 1 TIR band with spectral-based and SST-based analysis.

During the long-term operation of GOSAT, two significant anomalies occurred on 24 May 2014, and 2 August 2015. These sudden anomalies affected the TIR radiometric calibration considerably. At the time of cryocooler shutdowns, the step changes were seen in the value of $V_{DCoffset}$. To review and make the new $V_{DCoffset}(t)$ model and the nonlinear correction, it is useful to use the spectral validation with a well-calibrated AIRS and TANSO-FTS. We estimated the sensitivity of background radiation $V_{DCoffset}$ and the detector temperature in the CO_2 band from the TANSO-FTS and the AIRS analysis. Applying the proper time-dependent $V_{DCoffset}$ model and reprocessed the TANSO-FTS V210 product, the stepwise changes of the spectral residuals between AIRS and TANSO-FTS, especially in the CO_2 channel and CH_4 channel, has been reduced compare to the previous version of TANSO-FTS product.

The comparison between TANSO-FTS retrieved SST and in-situ iQuam SST has confirmed the long-term stability of the TANSO-FTS spectra at the window channel. The temporal trends of SST difference between TANSO-FTS retrieved SST and iQuam SST are found to be 3.93 mK/yr at day and 10.39 mK/yr at night. It means the no noticeable trend in the window channel of the TANSO-FTS TIR spectra from launch.

7. Summary

7.1. Other issues relating to GOSAT/TANSO-FTS TIR Level 1B data

The TANSO-FTS L1B V210 spectra have been corrected by reviewing the non-linearity of the detector. The background radiation $V_{DCoffset}$ depends on the detector-amplifier temperature, and its value has been modeled as a function of the elapsed time since launch. The $V_{DCoffset}(t)$ model incorporates the effects of stepwise changes triggered by the GOSAT operation anomalies up until 2015. However, additional GOSAT operation anomalies occurred in 2018, which may also affect the thermal properties of the FTS optics.

On 17 May 2018, GOSAT transferred to the least load mode (LLM), and all instruments and data recorders were shut down due to a "Command and Data Management System (CDMS)" incident. The FTS nominal heater control restarted 3 days after the anomaly occurred, and the cryocooler began cooling after 5 days. This situation was similar to the anomaly that occurred when the solar paddle stopped rotating in May 2014. On 24 November 2018, GOSAT transferred to the LLM again, and TANSO-FTS was shut down. The FTS nominal heater control restarted 4 days after the anomaly, and the cryocooler began cooling after 27 days. This situation was similar to the cryocooler shut-down in August 2015. Table 7.1-1 summarizes the sensor startup sequence for each anomaly event.

Recall that $V_{DCoffset}$ strongly depends upon the environmental temperature. The thermal gradient between the cryocooler cold head and the detector creates ice contamination or decontamination on the thermal coupler. For the anomalies in May 2014 and May 2018, both the cryocooler and the TANSO-FTS mechanics were shut down. The TANSO-FTS optics and background warmed up, but the temperature-controlled detector cooled down. This situation may have caused ice contamination. For the anomalies on August 2015 and November 2018, only the detector warmed up, which may have decontaminated the thermal coupler.

Based on the analysis of past anomaly events, an increase or decrease in $V_{DCoffset}$ appears to relate to the period from the start of the FTS heater control to the cryocooler cooling. Therefore, we must allocate enough time for the FTS heater control to avoid a thermal hysteresis of FTS optics.

Table 7.1-1.　TANSO-FTS sensor startup sequence for each anomaly event.

No	Event	Elapsed days	Day	UT	Event
1	2009/02 LLM transition →Restart	0	2009/2/26	22 UT	LLM transition
			2009/2/27	01 UT	FTS-ELU ON FTS nominal heater control start
				09 UT	FTS-C ON、PM-C(A) ON、TEC-C ON、S-ASP ON
				09 -12 UT	Cryocooler cool down
		2	2009/2/28	01 UT	T-ASP ON, S-DET cooling
		5	2009/3/3	03 UT	FTS checkout operation restart by SCMD
2	2014/05 LLM transition →Restart	0	2014/5/24	23 UT	LLM transition (rotation of one of the two solar paddles stopped)
		3	2014/5/27	23 UT	FTS-ELU ON FTS nominal heater control start
		4	2014/5/28	06 UT	PM-C(A) ON
				10 UT	TEC-C ON
				12 UT	FTS-C、S-ASP ON
				12 -15 UT	Cryocooler cool down
		5	2014/5/29	03 UT	T-ASP ON, S-DET cooling
		6	2014/5/30	03 UT	FTS observation restart by SCMD
3	2015/08 cryocooler shutdown →Restart	0	2015/8/2	03 UT	Cryocooler shutdown
		43	2015/9/14	00 -03 UT	Cryocooler cool down
				06 UT	T-ASP ON
		44	2015/9/15	02 UT	FTS observation restart by SCMD
4	2018/05 LLM transition →Restart	0	2018/5/18	09 UT	LLM transition (GOSAT CDMS trouble)
		2	2018/5/20	12 -14 UT	FTS-ELU ON FTS nominal heater control start
		5	2018/5/23	03 UT	FTS-C ON、PM-C(B) ON、TEC-C ON、S-ASP ON
				05 - 07 UT	Cryocooler cool down
				14 UT	T-ASP ON
		6	2018/5/24	02 UT	FTS observation restart by SCMD
				04 UT	S-DET cooling
5	2018/12 LLM transition →Restart	0	2018/11/24	19 UT	LLM transition (rotation anomaly of the second solar-paddle)
		4	2018/11/28	03 UT	FTS-ELU ON FTS nominal heater control start
		27	2018/12/21	03 UT	TEC-C ON
				07 UT	PM-C(B) ON
				03 -06 UT	Cryocooler cool down
		31	2018/12/25	01 UT	S-ASP ON、FTS-C ON
				15 UT	T-ASP ON, S-DET cooling
		32	2018/12/26	01 UT	FTS observation restart by SCMD

Optical system unit
　　　S-DET : Short wavelength infrared detector
　　　T-DET: Thermal infrared detector
　　　S-ASP : Short wavelength infrared analog processing unit
　　　T-ASP : Thermal infrared analog processing section
Control system unit
　　　FTS-C : Interferometer drive controller
　　　PM-C :Pointing control unit
　　　TEC-C : Electronic cooling control circuit
　　　A: primary, B: Secondary
Electric circuit unit
　　　ELU : Electrical circuit unit

The spectral validation using AIRS (see Chapter 6) shows that there is some spectral bias, especially in the CO_2 and CH_4 channels. This is probably due to the uncertainty in orbital and/or seasonal variation of $V_{DCoffset}$. More frequent calibration is effective for better spectral quality; however, it is a trade-off between the quantity of observational data and TIR radiometric accuracy. For further improvements, the $V_{DCoffset}(t)$ model must include an orbital phase. Other potential sources of calibration uncertainty are the prelaunch model of polarization sensitivity in the TANSO-FTS optics, and the emissivity of onboard BB.

7.2. Conclusion

In this thesis, we describe the GOSAT TANSO-FTS TIR band calibration of radiance spectra and its radiometric validation. TANSO-FTS Band 4 uses a PC-MCT detector, which is often used for large footprint observation with high spectral resolution. The PC-MCT detector is known to have a non-linear response to input photons, causing critical radiometric errors in quantitative spectroscopic measurements. A correction for non-linearity has been applied to all the interferograms, including scene flux, blackbody, and deep-space calibration view. However, the TANSO-FTS measures scene flux with wide dynamic range and broad spectral coverage using a single detector, making it difficult to characterize and calibrate the errors of the TANSO-FTS TIR radiance effectively for decade long observation in space. Especially, TIR radiance at low temperature, which is absorbed by atmospheric CO_2, CH_4, and other gas, is quite different from onboard blackbody temperature and required an accurate non-linearly correction.

We utilized spectral comparison with a well-calibrated sensor, which is an effective means for calibration and validation of the TANSO-FTS TIR spectra. Specifically, we used an aircraft-based FTS sensor (S-HIS) over a hot desert site using the double-difference method. This method utilizes forward model calculations and reduces the effect of differences in observation geometry between the TANSO-FTS and S-HIS and, in turn, the input parameter error. The surface temperature and emissivity, which are crucial in the TIR spectrum, were retrieved from the simultaneous measurement of ground-based FTS (S-AERI). We evaluated an entire spectral range of TANSO-FTS Band 4 with uncertainty within about 0.1 K.

Over its 10-year operating period, GOSAT has experienced several anomalies in the thermal properties of the TANSO-FTS. The response of the PC-MCT detector has a non-linear characteristics and strong temperature dependency. The background radiation changes arising from the thermal condition changes of FTS optics and environment subsequently cause radiometric errors in the TANSO-FTS TIR spectra. In addition, the temperature resolution of the PC-MCT detector is too coarse (0.7 K) to estimate the changes in background radiation. We made the effectiveness of background radiation and non-linearity correction models using spectral validation with a well-calibrated AIRS dataset. From the TANSO-FTS Level 1B V210 processing, the background radiation has been modeled as a function of the elapsed time since launch. It accounts for stepwise changes that may have occurred just before and after anomalies in the thermal properties of the TANSO-FTS.

GOSAT has the advantage of being able to measure the same field of view in both SWIR and TIR spectra simultaneously. However, this makes it difficult to ensure radiometric accuracy. On-orbit calibration for the TIR band cannot be conducted frequently, as it interrupts the SWIR observation. Therefore, the challenge is to use limited on-orbit calibration data, e.g., by estimating the change in environmental temperature between the Earth and deep-space calibration views, while applying more accurate background radiation at the same time as the Earth observation.

Some contaminants, including water vapor, ice, and other substances, remain around the spacecraft and instruments following an initial outgassing period. During the long-term operation, sudden occurrences of satellite or sensor shutdown are unavoidable, and contamination control is required. In this study of the GOSAT, we have learned that it is important to establish a start-up procedure for the sensor and heat source equipment, while considering the thermal conditions of the optical system, to avoid a thermal hysteresis.

This work contributes to the provision of consistent data quality from the TANSO-FTS in the TIR spectra for a 10-year period.

Reference

Abe, O., Kawasaki, K., Wakaki, M.: Improvement of Nonlinearity and Extension of Wavelength Region Using Tandem (PV+PC) Type HgCdTe Detector (Dual-MCT) in FTIR Spectrometer, *Journal of Elec Materi*, 28: 858. https://doi.org/10.1007/s11664-999-0084-0,1999.

Antonelli, P., Revercomb, H.E., Sromovsky, L.A., Smith, W.L., Knuteson, R.O., Tobin, D.C., Garcia, R.K., Howell, H.B., Huang, H., and Best, F.A.: A principal component noise filter for high spectral resolution infrared measurements, *J. Geophys. Res.*, vol. 109, no. D23, p. D23 102, 2004.

Aumann, H. H., Elliott, D., Strow, S.: Validation of the Radiometric Stability of the Atmospheric Infrared Sounder, Proc. SPIE 8510-28, August, 2012.

Aumann, H.H., Broberg, S., Elliott, D.A., Gaiser, S.L., and Gregorich, D: Three years of Atmospheric Infrared Sounder radiometric calibration validation using sea surface temperatures.: Three years of Atmospheric Infrared Sounder radiometric calibration validation using sea surface temperatures, *J. Geophys. Res.*, 111, D16S90, doi:10.1029/2005JD006822, 2006.

Baldridge, A. M., Hook, S. J., Grove, C. I. and Rivera, G.: The ASTER spectral library version 2.0, *Remote Sens. Environ.*, vol. 113, no. 4, pp. 711–715, 2009.

Baldridge, A. M., Hook, S.J., Grove, C.I. and Rivera, G.: The ASTER Spectral Library Version 2.0., *Remote Sensing of Environment,* vol 113, pp. 711-715, 2009.

Bartoli, F., Allen, R., Esterowitz, L., and Kruer, M.: Auger‐limited carrier lifetimes in HgCdTe at high excess carrier concentrations, *J. Appl. Phys.* 45, 2150, 1974.

Beer, R. et al.: TES Level 2 Algorithm Theoretical Basis Document, Jet Propulsion Laboratory, California Institute of Technology Pasadena, California, Version 1.1, JPL D-16474, Oct. 1999.
Beer, R., Glavich, T. A. and Rider, D. M.: Tropospheric emission spectrometer for the Earth Observing System's Aura satellite, *Applied Optics*, Vol. 40, No. 15, May 20, 2001.

Berk, A., Conforti, P., Kennett, R., Perkins, T., Hawes, F. and Bosch, J. : MODTRAN6: a major upgrade of the MODTRAN radiative transfer code, Proc. SPIE 9088, Algorithms and Technologies for Multispectral, Hyperspectral, and Ultraspectral Imagery XX, 90880H (June 13, 2014); doi:10.1117/12.2050433 ,2014.

Berk, A., Conforti, P., and Hawes, F. : An accelerated line-by-line option for MODTRAN combining on-the-fly generation of line center absorption with 0.1 cm-1 bins and pre-computed line tails, Proc. SPIE 9471, Algorithms and Technologies for Multispectral, Hyperspectral, and Ultraspectral Imagery XXI, 947217 (May 21, 2015); doi:10.1117/12.2177444, 2015.

Bluefield Technologies, URL: https://bluefield.co/ (accessed on 15 October 2019).

Blumstein, D., Péquignot, E., Buffet, L., Buil, C., Hébert, P., Larigauderie, C., Phulpin, T., Camy-Peyret ,C. and Siméoni ,D. : The IASI instrument, ECMWF/EUMETSAT NWP-SAF Workshop on the assimilation of IASI in NWP, 6 – 8 May 2009.

Bormann, N. and Healy, S. B.: A fast radiative‐transfer model for the assimilation of MIPAS limb radiances: Accounting for horizontal gradients, *Q.J.R. Meteorol. Soc.*, 132: 2357-2376. doi:10.1256/qj.05.160, 2006.

Bradbury, L. M., Ligori, M., Spina, R., Kekez, D., Lukaszynski, P., Zee, R. E, Germain, S. : On-Orbit Greenhouse Gas Detection with the GHGSat Constellation, Proceedings of the 69th IAC (International Astronautical Congress) Bremen, Germany, 1-5, paper: IAC-18.B4.4.8, 2018.

Buchwitz, M., de Beek, R., Burrows, J. P., Bovensmann, H.,Warneke, T., Notholt, J., Meirink, J. F., Goede, A. P. H., Bergamaschi, P., Körner, S., Heimann, M., and Schulz, A.: Atmospheric methane and carbon dioxide from SCIAMACHY satellite data: initial comparison with chemistry and transport models, *Atmos. Chem. Phys.*, 5, 941–962, https://doi.org/10.5194/acp-5-941-2005, 2005.

Buehler, S. A., Eriksson. P., Kuhn, T., von Engeln, A., Verdes, C.: ARTS, the atmospheric radiative transfer simulator, *J Quant Spectrosc RadiatTransfer*, 91, 65–93, 2005.

Caceci, M. S. and Cacheris, W. P.: "Fitting curves to data: The Simplex algorithm is the answer, BYTE Magazine, pp. 340-362, May, 1984.

Calvo B., E., Guendehou, S., Limmeechokchai, B., Pipatti, R., Rojas, Y., Sturgiss, R., Tanabe, K., Wirth, T., Romano, D., Witi, J., Garg, A., Weitz, M. M., Cai, B., Ottinger, A. D., Dong, H., MacDonald, D. J., Ogle, M. S., Rocha, R. M., Sanchez, José Sanz, M., Bartram, M. D., Towprayoon, S. : 2019 Refinement to the 2006 Guidelines for National Greenhouse Gas Inventories, https://www.ipcc-nggip.iges.or.jp/public/2019rf/index.html, (accessed on 1 February, 2020).

Chahine, M.T., Chen, L., Dimotakis, P., Jiang, X., Li, Q., Olsen, E. T., Pagano,T., Randerson, J., Yung, Y. L. ; Satellite Remote Sounding of Mid-Tropospheric CO2, *Geophys. Res. Lett.*, 35, L17807, doi:10.1029/2008GL035022, 2008.

Clough, S. A., Iacono, M. J., and Moncet, J.-L.: Line-by-line calculation of atmospheric fluxes and cooling rates:Application to water vapor, *J. Geophys. Res.*, 97, 15761-15785, 1992.

Clough, S. A., Shephard, M. W., Mlawer, E. J., Delamere, J. S., Iacono, M. J., Cady-Pereira, K., Boukabara, S., and Brown, P. D.: Atmospheric radiative transfer modeling: a summary of the AER codes, Short Communication, *J. Quant. Spectrosc. Radiat. Transfer*, 91, 233-244, 2005.

Connor, T.C., Shephard, M. W., Payne, V. H., Cady-Pereira, K. E., Kulawik, S. S., Luo, M., Osterman, G. and Lampel, M.: Long-term stability of TES satellite radiance measurements, *Atmos. Meas. Tech.*, 4, doi:10.5194/amt-4-1481-2011, 1481–1490, July 25, 2011.

Crevoisier, C., Chédin, A., Matsueda, H., Machida, T., Armante, R., and Scott, N. A.: First year of upper tropospheric integrated content of CO2 from IASI hyperspectral infrared observations, *Atmos. Chem. Phys.*, 9, 4797-4810, https://doi.org/10.5194/acp-9-4797-2009, 2009.

Crevoisier, C., Heilliette, S., Chédin, A., Serrar, S., Armante, R., and Scott, N. A.: Midtropospheric CO2 concentration retrieval from AIRS observations in the tropics, *Geophys. Res. Lett.*, 31, L17106, https://doi.org/10.1029/2004GL020141, 2004.

Crisp, D., Pollock, H. R., Rosenberg, R., Chapsky, L., Lee, R. A. M., Oyafuso, F. A.,

Frankenberg, C., O'Dell, C. W., Bruegge, C. J., Doran, G. B. ; The on-orbit performance of the Orbiting Carbon Observatory-2 (OCO-2) instrument and its radiometrically calibrated products. *Atmos. Meas. Tech.* 10, 59–81, 2017.

de Lange, A. and Landgraf, J.: Methane profiles from GOSAT thermal infrared spectra, *Atmos. Meas. Tech.*, 11, 3815–3828, https://doi.org/10.5194/amt-11-3815-2018, 2018.

Donlon, C. J., Minnett, P. J., Gentemann, C., Nightingale, T. J., Barton, I. J., Ward, B., Murray, M. J.: Toward improved validation of satellite sea surface skin temperature measurements for climate research, *J. Climate*, vol. 15, no. 4, pp. 353–369, 2002.

Donlon, C., Robinson, I.S., Reynolds, M., Wimmer, W., Fisher, G., Edwards, R. and Nightingale, T.J.: An infrared sea surface temperature autonomous radiometer (ISAR) for deployment aboard volunteer observing ships (VOS), *J. Atmos. Ocean. Technol.*, vol. 25, no. 1, pp. 93–113, 2008.

Dudhia, A.: The Reference Forward Model (RFM), *Journal of Quantitative Spectroscopy and Radiative Transfer*, 186, 243–253, doi:10.1016/j.jqsrt.2016.06.018, 2017.

Ehret, G., Bousquet, P., Pierangelo, C., Alpers, M., Millet, B., Abshire, J.B., Bovensmann, H., Burrows, J.P., Chevallier, F., Ciais, P., Crevoisier, C., Fix, A., Flamant, P., Frankenberg, C., Gibert, F., Heim, B., Heimann, M., Houweling, S., Hubberten, H.W., Jöckel, P., Law, K., Löw, A., Marshall, J., Agusti-Panareda, A., Payan, S., Prigent, C., Rairoux, P., Sachs, T., Scholze, M., Wirth, M. : MERLIN: A French-German Space Lidar Mission Dedicated to Atmospheric Methane. *Remote Sens.*, 9, 1052 ,2017.

Eldering, A., Taylor, T. E., O'Dell, C. W., and Pavlick, R. : The OCO-3 mission: measurement objectives and expected performance based on 1 year of simulated data, *Atmos. Meas. Tech.*, 12, 2341–2370, https://doi.org/10.5194/amt-12-2341-2019, 2019.

Eriksson, P., Buehler, S. A., Davis, C.P., Emde, C., Lemke, O.: ARTS, the atmospheric radiative transfer simulator, Version 2, *Journal of Quantitative Spectroscopy and Radiative Transfer.* 112 (10): 1551–1558. Bibcode:2011JQSRT.112.1551E. doi:10.1016/j.jqsrt.2011.03.001. Retrieved 2016-11-02, 2011.

Fiedler, L., Newman, S., and Bakan, S.: Correction of detector nonlinearity in Fourier

transform spectroscopy with a low-temperature blackbody, *Appl. Opt.*, 44, 5332-5340, 2005.
GHGSat-C1/C2, URL: http://www.ghgsat.com/who-we-are/our-satellites/satellite-2/ (accessed on 12 October 2019).

GSICS Traceability Statement for IASI and AIRS v1A, document EUM/MET/TEN/11/0157, Oct. 2014. [Online]. Available: https://www.eumetsat.int/website/wcm/idc/idcplg?IdcService=GET_FILE&dDocName=PDF_TRACE_STAT_IASI_AIRS&RevisionSelectionMethod=LatestReleased&Rendition=Web

Gordon, I.E., Rothman, L.S., Hill C., et al.: The HITRAN2016 Molecular Spectroscopic Database, *J. Quant. Spectrosc. Radiat. Transf.*, 203, 3-69, 2017.
Hamamatsu Photonics K.K.: Characteristics and use of infrared detectors, Technical Information SD-12, 2011.

Holben, B. N., Eck, T. F., Slutsker, I., Tanré, D., Buis, J. P., Setzer, A., Vermote, E., Reagan, J. A., Kaufman, Y. J., Nakajima, T., Lavenu, F., Jankowiak, I., and Smirnov, A.: AERONET— A federated instrument network and data archive for aerosol characterization, *Remote Sens. Environ.*, vol. 66, no. 1, pp. 1–16, 1998.

Hook, S. J., Clodius, W. B., Balick, L., Alley, R. E., Abtahi, A., Richards, R. C. and Schladow, S. G.: In-flight validation of Mid- and thermal infrared data from the Multispectral Thermal Imager (MTI) using an automated high-altitude validation site at Lake Tahoe CA/NV, USA, *IEEE Trans. Geosci. Remote Sens.*, vol. 43, no. 7, pp. 1991–1999, 2005.

Hook, S. J., Vaughan, R. G., Tonooka, H. and Schladow, S. G.: Absolute radiometric in-flight validation of mid infrared and thermal infrared data from ASTER and MODIS on the Terra spacecraft using the Lake Tahoe, CA/NV, USA, automated validation site, *IEEE Trans. Geosci. Remote Sens.*, vol. 45, no. 6, pp. 1798–1807, 2007.

Hu, H., Landgraf, J., Detmers, R., Borsdorff, T., Aan de Brugh, J., Aben, I., Butz, A., Hasekamp, O., : Toward Global Mapping of Methane With TROPOMI: First Results and Intersatellite Comparison to GOSAT, *Geophysical Research Letters*, Volume 45, Issue 8, pp. 3682-3689, 2018.

Hébert, Ph., Blumstein, D., Buil, C., Carlier, T., Chalon, G., Astruc, P., Clauss, A., Siméoni,

D. and Tournier B.: IASI instrument: technical description and measured performances", In: Proceedings of the 5th International Conference on Space Optics (ICSO 2004), 30 March - 2 April 2004, Toulouse, France. Ed.: B. Warmbein. ESA SP-554, Noordwijk, Netherlands: ESA Publications Division, ISBN 92-9092-865-4, p. 49 – 56, 2004.

Illingworth, S. M., Remedios, J. J., and Parker, R. J.: Intercomparison of integrated IASI and AATSR calibrated radiances at 11 and 12 μm, *Atmos. Chem. Phys.*, 9, 6677-6683, https://doi.org/10.5194/acp-9-6677-2009, 2009.

Inoue, T.: On the temperature and effective emissivity determination of semi-transparent cirrus clouds by bi-spectral measurements in the 10 μm window region, *J. Meteorol. Soc. Jpn.*, vol. 63, no. 1, pp. 88–98, 1985.

Institute for Environmental Studies (NIES) GOSAT Data Archive Service (GDAS). Accessed: Oct. 24, 2019. [Online]. Available: https://data2.gosat.nies.go.jp/

Iwata, T. and Koshoubu, J.: Correction of Nonlinearity of Photoconductive MCT Detector in Fourier-Transform Infrared Spectroscopy, *Journal of the Spectroscopical*, Vol 46, Issue 3, 1997.

Jacquinet-Husson, N. , Armante, R., Scott, N.A., Chedin, A., Crépeau, L., Boutammine, C., Bouhdaoui, A., Crevoisier, C., Capelle, V., Boonne, C., Poulet-Crovisier, N., Barbe, A., Chris Benner, D., Boudon, V., Brown, L. R., Buldyreva, J. , Campargue, A., Coudert, L. H. , Devi, V. M., Down, M.J., Drouin, B. J. et al : The 2015 edition of the GEISA spectroscopic database, *J. Mol. Spectrosc.*, 327, 31-72, http://dx.doi.org/10.1016/j.jms.2016.06.007, 2016.

Jacquinet-Husson, N. et al. : The 1997 spectroscopic GEISA data bank, *J. Quant. Spectrosc. Radiat. Transf.*, 62, 205-254, 1999.

Jacquinet-Husson, N. et al.,: The GEISA spectroscopic database: Current and future archive for Earth and planetary atmosphere studies, *J. Quant. Spectrosc. Radiat. Transf.*, 109, 1043-1059, 2008.

JAXA/EORC GOSAT Website: https://www.eorc.jaxa.jp/GOSAT/index.html (accessed on 22 January 2020).

Keens, A., and Simon, A.: Correction of non-linearities in detectors in Fourier Transform Spectroscopy', United States Patent number 4927269, May 22, 1990.

Kikuchi, N., Kuze, A., Kataoka, F., Shiomi, K., Hashimoto, M., Suto, H., Knuteson, R. O., Iraci, L. T., Yates, E. L., Gore, W., Tanaka, T.: Three-dimensional distribution of greenhouse gas concentrations over megacities observed by GOSAT, in Proc. AGU Fall Meeting Abstr., Paper #A32D-02, 2017.

Kilpatrick, K. A., Podestá, G. P., and Evans, R.: Overview of the NOAA/NASA advanced very high resolution radiometer Pathfinder algorithm for sea surface temperature and associated matchup database, *J. Geophys. Res.*, Oceans, vol. 106, no. C5, pp. 9179–9197, 2001.

Knuteson, R. O., Revercomb, H. E., Best, F. A., Ciganovich, N. C., Dedecker, R. G., Dirkx, T. P., Ellington, S. C., Feltz, W. F., Garcia, R. K., Howell, H. B., Smith, W. L., Short, J. F., Tobin, D. C.: Atmospheric emitted radiance interferometer. Part I: Instrument design, *J. Atmos. Ocean. Technol.*, vol. 21, no. 12, pp. 1763–1776, 2004a.

Knuteson, R. O., Revercomb, H. E., Best, F. A., Ciganovich, N. C., Dedecker, R. G., Dirkx, T. P., Ellington, S. C., Feltz, W. F., Garcia, R. K., Howell, H. B., Smith, W. L., Short, J. F., Tobin, D. C.: Atmospheric emitted radiance interferometer. Part II: Instrument performance, *J. Atmos. Ocean. Technol.*, vol. 21, no. 12, pp. 1777–1789, 2004b.

Knuteson, R. O., Best, F. A., Deslover, D. H., Osborne, B. J., Revercomb, H. E., Smith, W. L.: Infrared land surface remote sensing using high spectral resolution aircraft observations, *Adv. Space Res.*, vol. 33, no. 7, pp. 1114–1119, 2004c.

Kulawik, S. S., Worden, J. R., Wofsy, S. C., Biraud, S. C., Nassar, R., Jones, D. B. A., Olsen, E. T., Jimenez, R., Park, S., Santoni, G. W., Daube, B. C., Pittman, J. V., Stephens, B. B., Kort, E. A., Osterman, G. B., and TES team: Comparison of improved Aura Tropospheric Emission Spectrometer CO2 with HIPPO and SGP aircraft profile measurements, *Atmos. Chem. Phys.*, 13, 3205-3225, https://doi.org/10.5194/acp-13-3205-2013, 2013.

Kuze, A., O'Brien, D. M., Taylor, T. E., Day, J. O., O'Dell, C., Kataoka, F., Yoshida, M., Mitomi, Y., Bruegge, C., Pollock, H., Basilio, R., Helmlinger, M., Matsunaga, T., Kawakami, S., Shiomi, K., Urabe, T., and Suto, H.: Vicarious calibration of the GOSAT sensors using the Railroad Valley desert playa," *IEEE Trans. Geosci. Remote Sens.*, vol. 49, no. 25, pp. 1781–1795, 2011.

Kuze, A., Suto, H., Nakajima, M., and Hamazaki, T.: Thermal and near infrared sensor for carbon observation Fourier-transform spectrometer on the Greenhouse Gases Observing Satellite for greenhouse gases monitoring, *Appl. Opt.*, 48, 6716–6733, 2009.

Kuze, A., Suto, H., Shiomi, K., Kawakami, S., Tanaka, M., Ueda, Y., Deguchi, A., Yoshida, J., Yamamoto, Y., Kataoka, F., Taylor, T. E., and Buijs, H. L.: Update on GOSAT TANSO-FTS performance, operations, and data products after more than 6 years in space, *Atmos. Meas. Tech.*, 9, 2445–2461, https://doi.org/10.5194/amt-9-2445-2016, 2016.

Kuze, A., Suto, H., Shiomi, K., Urabe, T., Nakajima, M., Yoshida, J., Kawashima, T., Yamamoto, Y., Kataoka, F., and Buijs, H. L.: Level 1 algorithms for TANSO on GOSAT: Processing and on-orbit calibrations, *Atmos. Meas. Tech.*, vol. 5, no. 10, pp. 2447–2467, 2012.

Lachance, R. L., Villemciire, A., Rochette, L.: Correction of the non-linearity of FT remote sensing instruments, Third Workshop on Infrared Emission Measurements by FTIR, Quebec, Feb. 4 – 6 ,1998.

Lamsal, L. N., Weber, M., Tellmann, S. and Burrows, J. P.: Ozone column classified climatology of ozone and temperature profiles based on ozonesonde and satellite data, *J. Geophys. Res.*, vol. 109, no. D20, pp. D20 304 -1–D20 304-15, 2004.

Ligori, M., Bradbury, L., Spina, R., Zee, R. E. : GHGSat Constellation: The Future of Monitoring Greenhouse Gas Emissions, in Proc. 33rd Annual AIAA/USU Conference on Small Satellites,2019.

Maddy, E. S., Barnet, C. D., Goldberg, M., Sweeney, C., and Liu, X.: CO2 retrievals from the Atmospheric Infrared Sounder: Methodology and validation, *J. Geophys. Res., Atmos.*, vol. 113, p. D11301, 2008.

Matricardi, M.: Technical Note: An assessment of the accuracy of the RTTOV fast radiative transfer model using IASI data, *Atmos. Chem. Phys.*, 9, 6899-6913, https://doi.org/10.5194/acp-9-6899-2009, 2009.

Matsunaga, T., Morino, I., Yoshida, Y., Saito, M., Noda, H., Ohyama, H., Kamei, A.,

Kawazoe, F., Maksyutov, S., Yokota, T., Kuze, A., Suto, H., Nakajima, M., and Imasu, R., : FTS and FTS-2 Onboard Japanese GOSAT Earth Observation Satellite Series, in Light, Energy and the Environment 2018 (E2, FTS, HISE, SOLAR, SSL), OSA Technical Digest Optical Society of America, 2018.

Moore, B., Crowell, S. M. R., Rayner, P. J., Kumer, J., O'Dell, C. W., O'Brien, D., Utembe, S., Polonsky, I., Schimel,D., Lemen, J. : The Potential of the Geostationary Car- bon Cycle Observatory (GeoCarb) to Provide Multi-scale Constraints on the Carbon Cycle in the Americas. *Front. Env. Sci.*, 6, 109, doi:10.3389/fenvs.2018.00109, 2018.

Nakajima, M., Suto, H., Yotsumoto, K., Shiomi, K., Hirabayashi, T. : Fourier transform spectrometer on GOSAT and GOSAT-2, Proc. SPIE 10563, International Conference on Space Optics — ICSO 2014, 105634O (17 November 2017), https://doi.org/10.1117/12.2304062

Nakamura, T.: Overview of IBUKI-equipped monitor camera and results on orbit (in Japanese), Aeronautical and Space Sciences Japan, Volume 58 Issue 675 111-115, https://doi.org/10.14822/kjsass.58.675_111, 2010.

Na-Nakornpanom, A., Lee, A.M. A, Chapsky, L.: In-Flight Thermal Performance of the OCO-2 Instrument, Proc. 47th International Conference on Environmental Systems, 2017.

Nicol, P., Fleury, J., and Bernard, F.: The IASI detection chain, Proceedings of the 5th International Conference on Space Optics (ICSO 2004), 30 March - 2 April 2004, Toulouse, France. Ed.: B. Warmbein. ESA SP-554, Noordwijk, Netherlands: ESA Publications Division, ISBN 92-9092-865-4, p. 751 – 758, 2004.

Olsen, K. S., Strong, K., Walker, K. A., Boone, C. D., Raspollini, P., Plieninger, J., Bader, W., Conway, S., Grutter, M., Hannigan, J. W., Hase, F., Jones, N., de Mazière, M., Notholt, J., Schneider, M., Smale, D., Sussmann, R., and Saitoh, N.: Comparison of the GOSAT TANSO-FTS TIR CH4 volume mixing ratio vertical profiles with those measured by ACE-FTS, ESA MIPAS, IMK-IAA MIPAS, and 16 NDACC stations, *Atmos. Meas. Tech.*, 10, 3697–3718, https://doi.org/10.5194/amt-10-3697-2017, 2017.

Ota, Y. and Imasu, R.: CO2 retrieval using thermal infrared radiation observation by Interferometric Monitor for Greenhouse Gases (IMG) onboard Advanced Earth Observing

Satellite (ADEOS), *J. Meteorol. Soc. Jpn.*, 94, 471–490, 2016.

Pachauri, R. K. et al.: Climate Change 2014: Synthesis Report. Contribution of Working Groups I, II and III to the Fifth Assessment Report of the Intergovernmental Panel on Climate Change / R. Pachauri and L. Meyer (editors), Geneva, Switzerland, IPCC, 151 p., ISBN: 978-92-9169-143-2, 2014.

Pagano, T., Aumann, H., Overoye, K.: Level 1B products from the Atmospheric Infrared Sounder (AIRS) on the EOS Aqua Spacecraft, International TOVS Study Conference-XIII Proceedings, 2003a.

Pagano, T., Chahine, M., Aumann, H., Elliott, D., Manning, E., Realmuto, V., Thompson, C., Lambrigtsen, B., Lee, S., Broberg, S., Olsen, E., Fetzer, E., Strow, L.: AIRS/AMSU/HSB on EOS Aqua First Year Post Launch Assessment, SPIE Proc., 5151-25, Aug. 2003b.

Payan, S., Camy-Peyret, C., and Bureau, J. ; Comparison of retrieved L2 products from four successive versions of L1B spectra in the thermal infrared band of TANSO-FTS over the arctic ocean, *Remote Sens.*, vol. 9, p. 1167, Nov. 2017.

Pitman, K. M., Wolff, M. J. and Clayton, G. C.: Application of modern radiative transfer tools to model laboratory quartz emissivity, *J. Geophys. Res.*, vol. 110, no. E8, p. E08 003, 2005.

Revercomb, H. E., Buijs, H., Howell, H. B., LaPorte, D. D., Smith, W. L. and Sromovsky, L. A.: Radiometric calibration of IR Fourier transform spectrometers: solution to a problem with the High-Resolution Interferometer Sounder, *Appl. Opt.*, 27, 3210-3218 , 1988.

Rinsland, C. P., Luo, M., Logan, J. A., Beer, R., Worden, H., Kulawik, S., Rider, D., Osterman, G., Gunson, M., Eldering, A., Goldman, A., Shephard, M., Clough, S. A., Rodgers, C., Lampel, M., Chiou, L.: Nadir measurements of carbon monoxide distributions by the Tropospheric Emission Spectrometer instrument onboard the Aura Spacecraft: Overview of analysis approach and examples of initial results, *Geophys. Res. Lett.*, 33, L22806, doi:10.1029/2006GL027000, 2006.

Rodriguez I. J., Ronald G. Ross G. R.: AIRS on-orbit cryocooler system performance, Proc. SPIE 5151, Earth Observing Systems VIII, 2003.

Rodriguez I. J., Na-Nakornpanom, A.: On-Orbit performance of the TES pulse tube cryocooler system and the instrument - Six years in space, AIP Conference Proceedings 1434, 137,2012.

Rogalski, A.: Recent progress in infrared detector technologies, Infrared Physics & Technology, Volume 54, Issue 3, p. 136-154, 2011.

Ross, R.G., Jr., Johnson, D.L., Elliott, D.: AIRS Pulse Tube Coolers Performance Update – Twelve Years in Space," Cryocoolers 18, ICC Press, Boulder, CO, pp. 87-95, 2014.

Rothman, L., Gordon, I., Barber, R., Dothe, H., Gamache, R., Goldman, A., Perevalov, V., Tashkun, S., Tennyson, J.: HITEMP, the high-temperature molecular spectroscopic database, *J. Quant. Spectrosc. Radiat. Transf.*,111, 2139–2150, 2010.

Saitoh, N., Imasu, R., Ota, Y., and Niwa, Y.: CO2 retrieval algorithm for the thermal infrared spectra of the Greenhouse Gases Observing Satellite: Potential of retrieving CO2 vertical profile from high-resolution FTS sensor, *J. Geophys. Res.*, Atmos., vol. 114, p. D17305, 2009.

Saitoh, N., Kimoto, S., Sugimura, R., Imasu, R., Kawakami, S., Shiomi, K., Kuze, A., Machida, T., Sawa, Y., and Matsueda, H.: Algorithm update of the GOSAT/TANSO-FTS thermal infrared CO2 product (version 1) and validation of the UTLS CO2 data using CONTRAIL measurements, *Atmos. Meas. Tech.*, 9, 2119–2134, https://doi.org/10.5194/amt-9-2119-2016, 2016.

Saitoh, N., Kimoto, S., Sugimura, R., Imasu, R., Shiomi, K., Kuze, A., Niwa, Y., Machida, T., Sawa, Y., and Matsueda, H.: Bias assessment of lower and middle tropospheric CO2 concentrations of GOSAT/TANSO-FTS TIR version 1 product, *Atmos. Meas. Tech.*, 10, 3877–3892, https://doi.org/10.5194/amt-10-3877-2017, 2017.

Saunders, R., Hocking, J., Turner, E., Rayer, P., Rundle, D., Brunel, P., Vidot, J., Roquet, P., Matricardi, M., Geer, A., Bormann, N., and Lupu, C.: An update on the RTTOV fast radiative transfer model (currently at version 12), *Geosci. Model Dev.*, 11, 2717-2737, https://doi.org/10.5194/gmd-11-2717-2018., 2018.

Scott N.A. and Chédin A.: A fast line-by-line method for atmospheric absorption

computations: The Automatized Atmospheric Absorption Atlas, *J. Appl. Meteor.*, 20, n° 7, pp. 802-812 ,1981.

Shephard, M.W., Worden, H. M., Cady-Pereira, K. E., Lampel, M., Luo, M., Bowman, K. W., Sarkissian, E., Beer, R., Rider, D. M., Tobin, D. C., Revercomb, H. E., Fisher, B. M., Tremblay, D., Clough, S. A., Osterman, G. B., and Gunson, M.: Tropospheric emission spectrometer Nadir spectral radiance comparisons, *J. Geophys. Res.*, vol. 113, no. D15, pp. D15 S05-1–D15 S05-12, 2008.

Stiller, G.P. (Editor) with contributions from Clarmann, T. V., Dudhia, A., Echle, G.,   Funke, B. , Glatthor, N., Hase, F., Höpfner, M., Kellmann, S., Kemnitzer, H., Kuntz, M., Linden, A., Linder, M., Zorn, S.: The Karlsruhe Optimized and Precise Radiative transfer Algorithm (KOPRA), Forschungszentrum Karlsruhe, Wissenschaftliche Berichte, Bericht Nr. 6487, 2000.

Strow, L. L., Hannon, S. E., Weiler, M., Overoye, K., Gaiser, S. L. and Aumann, H. H.: Prelaunch spectral calibration of the atmospheric infrared sounder (AIRS), *IEEE Trans. Geosci. Remote Sens.*, vol. 41, no. 2, pp. 274-286, doi: 10.1109/TGRS.2002.808245, 2003.

The introduction of Automatized Atmospheric Absorption Atlas (4A). Available online: : http://ara.abct.lmd.polytechnique.fr/index.php?page=4a#3 (accessed on 10 October 2019).

Tobin, D., Revercomb, H., Knuteson, R., Taylor, J., Best, F., Borg, L., DeSlover, D., Martin, G., Buijs, H., Esplin, M., Glumb, R., Han, Y., Mooney, D., Predina, J., Strow, L., Suwinski, L., Wang, L.: Suomi-NPP CrIS radiometric calibration uncertainty, *J. Geophys. Res., Atmos.*, vol. 118, no. 18, pp. 10,589–10,600, 2013.

Tobin, D.C., Revercomb, H.E., Knuteson, R.O., Best, F.A., Smith, W.L., Ciganovich, N.N., Dedecker, R.G., Dutcher, S., Ellington, S.D., Garcia, R.K., Howell, H.B., Laporte, D.D., Mango, S.A., Pagano, T.S., Taylor, J.K., Delst, P.V., Vinson, K.H., and Werner, M.W.: Radiometric and spectral validation of atmospheric infrared sounder observations with the aircraft-based scanning high-resolution interferometer sounder, *J. Geophys. Res.*, vol. 111, no. D9, pp. D09 S02-1–D09 S02-14, 2006.

Tribble, A. C., Boyadjian, B., Davis, J., Haffner, J., McCullough, E.: Contamination control engineering design guidelines for the aerospace community, NASA-CR-4740, NAS 1.26:4740,

M-810, NAS5-32876, 96N32082, 1996.

Vomel, H., Selkirk, H, Miloshevich, L., Valverde-Canossa, J., Vald_es, J., Kyr_o, E., Kivi, R., Stolz, W., Peng, G. and Diaz, J. A.: Radiation dry bias of the Vaisala RS92 humidity sensor, *J. Atmos. Ocean. Technol.*, vol. 24, no. 6, pp. 953–963, 2007.

Wan Z. and Li, Z.-L.: A physics-based algorithm for retrieving land surface emissivity and temperature from EOS/MODIS data, *IEEE Trans. Geosci. Remote Sens.*, vol. 35, no. 4, pp. 980–996, 1997.

Wang, L., Wu, X., Goldberg, M., Cao, C., Li, Y. and Sohn, S.: Comparison of AIRS and IASI Radiances Using GOES Imagers as Transfer Radiometers toward Climate Data Records. *J. Appl. Meteor. Climatol.*, 49, 478–492, https://doi.org/10.1175/2009JAMC2218.1, 2010.

Wilson, S. H. S., Atkinson, N. C. and Smith, J. A.: The development of an airborne infrared interferometer for metorological sounding studies, *J. Atmos. Oceanic Technol.*,16, 1912–1926, 1999.

Worden H. M. and Bowman, K. W.: Tropospheric Emission Spectrometer (TES) Level 1B Algorithm Theoretical Basis Document, Rep. JPL D-16479 @Jet Propulsion Laboratory, California Institute of Technology, 1999.

Worden H., Beer,R., Bowman, K. W., Fisher, B., Luo, M., Rider, D., Sarkissian, E., Tremblay, D.: TES level 1 algorithms: interferogram processing, geolocation, radiometric, and spectral calibration, *IEEE Trans. Geosci. Remote Sens.*, vol. 44, no. 5, pp. 1288-1296, 2006.

World Meteorological Organization (WMO): WMO Greenhouse Gases Bulletin: The State of Greenhouse Gases in the Atmosphere Using Global Observations up to December 2015, No. 12, https://gaw.kishou.go.jp/static/publications/bulletin/Bulletin2015/ghg-bulletin-12.pdf, 2016.

X, F., and Ignatov, A.: In situ SST quality monitor (iQuam), *J. Atmos. Ocean. Technol.*, vol. 31, no. 1, pp. 164–180, 2014.

Yang, Z., Zhen, Y., Yin, Z., Lin, C., Bi, Y., Liu ,W., Wang, Q., Wang, L., Gu, S., Tian, L. :

Prelaunch Radiometric Calibration of the TanSat Atmospheric Carbon Dioxide Grating Spectrometer, *IEEE Trans. Geosci. Remote Sens.*, vol. 56, no. 7, pp. 4225-4233, doi: 10.1109/TGRS.2018.2829224, 2018a.

Yang, D., Liu, Y., Cai, Z., Chen, X., Yao, L., Lu, D : First Global Carbon Dioxide Maps Produced from TanSat Measurements, *Advances in Atmospheric Sciences*, Vol. 35(6),   pp: 621–623, https://doi.org/10.1007/s00376-018-7312-6, 2018b.

Yates, E. L., Lowenstein, M., Iraci, L. T., Tadic, J., Sheffner, E. J., Schiro, K. and Kuze, A.: Carbon dioxide and methane at a desert site - A case study at Railroad Valley playa, Nevada, USA, *Atmosphere*, vol. 2, no. 4, pp. 702–714, 2011.